THESIS FOR THE DEGREE OF DOCTOR OF PHILOSOPHY

# Plasmonic Nanospectrocopy of Individual Nanoparticles

## Studies of Metal-Hydrogen Interactions and Catalysis

SVETLANA ALEKSEEVA


CHALMERS

Department of Physics
CHALMERS UNIVERSITY OF TECHNOLOGY
Gothenburg, Sweden 2017

Plasmonic Nanospectroscopy of Individual Nanoparticles
Studies of Metal-Hydrogen Interactions and Catalysis
SVETLANA ALEKSEEVA
ISBN: 978-91-7597-595-5



Doktorsavhandlingar vid Chalmers tekniska högskola
Ny serie nr 4276
ISSN 0346-718X

Department of Physics
Chalmers University of Technology
SE-412 96 Gothenburg
Sweden
Telephone + 46 (0)31-772 1000

Cover:
An illustration of individual nanoparticles of various shape, size, material and structure lining up one-by-one before the plasmonic antenna particle (in the forefront of the image), for their secrets to be discovered under illumination of light. Cover art created by Marina Gridina and Vitaliy Musatov.

Printed at Chalmers Reproservice
Gothenburg, Sweden 2017

Plasmonic Nanospectroscopy of Individual Nanoparticles
Studies of Metal-Hydrogen Interactions and Catalysis

Svetlana Alekseeva
Department of Physics
Chalmers University of Technology

# Abstract

Localized surface plasmon resonance (LSPR) is the phenomenon of collective oscillation of conduction electrons in metal nanoparticles smaller than the wavelength of light used for the excitation. Plasmonic metal nanoparticles are able to confine light to extremely small volumes around them, i.e. below the diffraction limit. This gives rise to strongly localized and enhanced electromagnetic fields in so-called "hot spots" of the plasmonic nanoparticle. These hot spots are advantageous for sensing, as well as enhancing surface processes, since any object inserted in the hot spot will influence the optical resonance of the system via coupling to the local field. Placing a well-defined nanoobject in the hot spot of a plasmonic nanoantenna offers, thus, unique possibilities to obtain detailed information about the role of specific features (e.g. facets, size, shape or relative abundance of low-coordinated sites) of that particle for its functionality/activity at the single particle level. Consequently, there is an increasing interest to use plasmonic antennas as an *in situ* tool to investigate physical/chemical processes in/on single functional nanomaterials. Single particle measurements are possible with the use of dark-field scattering spectroscopy, since plasmonic nanoparticles efficiently scatter light and are easily observable in the dark-field microscope. In this context, this work was dedicated to: i) Development of fabrication methods for making plasmonic nanoantenna structures with the possibility to place a nanoparticle of interest (e.g. a hydride former or a catalyst) in the hot spot of the antenna, as well as fabrication methods for accommodation of protecting layers for the antenna via complete encapsulation in a core-shell scheme. ii) Investigation of the role of size, shape, defects and microstructure in hydride formation thermodynamics of single-crystalline and polycrystalline palladium (Pd) nanoparticles. iii) Application of the developed fabrication schemes and experimental strategies to the investigation of (photo)catalytic reactions at the single particle level.

**Keywords**: localized surface plasmon resonance, plasmonic sensors, hole-mask colloidal lithography, shrinking-hole colloidal lithography, single particle spectroscopy, dark field scattering spectroscopy, plasmonic nanospectroscopy, nanoscale effects, palladium nanoparticles and nanocrystals, metal-hydrogen interactions, grain boundary, nanocatalysts

# List of appended papers

This thesis is based on the work presented in the following publications:

I. *Shrinking-Hole Colloidal Lithography: Self-Aligned Nanofabrication of Complex Plasmonic Nanoantennas*
Svetlana Syrenova*, Carl Wadell and Christoph Langhammer
Nano Letters **14**, 2655-2663 (2014)

II. *A Versatile Self-Assembly Strategy for the Synthesis of Shape-Selected Colloidal Noble Metal Nanoparticle Heterodimers*
Tina A. Gschneidtner, Yuri A. Diaz Fernandez, Svetlana Syrenova*, Fredrik Westerlund, Christoph Langhammer, and Kasper Moth-Poulsen
Langmuir **30**, 3041-3050 (2014).

III. *Hydride formation thermodynamics and hysteresis in individual Pd nanocrystals with different size and shape*
Svetlana Syrenova*, Carl Wadell, Ferry A. A. Nugroho, Tina A. Gschneidtner, Yuri A. Diaz Fernandez, Giammarco Nalin, Dominika Świtlik, Fredrik Westerlund, Tomasz J. Antosiewicz, Vladimir Zhdanov, Kasper Moth-Poulsen and Christoph Langhammer
Nature Materials **14**, 1236-1244 (2015).

IV. *Grain-Boundary-Mediated Hydriding Phase Transformations in Individual Polycrystalline Metal Nanoparticles*
Svetlana Alekseeva, Alice Bastos da Silva Fanta, Beniamino Iandolo, Tomasz J. Antosiewicz, Ferry A. A. Nugroho, Jakob B. Wagner, Andrew Burrows, Vladimir P. Zhdanov and Christoph Langhammer
*Accepted for publication in Nature Communications.*

V. *Combining Mass Spectrometry with in operando Plasmonic Nanospectroscopy of Single Catalyst Nanoparticles*
Su Liu, Svetlana Alekseeva, Arturo Susarrey-Arce, Lars Hellberg and Christoph Langhammer
*In manuscript*

VI. *A Core-Shell Nanoparticle Library for Optical Absorption Engineering and Plasmon-Mediated Catalysis*
Arturo Susarrey-Arce, Svetlana Alekseeva, Iwan Darmadi, Sara Nilsson, Stephan Bartling, Tomasz J. Antosiewicz and Christoph Langhammer
*In manuscript*

# Related papers not included in this thesis

*Nanoplasmonic Sensing for Nanomaterials Science*

Elin Larsson, Svetlana Syrenova* and Christoph Langhammer

Nanophotonics **1**, 249 (2012).

*Plasmonic Hydrogen Sensing with Nanostructured Metal Hydrides*

Carl Wadell, Svetlana Syrenova* and Christoph Langhammer

ACS Nano 8, 11925-11940 (2014).

* I changed my surname from Syrenova to Alekseeva.

## My contribution to the appended papers

**Paper I:** I fabricated the samples, did the experiments, analyzed the data and wrote the first draft of the paper.

**Paper II:** I did the hydride formation experiments, analyzed the data related to the hydride formation experiments and contributed to the writing of the paper.

**Paper III:** I did all hydride formation experiments, conducted all experimental data analysis and wrote the first draft of the paper.

**Paper IV:** I fabricated all samples, did all hydride formation experiments, conducted all data analysis related to the hydride formation experiments and wrote the first draft of the paper.

**Paper V:** I fabricated the samples and contributed to the writing of the paper.

**Paper VI:** I started the development of the nanofabrication method, supervised a master thesis (I. Darmadi) related to the project, and wrote the first draft of the paper.

# Contents

# 1 INTRODUCTION

Nanoparticles surround us everywhere – just look at your silver spoon: it's releasing nanoparticles as you read this[1]! We become more and more aware of the nanoparticles around us as we are able to look closely enough to see these tiny objects. However, magnifying glasses and optical microscopes[*] are not sufficient for the purpose due to the resolution limit. Instead electron microscopes can be used, since the nanoworld deals with objects that are in the size range of 1 to 100 nm. Nanomaterials behave generally very different compared to bulk (macroscopic) matter with "ordinary" properties. Nanoparticles are common in many different environments and many kinds of physical and chemical processes produce nanoparticles. One can identify two sources of nanoparticles, that is, 1) natural and 2) synthetic (i.e. made by humans, also called anthropogenic)[2]. Natural nanoparticles are contained in, for example, sand, dust and volcanic ash, or in biological matter, for example, viruses, DNA or biomolecules. Synthetic nanoparticles are either incidentally made by-products of daily human activities (e.g. from the exhaust of engines, industrial plants, burning of fossil fuels, mining or simply burning a candle (soot)), or engineered nanoparticles consciously synthesized for a specific purpose. With rapid advances in nanoscience and nanotechnology, it is possible to engineer ever more sophisticated nanostructures that are well defined in terms of size, shape and composition (in comparison to incidental nanoparticles). Nanoparticles can also be made by relatively simple chemical processes that have been in the arsenal of alchemists and chemists for centuries. Ancient Romans[3] and Egyptians[4] are considered to be among the first to exploit nanoparticles for their needs such as hair dyeing, colouring glass and making jewelry. One can only guess that they did not know what *exactly* they were doing. Nevertheless, the results of their work are remarkable and there are things we can learn from ancient nanotechnology. For example, reproduction and analysis of hair dyeing recipes dating back 2000 years have shown that it is the precipitation of galena (lead sulfide) nanocrystals within the hair during chemical treatment that produces a very effective black dye. In the process, lead comes from an applied dyeing paste and sulfur that participates in the reaction – from aminoacids in keratin (protein in hair). This observation has stimulated further investigations of crystal growth mechanisms and ion diffusion in hair for potential applications of the hair fibers to be used as nanoreactors in development of nanocomposites[5,6]. Another well-known example of

[*] Technically, with an optical microscope (as will be shown in this thesis) it is possible to see the *scattering* or *fluorescence* from the nanoparticles. However the resolution of the optical microscope is still not good enough to see structural details of the nanoparticles.

nanocraftsmanship is the use of colloidal solutions of metals such as gold, silver and copper. In nanoparticle solution form, the precious metals that we are accustomed to see having metallic shine, in fact, give rise to vibrant colors like red, pink, purple, yellow, green, etc., depending on the size and shape of the colloidal nanoparticles. The colloidal solution could be impregnated into glass[3], which have been used for making decorative cups, stained windows in churches and mosques and also glaze decorations on medieval ceramics[7].

Nowadays, nanoparticles are on the way to large-scale commercialization with ongoing research in implementing the nanoparticles in new products with better or completely new properties. Already commercialized applications can be found in many products ranging from health care items and cosmetics (e.g. sun screens, toothpaste and drugs), food and agricultural products, sports equipment and toys, to electronics and construction materials. Several databases are available on the Internet listing more than 1000 consumer products where nanomaterials are used deliberately in their production[8].

Nanoparticles are intensively studied for many key applications in our present and future society. In medicine, researchers are developing nanoparticles to help cure[9,10] or prevent[11] diseases. Nanoparticles could be employed for efficient drug delivery, diagnostics of diseases, therapeutic and anti-microbial treatments. The idea to use nanomaterials in diagnosis, treatment and protection can be extended also to the conservation of cultural artifacts. Nanomaterials are applied, for example, in cleaning paintings from old coatings, strengthening the paint and neutralizing acidity that degrades paper and wood artifacts[12]. Coatings against pollution and microbial contamination of the architectural surfaces[13] (i.e. buildings) could be used for the preservation of cultural heritage such as historical buildings and monuments. Furthermore, there are ongoing studies to use nanoparticles for food safety and storage applications[14], where nanoparticles can be used in packaging with high barrier properties against gases, small organic molecules and bacteria, and also as sensors for detection of food contaminants and microbes.

The field of electronics is traditionally linked to nanoscience and nanotechnology, which is related to not only the miniaturization of the electronic devices, but also building completely new ones (moving away from silicon electronics towards, for example, molecular devices[15]) that are lightweight and consume less power.

Nanoparticles are furthermore essential to save the Earth from pollution. This includes development of strategies for water purification[16,17] by removing industrial waste pollutants, salts, metals and bacteria from water. Better air quality[18] is another important aspect, where nanoparticles are used in catalysts that reduce harmful emissions from vehicles and industrial plants, and for adsorption of toxic gases like nitrogen oxides ($NO_x$), carbon dioxide ($CO_2$), dioxins and volatile organic compounds from air. Reactive nanomaterials are investigated for the use in cleaning of large-scale contaminated sites[19], where they could transform and detoxify pollutants reducing costs and time for cleanup. Finally, nanoparticles will play a crucial role in the

development of efficient and sustainable energy sources[20], such as solar cells, fuel cells, batteries, hydrogen production and hydrogen storage.

As becomes clear from the above, we have seemingly infinite motivations to tame nanomaterials for the benefit of mankind. Moreover, as never before in human history, we are exposed to rapidly increasing amounts of nanoparticles. On one hand, we have many incidental nanoparticles contained in, for example, by-products of fossil fuel burning and air pollution from industrial plants. On the other hand, with advances of nanotechnology, also the amount of exposure to engineered nanoparticles is increasing. It is therefore imperative that we have sufficient understanding of nanoparticle properties, both natural and synthetic, as well as the many possible reactions and interactions that they may undergo. This is important not only for their best performance for a specific task, but also for the health of humans and our planet, if/when nanoparticles are emitted into the environment.

This thesis is about the design and understanding of engineered nanoparticles with well-defined sizes, shapes and composition. It is clear that there is an immense variety of questions one can ask and study about nanoparticles, and, thus, it is hard to embrace them all. Therefore, this work is mainly focused on studying the interaction of a nanoparticle with its surrounding environment. Among these interactions the focus is placed on events such as ad-/absorption or desorption of species on/from the particle. These processes were studied here in the context of the two fields, namely metal-hydrogen systems and catalysis. The following paragraphs introduce the importance of metal-hydrogen interactions and the concept of catalysis, techniques for how to study hydrogen-absorbing and catalyst nanoparticles and challenges in this direction.

## 1.1 Hydrogen-metal interactions

The interest in metal-hydrogen systems is stimulated both from a fundamental and an applications point of view, which naturally overlap with each other. Many interesting properties that can immediately or potentially be used are related to the small size of the hydrogen atoms, which allows them to occupy interstitial sites in metal lattices, and with high mobility diffuse within the host. As a result of the high mobility, it is possible for hydrogen atoms to relatively quickly reach thermodynamic equilibrium inside a metal even at room temperature. This is the reason why metal-hydrogen systems are often used as model systems for studying physical/chemical properties and their change with concentration, for example, solute-solute interactions[21], quantum mechanical tunnelling as a diffusion mechanism for atoms in solids[22], hydrogen density modulations related to sample geometry[23], behaviour of systems with reduced dimensions and modulated hydrogen affinity[24], as well as influence of defects[25].

Applications of metal-hydrogen systems extend to several areas of which some will be discussed here. One of these areas of interest is hydrogen storage, which is an important pillar of the proposed *hydrogen economy*, where hydrogen is envisioned as an alternative to traditional fuels (i.e. coal, oil and natural gas). This is motivated by the abundance of hydrogen on Earth (however, not in molecular form but covalently

bonded in hydrocarbons) and since it can either be combusted or drive an electrochemical process in a fuel cell, producing in both cases only heat and water as (by-)products. The outstanding energy density of hydrogen comes from its low molecular weight and high molar heat of combustion, which makes it excellent from the perspective of energy density by weight. However, the difficulty is that hydrogen has very low energy density by volume (compared to hydrocarbon fuels), unless it is highly compressed or liquefied. Both of these forms of storage are problematic in terms of safety and cost. Liquid hydrogen has a low boiling point (around 20 K), which requires expensive cryogenic storage that requires good thermal insulation. In this respect, metal hydrides have long been considered as possible alternative for effective and safe lightweight hydrogen storage systems in vehicles. This builds on the fact that many metals and metal alloys under appropriate temperature and pressure conditions react with hydrogen to reversibly form metal hydrides. Therefore, they are considered as a potential solution to the problem offering reduced energy costs, low reactivity (important for safety) and high hydrogen storage densities.[26] However, in today's commercially available hydrogen fuel cell powered cars, such as the Toyota Mirai, it is high pressure tanks made from high-strength and light-weight carbon-fiber based composite materials for compressed hydrogen gas which are the storage systems of choice.

Another interesting aspect of the unique property of metals and metal alloys to absorb hydrogen under constant pressure is that the absorption process is accompanied by the release of heat. This means that, if the hydride formation reaction is reversible, thermal energy can be reversibly stored in hydrides. Therefore metal hydrides can be used not only for hydrogen storage but also for storage of heat. A fundamental difference between the two forms of storage is that in the latter case the heat of reaction from hydride formation can be used as heat while retaining the hydrogen in a closed system through many heat storage cycles, whereas in the former case the hydrogen is liberated from the hydride in an open system and irreversibly reacting to form water[27]. Heat storage materials may be critical to the energy storage process of both solar and nuclear power plants. For example, a metal hydride system for storing solar energy can work by heating a high temperature metal hydride during the day by the sun. This releases hydrogen, which is stored either in a volumetric gas tank, or by another metal hydride that operates at lower temperature. The heat from the high temperature hydride is then extracted for generation of electricity through a heat engine or steam turbine during the night. [28]

One more relevant aspect of metal-hydrogen systems related to the hydrogen economy is hydrogen sensing. In a hydrogen sensor it is the sensing element that enables the detection of hydrogen and its concentration. To this end, due to their high affinity to hydrogen, as well as their high selectivity, metal hydrides are ideal as active materials in a hydrogen sensor. More specifically, this is due to the fact that, upon interaction with hydrogen, a hydride-forming metal may change its temperature, refractive index, mass, electrical, mechanical or optical properties, which are all parameters that can be measured with high accuracy and, thus, serve as the basis for hydrogen detection. Hence, metal hydrides are very attractive transducers in various types of hydrogen

sensors. If hydrogen is to be introduced as an energy carrier on a large scale, hydrogen sensors will be an important part of the infrastructure to ensure safe handling by detecting hydrogen leaks and preventing ignition/explosion of highly flammable/explosive hydrogen-air mixtures. Besides the hydrogen economy, hydrogen sensors are significant for safe operation in the chemical industry, where hydrogen is either a necessary component or by-/end product of chemical processes (e.g. production of ammonia and methanol and refinement of crude oils).[29]

So far, I have highlighted the possible beneficial aspects of the interaction of hydrogen with metals. However, there is also a backside of the coin. Since hydrogen, due to its abundance, is often present in metals already from the first stages of production and processing, it is known to be the cause of a large number of degradation and material failure processes, such as hardening, embrittlement and internal damage. Metal failure is of high technological importance, and the negative role of hydrogen in this respect has been studied for many decades in terms of the underlying mechanisms and preventive measures of hydrogen related degradation.[30] The small size and high mobility of hydrogen atoms are at the core of the problem. In general, hydrogen damage can be caused by interaction of hydrogen with defects in the crystal lattice of the metal, with alloying or impurity elements, and by precipitation at internal surfaces such as voids or pores.[31]

Finally, the interest in *nanoscale* metal-hydrogen systems is caused mainly by the large surface-to-volume ratio of nanoparticles and shorter hydrogen diffusion paths. Both these aspects, solely related to geometry and size, are expected to improve hydrogen absorption/desorption kinetics because hydrogen uptake happens only through the surface, and diffusion barriers inside the host typically are rate limiting during hydride formation/decomposition. This is especially interesting for storage applications and hydrogen sensors, where fast response to hydrogen is desirable. For example, in hydrogen-powered vehicles it translates into sufficiently fast refuelling rates and adequate performance of the tank system during operation. However, significant research efforts are still needed to provide deeper understanding of the physical mechanisms of the enhancement effects observed in nanosized metal hydrides. Many of the effects go beyond simple geometrical and size/diffusion length aspects, such as the influence of defects or impact of mechanical stress[25], as discussed in more detail in Chapter 3.

## 1.2 Catalysis

Nanoparticles are the workhorses of heterogeneous catalysis. However, before we come to that, let us ask ourselves, what is a catalyst? Making an analogy to the world of movies, if there was a (re)action movie to be made, starring chemical A and chemical B that together form product P, a catalyst could play a guy that comes in with a line: “We can do this the hard way or the easy way”. In other words, a catalyst is a substance that facilitates a chemical reaction by lowering the activation energy that is needed for the reaction to occur. In a catalysed process, reactants A and B adsorb to

the catalyst, maybe dissociate, and react with each other while they are transiently bound to it. The activation energy of the rate limiting elemental reaction step along this reaction pathway is significantly lower than that in the corresponding uncatalysed reaction. In this way, a catalyst is able to significantly enhance the rate of reaction or change the distribution of the reaction products selectively towards specific compounds. When the product is formed, it detaches from the catalyst and leaves it unaltered and unconsumed during the process, so that the catalyst is available for the next reaction event. While the overall change in free energy is the same both for catalysed and uncatalysed reactions, the kinetic barriers are lowered.

There are three types of catalysts: biocatalysts (enzymes and cells), homogeneous catalysts and heterogeneous catalysts. In heterogeneous catalysis, as opposed to the homogeneous, the catalyst and reactants are in different states, i.e. solid, liquid or gas. Usually, the catalyst material is a solid, and reactants are molecules in the gas or liquid phase. Heterogeneous catalysts can be metals, oxides, sulfides, carbides, nitrides – in other words, practically any type of material. Supported *nanoparticle* catalysts made from such materials are especially interesting (and constitute the majority of industrial catalysts) since they provide a large surface area per unit mass, and therefore such nanocatalysts are more effective. In addition, the smaller the used nanoparticles are the larger the abundance of low-coordinated sites such as edges/steps and corners, which in some cases are characterized with high reactivity. To enable the operation of nanoparticle catalysts and minimize sintering effects, the nanoparticles are typically dispersed on a support material. This support can be either amorphous (e.g. porous alumina, silica, carbon (C)) or crystalline (zeolites), and mainly serves as a template with high surface area and porosity that allows maximizing the total number of active sites per unit volume of the catalyst system.

### 1.2.1 Why study catalysts?

Catalysts are very important in the chemical industry for production of chemicals and energy, and they are also key in pollution mitigation. In fact, the vast majority of existing chemical products and fuels involve catalytic processes at some point during their production. Furthermore catalysts are often needed in hydrogen storage materials[32] to enable hydrogen molecule dissociation on/in the material as the first critical step for hydrogen absorption/hydride formation, or to improve kinetics of hydrogen absorption/desorption processes. Therefore, the need for understanding, and to either optimize existing catalysts or design new ones, is important both from an economical and environmental point of view.

A perfect catalyst is active, selective and durable, but reality is that the catalysts are not always perfect. Moreover, the catalyst has to facilitate the reaction at an appropriate rate and under acceptable temperature and pressure conditions in order to be efficient. Lowering the working temperature of the catalyst, as well as the amount of reaction by-products, is a main goal in catalysis recently. If achieved, it can decrease the production costs, energy consumption, the amount of “waste” produced

during a catalytic process, and the amount of catalyst material that is used in the reaction. The latter is significant since industrial catalysts in many cases can involve expensive and scarce materials such as palladium (Pd), platinum (Pt) or rhodium (Rh). Therefore, designing new more efficient and/or cheap(er) catalysts is highly relevant. In order to reach these incentives, it is important to understand how the catalyst works: what are the active sites (not all the atoms/regions of the catalyst are involved in a real catalytic process), their structure and properties, and how they interact with all the reaction participants (reactants, intermediates and products). In addition, for nanoparticle catalysts a lot of research effort is put into understanding what are the optimal size, composition, shape, and surface structure of the nanoparticle to achieve the goal of catalysis by design.[33]

## 1.3 Challenges in characterization of nanosized catalysts and metal-hydrogen systems

Catalysts and catalytic processes are generally complicated: a catalytic reaction can involve multiple steps and is highly dependent on the reaction conditions such as temperature and pressure. Studying a catalyst is, thus, a real challenge: the scientist is always facing a dilemma of how much information about the catalyst one can obtain with a certain technique and how relevant this information can be with respect to a real catalytic process. To simplify the investigation of the catalyst one can use well defined model systems such as supported nanoparticles (e.g. fabricated arrays of nanoparticles) or single crystals, and study them under well-defined ultrahigh vacuum (UHV) conditions. With the help of powerful surface science techniques, this approach has given a lot of valuable insight into catalytic processes, especially for fundamental science. However, there are two major problems with such an approach: first of all, a catalytic reaction may proceed very differently under UHV conditions compared to the real reaction conditions that involve high pressures; this is referred to as the *"pressure gap"*. Secondly, the reactivity is very different for a simplified structure compared to an industrial "real" catalyst; this is referred to as the *"material"* or *"structure gap"*. Consequently, it is not straightforward to relate information obtained in idealized experiments to the catalytic processes occurring under realistic reaction conditions in chemical industry. Therefore, the development of characterization techniques to investigate catalysts and catalytic processes *in situ* or even *in operando* (while the reaction is happening at close-to or identical to real application conditions) is very relevant and, at the same time, a challenging task. *In situ/operando* studies enable identification and understanding of important reaction steps, such as formation of reaction intermediates and the nature of the active sites. Moreover, they can shed light on important stages in catalyst lifetime, e.g. activation/deactivation. Requirements on the ideal *in situ/operando* experimental technique for studies of catalytic processes are very demanding: it should have high spatial (below nanometers) and temporal (ideally down to femtoseconds) resolution and allow simultaneous monitoring of the active site (structure, composition, activity) and the reaction intermediates. At present, there is no existing technique that meets all of the above requirements, and instead it is necessary

to combine several different approaches in order to get a more complete picture. Today, a variety of techniques allow for investigation of either *morphological properties* of the catalyst or *surface chemistry* associated with catalytic process and reaction mechanism. Examples of techniques that enable investigation of structural properties are the ones using electron probes (scanning electron microscopy (SEM), transmission electron microscopy (TEM)), scanning probes (atomic force microscopy (AFM), scanning tunneling microscopy (STM)) and X-rays (X-ray diffraction, X-ray absorption spectroscopy (XAS), small-angle X-ray scattering). The surface chemistry can be probed by the techniques such as infrared spectroscopy (IRS), Raman spectroscopy, neutron scattering (NS), XAS, and deviations like Extended X-ray Absorption Fine Structure (EXAFS) or X-ray Absorption Near-Edge Structure (XANES), electron paramagnetic resonance (EPR), ultraviolet-visible spectroscopy (UV-vis), thermal desorption spectroscopy (TDS), etc. The trade-off between these techniques is that the ones, which offer spatial resolution to resolve morphological properties of a catalyst down to nm scale, do not have sufficient temporal resolution for studies of the fast catalytic events and kinetics of the processes. Therefore, it is also useful to employ theoretical studies and modeling using, for example, density functional theory (DFT), Monte Carlo (MC) simulations, molecular dynamics (MD), to conceptually understand and/or predict the properties of the catalyst and the reaction steps.[34]

Similarly to catalysts, fundamental understanding of metal-hydrogen systems at the nanoscale is obtained by combining experimental and theoretical techniques. No technique existing today fulfils all requirements and, again, there is a trade-off between techniques allowing structural characterization and techniques providing high enough temporal resolution for measurements of metal-hydrogen interaction process kinetics at the nanoscale. Hydrogen absorption results in various changes in the chemical and physical properties of the host material, which allows a variety of techniques to be used for measuring such an event, especially under steady-state conditions. These include X-ray diffraction[35] (change in lattice parameter) and nuclear techniques[36] (changes in neutron scattering length or cross-section), which are possible to use for *in situ* studies of hydrogen absorption in nanostructured metals. Changes in optical properties of the material upon hydrogen absorption have recently become more common for studying metal hydride nanosystems. These optical changes can be revealed in measurements of reflected[37] or transmitted light[38], luminescence[39] and localized surface plasmon resonance[40]. Traditional ways to study metal-hydrogen systems also include volumetric methods (change in $H_2$ gas pressure of a material in a closed volume) and gravimetric methods (change in mass of the system).[25] These methods, however, require relatively large sample volumes, and therefore suffer from problems related to the typically quite broad size distributions of the probed nanoparticles and related inhomogeneous sample material effects.

A generic difficulty when exploring nanostructured materials with the aim of establishing structure-function relationships is that traditional methods rely on *ensembles* of nanoparticles. Nanoparticle ensembles, by nature, are inhomogeneous in terms of size, shape and structure. Thus, ensemble-averaged measurements may mask

individual-nanoparticle-specific details and the "true" factors controlling the mechanism of the studied processes, i.e. how these relate to details in nanoparticle size, shape, structure and composition. This, in turn, may complicate the identification of advantageous structural and/or compositional properties that an optimal particle designed for a specific purpose may have. Therefore, *single particle* studies of catalytic reactions and hydrogen sorption processes performed *in operando* and in real time are of crucial importance for the development of the fields of catalysis and metal-hydrogen systems.

## 1.4 Techniques for single nanoparticle characterization of catalyst and metal-hydrogen systems

Studying nanoparticles is not easy due to their small size; however studying *single* nanoparticles is even more difficult. The experimental method has to provide a very high sensitivity in order to probe such a low concentration of elements and furthermore allow for fast data acquisition that is necessary for transient experiments.

In the last decade, several experimental approaches have become available that allow monitoring catalytic events on single nanoparticles such as electrochemical methods (e.g. electrochemical scanning probe microscopy[41], electrochemical measurements with ultramicroelectrodes[42] or electrocatalytic current amplification via single-nanoparticle collisions[43]), single-molecule fluorescence microscopy[44] and surface-enhanced Raman spectroscopy[45]. These methods can detect the amount of reactants consumed or products generated in a catalytic reaction by a single nanoparticle. The detection scheme is based on the fact that reactants and products in a catalytic reaction can affect, for example, the current in electrochemical measurements (proportional to the rate of reactant consumption or product generation); in the case of fluorogenic reactions, reactants can be transformed into a fluorescent product; or reactants can have distinct vibrational features suitable for detection with Raman spectroscopy.

Other methods, instead, focus on the changes of the catalyst particle itself in their detection scheme, for example, alterations in the oxidation state or coordination environment of the atoms can be monitored by X-ray microscopy[46]. Chemical or physical properties of a catalyst and its surroundings can change due to consumption of reactant molecules and product generation on the catalyst surface. This can be monitored by surface plasmon resonance spectroscopy, which is based on the phenomenon of LSPR. Briefly, LSPR is a coherent oscillation of conduction electrons in metal nanoparticles, which will be discussed in detail in Chapter 2. The LSPR frequency of such a particle depends on its size, shape, material and surrounding environment. For nanoparticles of Au and Ag, which are common plasmonic materials due to their favourable optical properties, the LSPR wavelength is in the ultraviolet-visible-near-infrared (UV-vis-NIR) regime. In this regime, the scattering spectra of an individual plasmonic nanoparticle can be measured with dark-field scattering spectroscopy[47]. In general terms, the LSPR sensing approach is based on detection of changes in LSPR frequency of the sensor particle caused by alterations of the sensor

particle itself (e.g. shape, volume, oxidation state or through transformation into a hydride) or in the surrounding environment of the sensor (direct[48] and indirect[49] sensing). In this thesis, nanoplasmonic sensing (or *plasmonic nanospectroscopy*, as we coined it in the present context) was the main characterization tool used and further developed, and therefore it is discussed in more detail in Chapter 2, which gives a basic introduction to the phenomenon of LSPR, whereas in Chapter 6 the concept of dark-field scattering spectroscopy is introduced in more detail. [50,51]

Another important technique for single nanocatalyst characterization is environmental TEM (ETEM), which is capable of *in situ* studies of chemical processes at the gas–solid interface with atomic scale resolution.[52-54] It should be noted however, that most of the time, the information obtained with ETEM is at gas pressures of few millibars, and not at ambient pressure, which is more relevant for technological applications. Nevertheless, there are possibilities to bridge the pressure gap in ETEM by utilizing nanoreactors that allow atomic-resolution ETEM at ambient pressure and elevated temperature conditions[55]. Recent advances towards *in situ* and *operando* TEM are summarized in ref.[56-58]

Very few single particle studies on hydrogen-metal systems have been performed until recently. These include a first demonstration of LSPR sensing for probing H sorption in individual metal nanoparticles[59,60], as well as studies using *in situ* electron energy-loss spectroscopy (EELS) in ETEM[61-63] and coherent X-ray diffractive imaging (CXDI)[64,65] that were applied for studying hydriding phase transformations of individual Pd nanocrystals. Furthermore, it is my own contributions to the field made as part of this thesis.

## 1.5 The scope of this thesis

This thesis was aimed at studying metal-hydrogen interactions and catalytic reactions at the single nanoparticle level. In order to do this I developed and applied a non-invasive experimental method for probing individual nanoparticles during hydrogen sorption or during a catalytic reaction under *operando* conditions using plasmonic nanospectroscopy. Furthermore, I established the necessary nanofabrication concepts to make samples for such studies.

Specifically, in the first aspect of this work, a nanofabrication method was developed for making plasmonic nanoantenna structures, such as nanodisc dimers and trimers, which are characterized by high field enhancement (advantageous for sensing) in so-called *hot spots* of the antenna (i.e. narrow gaps in the dimer/trimer arrangements). As the key result, the targeted ability of the fabrication scheme to allow placement of a particle of interest (nanocatalyst or hydrogen-absorbing particle) in the plasmonic hot spot was realized. A second fabrication method was developed in order to accommodate various dielectric spacer layers for the protection (through complete encapsulation in a core-shell scheme) of the plasmonic antenna structure. This is a challenging task in terms of fabrication and it becomes important when the nanoantenna is to be used in harsh experimental conditions, such as high temperatures

and aggressive gas environments, and to tailor the surface chemistry and near-field coupling in hybrid-plasmonic photocatalyst materials. As one of the key results, this fabrication scheme is the first demonstration of large-scale nanofabrication of arrays of core-shell nanostructures with widely tailored material compositions in terms of all constituents (beyond what currently is possible by colloidal synthesis[66-68], which is the standard way of making core-shell structures).

In the second aspect of this work, I explored the possibility to probe individual Pd nanoparticles upon their interaction with hydrogen gas and during hydride formation. Firstly, wet-chemically synthesized *single crystal* Pd nanoparticles of various sizes (15 - 70 nm) and shapes (i.e. cubes, dodecahedra, rods, octahedra) were investigated. This was made possible by linking a plasmonic antenna nanoparticle to the Pd particle by means of electrostatic self-assembly in solution, with subsequent deposition of the assembled dimers onto a surface. The behavior of these particle arrangements upon exposure to $H_2$ and during hydride formation was investigated as a function of Pd crystal size and shape. Secondly, the role of grain boundaries during hydrogen sorption in *polycrystalline* Pd nanodiscs was explored. This was done by correlating plasmonic nanospectroscopy measurements of individual Pd nanodiscs with corresponding transmission Kikuchi diffraction (TKD) characterization of their crystallographic properties. Hydrogen absorption in/on Pd was chosen as the (model) reaction due to several reasons. From experimental point of view, hydrogen absorption in Pd occurs at "convenient" conditions, i.e. around room temperature and at pressures below 1 bar. In addition, the hydride formation in Pd is completely reversible, and the kinetics of the process are reasonably fast even at room temperature, since there are no or very low kinetic barriers for hydrogen ($H_2$) sorption and diffusion in Pd. Finally, even though the bulk Pd-hydrogen system is very well studied, there are still open questions about the physics of hydrogen sorption in nanoscale Pd systems. Specifically, detailed studies of the role of Pd nanoparticle size, shape and microstructure on the thermodynamics and kinetics of the hydride formation process have started to emerge only very recently and require further attention[61-65,69]. For example, since most of the work so far has been done on ensembles of Pd nanoparticles, it is unclear if some of the observed effects stem from the intrinsic size/shape properties or due to inherent inhomogeneity of the ensemble particles. One such example is the characteristic slope of the two-phase coexistence plateau that emerges upon nanosizing of the Pd. For polycrystalline nanoparticles, grains can largely influence their properties; however studying grain boundary effects at nanoscale is challenging and only beginning to be explored. In the single particle studies of Pd nanoparticles presented in this thesis, these issues are addressed. At a more general level, deeper understanding of the physics behind these nanoscale size and shape effects and the role of defects can facilitate the development of more efficient hydrogen storage systems and sensor, as well as catalyst materials.

In the third aspect of this work, which is catalysis, the fabricated core-shell nanostructures described above are shown to manifest significant optical absorption enhancement in small catalyst nanoparticles grown on top of them. In addition, photocatalytic reaction rate enhancement, as well as quenching, depending on the

specific system and reactant-mixing regime, are demonstrated for these structures. In the second catalysis-oriented study presented in this thesis, mass spectrometry was combined with *in operando* plasmonic nanospectroscopy of single catalyst nanoparticles. The experimental setup developed for this purpose is a significant step forward for catalyst characterization using plasmonic nanospectroscopy. While the latter offers only information about the state of the catalyst nanoparticle itself or the surrounding medium, addition of mass spectrometry allows the simultaneous analysis of reaction products, which makes it possible to directly correlate catalyst nanoparticle state and its activity or selectivity. The capabilities of the setup are demonstrated both at the ensemble and single particle level.

# 2 NANOPLASMONICS

When light interacts with metal particles with a size smaller than the wavelength of light, it can excite resonant collective oscillations of conduction electrons in the particle - the localized surface plasmon resonance (LSPR). LSPR is established when the frequency of the incoming light wave matches the resonance frequency of the electrons oscillating against the restoring force generated by the induced charge distribution inside the metal particle. The resulting electron displacement causes the formation of a dynamic dipole (Fig. 2.1), which leads to the enhancement of the electromagnetic field around the particle with respect to the incoming field and constitutes a spatially confined *sensing volume* around the particle[47]. The LSPR frequency is known to depend on particle parameters such as size, shape and composition, as well as on the dielectric properties of the surrounding environment. By monitoring the LSPR wavelength of the plasmonic particle it is thus possible to detect changes of the particle itself and also of its surroundings, which is the basis of plasmonic sensing. At the LSPR frequency the particle efficiently absorbs and scatters light. In the next paragraph these effects are briefly described with regard to the metal nanoparticle. This is followed by a short discussion of the role of particle size, shape and material in nanoplasmonics.

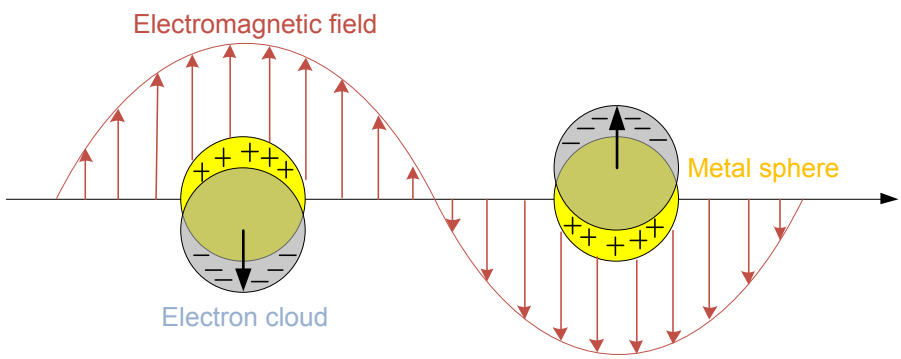


***Figure 2.1***. *Schematic representation of a metal nanosphere during LSPR excitation by an external alternating electromagnetic field at two different times.*

## 2.1 Extinction, scattering and absorption of light in metal nanoparticles

Propagation of light through a disperse medium can be described in terms of two mechanisms: *absorption*, when light is absorbed in the matter, and *scattering*, when light is forced to deviate from a straight trajectory due to the non-uniformity of the medium. These mechanisms can be expressed through respective cross-sections that are defined as the effective areas, which govern the probability of either a scattering or an absorption event. The sum of absorption and scattering gives rise to the so-called *extinction* cross-section.

The German physicist Gustav Mie in 1908 presented[70] an exact solution of Maxwell's equations for an incoming plane wave interacting with a spherical particle of arbitrary size and composition. A full description of these solutions is outside of the scope of this thesis. However, a basic model is useful for understanding how the material in and around the particle influences the LSPR. When the particle with size $a$ is smaller than the wavelength of light $\lambda$, i.e. $a << \lambda$, one can make the so-called quasi-static approximation for solving Maxwell's equations. The approximation implies that the incident electromagnetic field interacting with the particle is constant over the particle volume. For a spherical nanoparticle in the quasi-static limit, the cross-sections for extinction, scattering and absorption can then be described by the following expressions[71]:

$$C_{ext} = 4\pi k a^3 \cdot Im\left\{\frac{\varepsilon_p - \varepsilon_m}{\varepsilon_p + 2\varepsilon_m}\right\} \tag{2.1}$$

$$C_{sca} = \frac{8\pi}{3} k^4 \cdot a^6 \left|\frac{\varepsilon_p - \varepsilon_m}{\varepsilon_p + 2\varepsilon_m}\right|^2 \tag{2.2}$$

$$C_{abs} = C_{ext} - C_{sca} \tag{2.3}$$

where $k$ is the wave number ($k = 2\pi/\lambda$), $a$ is the radius of the particle, $\varepsilon_m$ is the dielectric function of the surrounding medium, and $\varepsilon_p$ is the dielectric function of the metallic nanoparticle. As can be seen from Eq. 2.1 - 2.3, extinction scales as the particle volume ($a^3$) and scattering scales as the particle volume squared ($a^6$). It is also apparent that the scattering and absorption of the particle are influenced by the dielectric functions of both the particle itself and its surrounding medium. As follows from Eq. 2.1 - 2.3, the maximum in scattering and extinction cross-sections should occur at the condition:

$$\varepsilon_p + 2\varepsilon_m = 0 \tag{2.4}$$

which is the resonance condition for the LSPR.

If one considers a dielectric function of a metal as predicted by the Drude model (which, in brief, uses the simplest approximation to describe the optical properties of metals by assuming that all conduction electrons are delocalized):

$$\varepsilon_p = 1 - \frac{\omega_p^2}{\omega^2 + i\gamma\omega} \tag{2.5}$$

where $\omega_p$ is the plasma frequency of a metal, i.e. the frequency below which the reflectivity of any metal is equal to unity for frequencies of the external perturbation. Then combining the last two equations (Eq. 2.4 and 2.5) gives an expression for the LSPR frequency:

$$\omega_{max} = \frac{\omega_p}{\sqrt{2\varepsilon_m + 1}} \tag{2.6}$$

Eq. 2.6 can be re-written in terms of the wavelength:

$$\lambda_{max} = \lambda_p\sqrt{2\varepsilon_m + 1} \tag{2.7}$$

where $\lambda_p$ is the wavelength corresponding to the bulk plasma frequency of the metal. From the latter expression it is clear that the wavelength position of the LSPR will depend on the dielectric function of the particle surroundings, as well as on changes of the plasma frequency (or, in other words, electron density) of the particle. This is the fundamental effect exploited by nanoplasmonic sensing.

## 2.2 Dependence of LSPR on shape, size and material of the nanoparticle

### 2.2.1 Shape

Particle shapes other than a sphere can be efficiently used to tune the LSPR over a wide wavelength range. Nowadays, with advances of nanotechnology, it is possible to prepare nanoparticles of a variety of different shapes and sizes and their optical properties have to be calculated using different theoretical tools (other than Mie theory). Theoretical modeling of nanoparticles with arbitrary shapes and sizes provides better understanding and improvement of current LSPR sensing schemes (as well as other incentives of nanophotonics). There are several techniques available that allow for calculations of different particle shapes and sizes. Examples are discrete dipole approximation (DDA), finite difference time domain (FDTD) method, T-matrix method, the multiple multipole method, and the modified long wavelength approximation (MLWA). [72,73]

The DDA method has been basis of many papers that analyze various particle shapes and their advantages for LSPR sensing. For example, Jain *et al.*[74] calculated optical properties of Au nanoparticles in the form of nanospheres, nanorods and nanoshells for the purpose of applications in biological imaging and biomedicine. In another paper by Hao *et al.*[75] the shape effect was considered in Ag nanoparticles by comparing a triangular prism, a rod and an oblate spheroid. Other shapes that have been studied are nanostars[76], nanorice[77], nanoeggs[78] and nanocups[79].

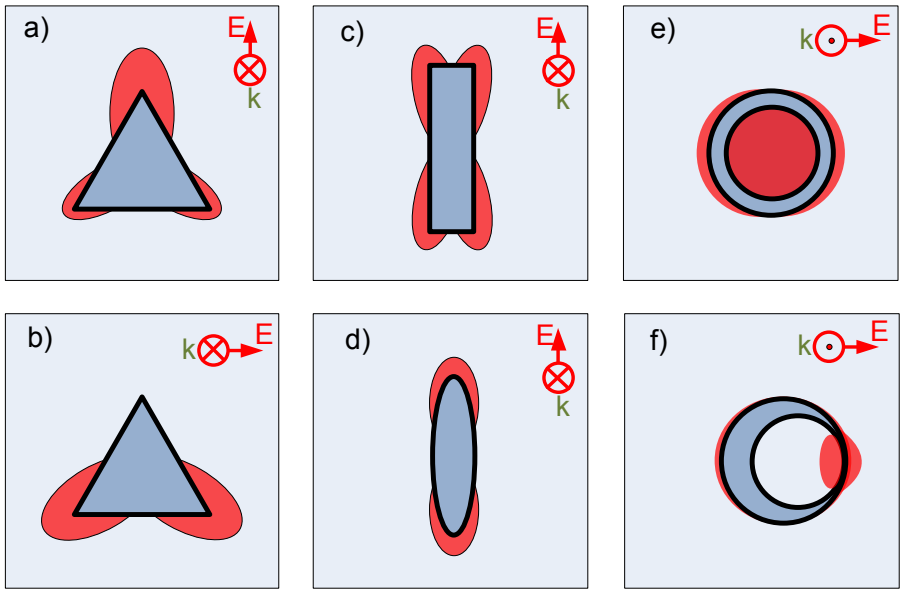


***Figure 2.2.*** *Schematic representation of plasmonic hot spots for different nanoparticle shapes in terms of electric field enhancement: (a) and (b) triangular prism with polarisation of the exciting field along two different symmetry axes; (c) and (d) rod and prolate spheroid with polarisation of the exciting field along their long axes; (e) and (f) nanoshell and nanoegg. Pictures are adapted from Hao et al.*[75] *and Wu et al.*[78]

One important conclusion from computational studies is that there exist so-called *hot spots* in plasmonic nanostructures. These hot spots are the regions on the nanostructure surface or in its vicinity, where there is the largest (for each individual shape) enhancement of the electromagnetic field. Generally, strong field focusing behavior is observed at sharp edges or tips of the nanostructures, and field enhancement tends to increase with prolate shapes. In addition, when the particle has non-symmetrical shape, it becomes important to excite LSPR with the appropriate polarization to obtain the highest enhancement of the electromagnetic field. Fig. 2.2 schematically shows the polarization-dependent electromagnetic field enhancement around different nanostructures. Note that the magnitude of the enhancement can be very different for each case, because it strongly depends on the size and material of the nanostructure,

and its distribution is only depicted schematically. Fig. 2.2 only serves as an illustration of a plasmonic hot spot.

### 2.2.2 Size

If the condition $a << \lambda$ is no longer valid, i.e. the particle size is comparable to the wavelength of light, the following effects arise: 1) the excitation field inside the particle becomes non-uniform; 2) the depolarization fields from a given volume elements of the induced charge experience phase shifts as they propagate across the particle. Both effects give rise to the phenomenon of retardation of the optical field. The retardation phenomenon leads to a lowering of the average depolarization field inside the nanoparticle (giving rise to the red shift of the LSPR resonance with increasing particle size) and appearance of higher order induced multipolar charge distributions besides the dipolar one. The latter modes (quadrupolar, octapolar, etc.) become increasingly significant as the particle size increases as well as with asymmetric particle shapes.

Another effect caused by increasing particle size is a broadening of the LSPR resonance (shorter lifetime) that is caused by energy loss of the radiating dipole via photon emission (light scattering)[80]. The radiative energy loss is proportional to the square of the induced dipole moment, which is proportional to the particle size. This implies that the radiative plasmon decay channel starts dominating with increasing particle size.

The effects accompanying an increase in particle size typically result in a shift of the LSPR to longer wavelengths, and in spectral broadening of the LSPR peak.

In the case of small spherical particles, as follows from Eq. 2.6, the size doesn't matter for determining the spectral position of LSPR, since there is no geometric factor involved. This is, however, not completely true for very small particles (< 10 nm), where the dielectric function of the metal becomes size dependent and surface scattering effects may become appreciable. The volume only determines the magnitude of the scattering and absorption cross-sections. As can be seen from Eq. 2.1 - 2.3, the scattering has a square dependence on the volume, while extinction is only linearly volume-dependent. Therefore, as the particle gets smaller, it is harder to see scattered light from it because with decreasing particle size more and more light gets absorbed.[81]

### 2.2.3 Material

The noble metals Au and Ag are traditional plasmonic materials. This is due to the fact that they have strong and spectrally relatively narrow plasmon resonances at optical frequencies. This can be partly explained by the high electron density of these metals: the more electrons involved in a plasmon oscillation, the higher is the resonance frequency. Another reason is that, at visible frequencies, the losses in Au and Ag are relatively low compared to metals such as copper (Cu), Pd and Pt.

The electron density and intrinsic losses are determined by the electronic band structure of the material, which describes the range of energy (i.e. energy bands) that an electron can have within a solid. At zero temperature, all low energy states up to a certain energy level, i.e. the Fermi energy, will be filled with electrons, and the states above this level will be empty. In contrast to Au and Ag, where the energy bands with the highest density of states (d-bands) are located well below the Fermi energy, the Fermi energy cross the d-band in metals like Pd and Pt. This increases the possibility for interband excitations over the whole UV-vis-NIR spectrum range. The latter leads to stronger damping of plasmon resonance via interband electron-hole pair formation (i.e. absorption)[82]. This is the main reason for the strong damping and low scattering (radiative decay) observed for LSPR in Pd and Pt nanoparticles. In summary, Ag is the best material in terms of the "quality" of its LSPR owing to its intrinsically low losses. Au is not quite as efficient but at the same time more chemically inert and therefore advantageous for applications. This is illustrated in Fig. 2.3, which shows how an unprotected Ag nanoparticle is oxidized after few weeks in air.

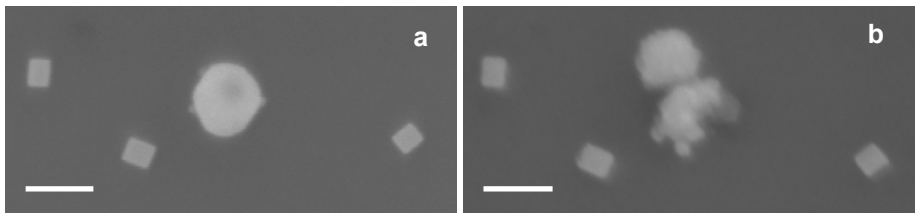


***Figure 2.3.*** *The SEM images of the synthesized Ag nanosphere with three Pd nanocubes around it: (a) as synthesized and deposited on the substrate; (b) after 3 weeks in the storage box. After some time in air, the Ag particle becomes oxidized and its appearance drastically changes. The Pd nanocubes remain visibly unchanged due to their higher oxidation resistance. The scale bar in the SEM images is 100 nm.*

Finally, it is worth mentioning that not only metals can support LSPR but (at infrared frequencies) also metal oxides (e.g. indium tin oxide[83]), and semiconductors (e.g. copper sulfide[84], copper selenide[85]) with appreciable free electron densities, as well as graphene.[86,87] Semiconductors are especially interesting for nanoplasmonics since their free electron concentrations can be tuned by doping, temperature and/or phase transitions. For example, heavily hydrogen doped semiconductors such as zinc oxide and titania ($TiO_2$) have been proposed[88] for creating highly efficient noble-metal-free plasmonic photocatalyst systems. Graphene has already been shown to possess unique mechanical, electric, magnetic and thermal properties,[89] as well as remarkable optical properties.[90] Graphene can support surface plasmons, and, furthermore, the optical properties can be modified by gating, by doping, by chemical means and through functionalization with conventional noble metals.

## 2.3 LSPR in dimers

A large number of theoretical and experimental studies[75,91-99] have demonstrated that there is coupling between two plasmonic nanostructures if they are placed in close vicinity. Qualitative interpretation of this phenomenon can be given based on the simple dipole-dipole interaction model.[92] The electromagnetic field applied to a single plasmonic nanoparticle creates induced surface charges that generate a restoring force on the conduction electrons (Fig. 2.4a) leading to collective harmonic oscillation of the latter, i.e. the LSPR. However, when there are two nanoparticles in close proximity to each other, depending on polarization of the external field, additional forces act on the particle pair, as sketched in Fig. 2.4. If the polarization of the external electric field is parallel to the long axis of the particle pair, the positive charge of the left particle faces the corresponding negative charge of the right particle (Fig. 2.4b). Such induced charge distribution of two adjacent particles creates attractive force between them, resulting in a lower resonance frequency of the coupled system. Contrary, in case of perpendicular external electric field polarization, the induced charge distributions on two particles lead to the repulsive force between them (Fig. 2.4c), which in turn causes an increase in the resonance frequency of the dimer system.

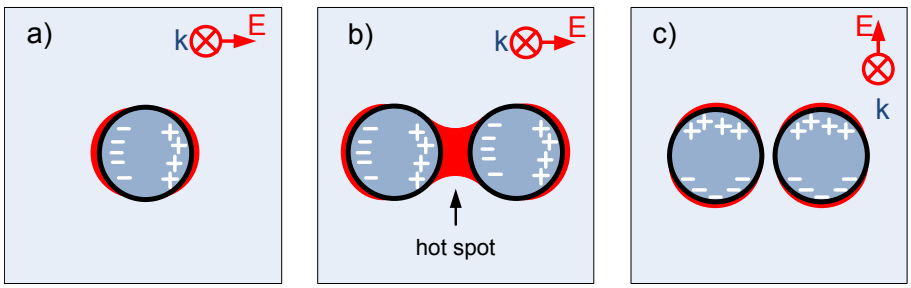


***Figure 2.4.*** *Schematic illustration of the induced charge distribution in (a) an isolated particle, (b) a pair of particles with electric field polarization parallel to their long axis and (c) perpendicular to their long axis (no strong hot spot in the dimer occurs). Pictures are adapted from Rechberger et al.*[92]

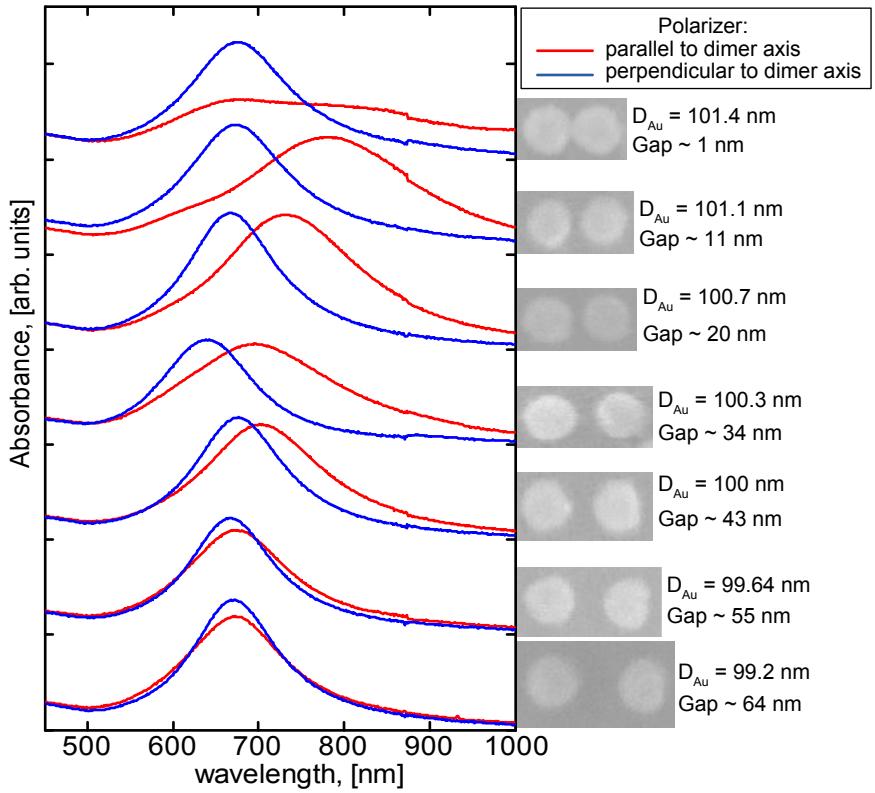


***Figure 2.5.*** *Polarization dependent absorbance spectra of Au nanodisc dimers prepared on glass substrate by HCL, and corresponding environmental SEM images.*

The strongest field enhancement in the coupled particle (dimer) system occurs in the gap between the particles, the so-called *hot spot.* This small area of intense local field is advantageous for LSPR sensing, since it provides strong coupling to anything trapped in the gap, and which will influence the resonance of the coupled system. The magnitude of the field enhancement in the gap of a dimer can be several times higher than the one in/around a single plasmonic particle.[75,100,101] For example, the square of electric field between two closely spaced spheres or triangles is theoretically estimated to be at least a factor of 10 larger than that around respective monomers[75]. The field enhancement in the gap is a strong function of the gap distance (as illustrated in Fig. 2.5, where absorbance spectra of nanodisc dimers were measured using different polarizations of light), and it scales with particle size, i.e. larger particles can give the same enhancements for larger gap sizes. It has also been shown that the plasmon wavelength-shift decays nearly exponentially with increasing inter-particle gap, and that the decay length is independent of the nanoparticle size, shape, the metal type, or the surrounding medium.[102,103] The absolute field enhancement in the dimer gap, as

well as absolute plasmon coupling strength, depend on the shape, size and material of dimer particles. Several particle pair geometries (other than pairs of nanospheres) have been investigated theoretically: pairs of ellipsoidal nanoparticles (spheroids, rods and cylinders)[95] and triangular prisms facing each other tip-to-tip and tip-to-side[75]; or studied experimentally (e.g. pairs of nanoshells[104]). The choice of the dimer particle shape is experimentally often determined by the availability of a suitable fabrication method.

## 2.4 Single nanoparticle plasmonics

There are several experimental approaches that allow for excitation of LSPR in a single nanoparticle, and at the same time are capable of probing the event. These approaches can be divided as far-field and near-field. In the far-field approach the particle is observed from much larger distance than the wavelength of light. In the near-field approach the particle is probed in almost direct proximity to it by a sharp tip or electron beam. The probed phenomenon in the far-field approach can constitute *scattering* (dark field microscopy), *absorption* (photothermal imaging[105]) and *extinction* (spatial modulation spectroscopy[106]) of the particle or *electromagnetic field enhancement* around it (surface-enhanced spectroscopy, e.g. surface-enhanced Raman spectroscopy[107] or second harmonic generation[108] spectroscopy). Consequently, with the near-field approach, the probed phenomenon would be *near-field optical transmission* or *scattering* (scanning near field optical microscope[109]), *photon-induced field-enhanced electron emission* (photoelectron emission microscopy[110], scanning photoionization microscopy[111]), *electron-induced field-enhanced photon emission* (cathodoluminescence[112]) or *energy loss in a transmitted electron beam due to plasmon excitation* (electron energy loss spectroscopy[113] (EELS)).[114]

Far-field approaches are intrinsically diffraction-limited, however their simplicity and robustness still allow investigating distinguished features of plasmonic nanoparticles such as scattering or absorption. Light scattering by the plasmonic particle can be very useful in single particle studies for investigations of materials that have poor scattering properties either due to their electronic structure (e.g. catalytic materials such as Pd or Pt as discussed above) or due to their small size, which also lowers scattering efficiency. These limitations can be overcome by employing the plasmonic particle as an indirect probe by placing it in close proximity to the particle of interest, which itself has weak scattering properties. In this way the plasmonic particle can serve as antenna unit that is sensitive to changes happening in its surrounding environment (i.e. sensing volume)[59,60] (Fig. 2.6). In this thesis dark field scattering spectroscopy was used as one of the main characterization techniques and is described in detail in Chapter 6.

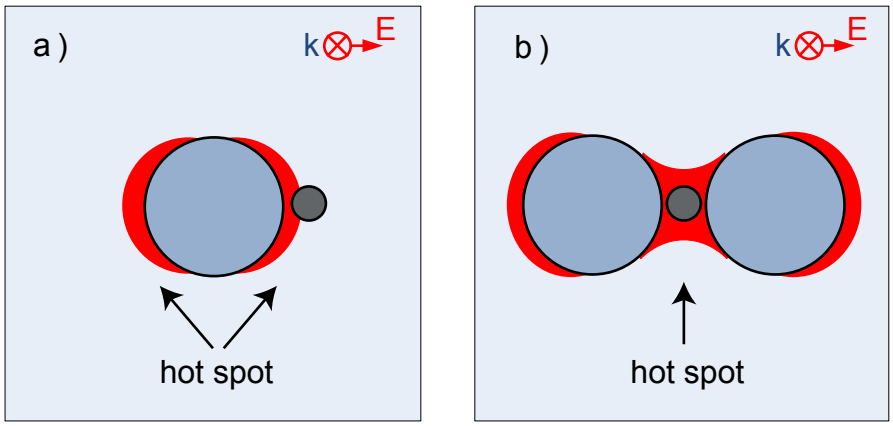


***Figure 2.6.*** *Illustration of the sensing volume of a plasmonic sphere (a) and a pair of spheres (b). By placing a particle of interest (grey) in the hot spot of the plasmonic antenna it is possible to probe the events in/on the particle with the help of the enhanced electromagnetic fields around the antenna.*

## 2.5 Plasmon-assisted light absorption engineering for catalysis

The plasmons decay after light absorption and LSPR excitation. This process occurs either radiatively through re-emission of photons, or non-radiatively by excitation of electron-hole pairs in the metal. The latter results in formation of energetic electrons and holes, which are not in thermal equilibrium and therefore are often referred to as *hot* carriers. The hot electron-hole pair generation process has typically been considered to be detrimental for plasmonic performance because of the consequent plasmon damping, which broadens the intrinsic linewidth of the plasmonic antenna. However, this loss mechanism has gained a lot of attention in recent years due to its potential for extracting and using the hot electrons and holes for applications in energy conversion, photodetection, photochemistry and photocatalysis.[115-118] In photocatalysis, hot electrons present opportunities for light-driven enhancement of catalytic reactions and selectivity control of the catalytic process. Several experimental studies have been performed, where enhanced rates of specific reactions are attributed to the hot-electron transfer to adsorbed species or reaction intermediates on the surface of Ag or Au nanoparticles[119-121] under light illumination. A mechanism where the selectivity of the propylene epoxidation reaction on Cu nanoparticles is controlled by hot electron mediated reduction of surface Cu atoms has also been demonstrated[122]. Recently, it was furthermore reported that hot electrons facilitate dissociation of hydrogen molecules on Al nanoparticles[123]. In all these studies, the plasmonic nanoparticle serves both as a light absorber and as the catalytic surface. However, the choice of Au, Ag, Cu and Al was dictated mainly by their attractive plasmonic

properties rather than catalytic properties. Typical industrial catalysts are instead transition metal nanoparticles (Pt, Pd, Rh, Ru, etc.) in sub-10 nm size range. These metals exhibit plasmonic properties only in the UV range, which does not overlap with the solar spectrum (for harvesting solar energy)[124]. Thus, attempts to combine the best features of the two worlds seem reasonable, and it has been shown that a plasmonic antenna made from a good plasmonic metal such as Au or Ag can increase the optical absorption in adjacent nanoparticles made from a different metal. Specifically this mechanism has been demonstrated theoretically and/or experimentally on examples of a sandwich structure comprised of a large Au nanodisk and large Pd nanodisk[125,126]; a Ag nanodisk and smaller disks of various catalytic particles such as Pt, Rh, Ru, and V[127]; and a Ag nanodisk decorated with sub-5 nm Pd particles[128]. The first attempt to realize this concept experimentally and illustrate its usefulness in photocatalysis was demonstrated recently using Al nanocrystals decorated with small Pd nanoparticles[129]. Strong indications that hot-carrier-induced desorption of hydrogen occurs on Pd surface were observed. In addition, in the presence of acetylene and hydrogen, the selectivity for photocatalytic ethylene production relative to ethane was shown to be strongly enhanced.

Despite intense research, it is still poorly understood how the process of electron transfer to adsorbed chemical species on the nanoparticle surface takes place[130], as well as the actual mechanism of plasmon-induced hot electron generation[131]. Moreover, in many related applications, when analysing the cause of, for example, the observed photocatalytic enhancement, it is important to distinguish between purely plasmonic effects such as hot carriers generated from plasmon decay and near-field enhanced absorption, and non-plasmonic effects[116,132]. Non-plasmonic effects include hot carrier generation by direct photon absorption, which is possible in metal nanostructures. The latter can also reduce barriers for reactions through binding adsorbates[133] and can enhance molecule adsorption via spillover effects[134], i.e. transport of active species (ad)sorbed or formed on one surface onto another surface[135]. In addition, plasmon-induced heating (under sufficient energy flux[136,137]) may thermally activate reactions and contribute to the thermal excitation of carriers trapped in defect sites. In order to clearly distinguish between various effects, careful theoretical modelling and design of experiments are required. The latter can be achieved with well-defined model systems that facilitate direct and unambiguous correlation between enhancement effects and plasmon-influence. In a study by Antosiewicz et al.[128], absorption enhancement was measured from a sample, where Pd catalyst particles are dispersed both in and out of the influence zone of the Ag nanoantenna, which makes it unclear how the LSPR of the Ag particle affects absorption in the catalyst. Motivated by this shortcoming, in **Paper VI** we have developed a fabrication method, which is a modified version of hole-mask colloidal lithography (HCL), where the plasmonic antenna is encapsulated by a few nm thin dielectric layer ($Al_2O_3$, $SiN_x$, $SiO_2$, $TiO_2$) and sub-10 nm catalytic particles (e.g. Pd and Pt) are located on top and only in the influence zone of the plasmonic antenna. In the fabrication process, we prioritized a possibility to use Ag, as plasmonic entity

covered by a protective layer, which is important for the use of Ag in oxidizing environments during catalytic experiments.

# 3 METAL-HYDROGEN INTERACTIONS

Since the first report more than 150 years ago[138] that Pd can absorb H, it has become one of the most well studied materials with respect to H uptake/release thermodynamics and kinetics. This is motivated both from a fundamental and applications point of view. Pd is used for e.g. H storage[48], heat storage[139], metal hydride batteries[140], hydrogen sensors[40], smart windows[141] and switchable mirrors[142]. The bulk Pd-H system has a well-known phase diagram and related electronic structure and optical properties at different H concentrations.[143] Another reason for Pd being an attractive model system is the fact that hydride formation in Pd occurs at convenient experimental conditions such as pressures below 1 bar at temperatures around room temperature.

In this thesis, the fascinating ability of Pd to absorb large amounts of atomic hydrogen is used as a model system. Specifically, Pd nanoparticles are utilized to study the sensing properties of different plasmonic nanoantenna structures (**Paper I, II**). Furthermore, Pd nanoparticles are subject of investigation whether their size and shape influence the thermodynamic and kinetic properties of hydride formation and decomposition (**Paper III**). Finally, we explore the role of grain boundaries in the hydrogenation phase transformation of polycrystalline Pd nanoparticles (**Paper IV**). This chapter is dedicated to the discussion of some of the important general aspects of metal-hydrogen (M-H) interactions (with emphasis on the Pd-H system) that are necessary for understanding the work presented in this thesis.

## 3.1 Bulk metal-H systems

### 3.1.1 H adsorption on the surface

When a metal is exposed to a hydrogen atmosphere, the $H_2$ molecules may adsorb onto the metal surface via physi- and/or chemisorption. Subsequently, the $H_2$ molecules may dissociate and the H atoms get absorbed into the metal. The dissociative chemisorption of $H_2$ molecules is usually an activated process that does not occur spontaneously at ambient conditions on many metals. However Pd demonstrates a high (non-activated) catalytic activity for $H_2$ dissociation on its surface.[144]

Often the equilibrium position of surface atoms differs from the one dictated by the lattice periodicity of the bulk, and this effect is called surface relaxation. It usually

constitutes contraction of the top two layers and appreciable expansion of the second and third, as well as third and fourth layers (atomic planes).[145] The adsorption of an H atom itself can also cause relaxation or reconstruction of the metal surface. After dissociation, there are several energetically different sites that chemisorbed H atoms can occupy depending on the temperature and surface reconstruction, thus forming ordered or disordered (at lower temperatures) surface phases with different coverage[146]. On surfaces with high defect concentration, H prefers the sites of high coordination and near steps, which can actually be useful for probing surface defects[147,148] (more on H-defect interaction in section 3.1.6).

H atoms occupy not only the sites on top of the metal surface, but also directly below and in-between top layer atoms, thus forming a subsurface hydride layer, which constitutes an important intermediate stage between chemisorbed hydrogen and bulk hydride[149]. Fig. 3.1 schematically illustrates the energy landscape encountered by hydrogen molecule/atom approaching a metal surface with indication of energetically different sites that hydrogen can occupy along the way from the gas phase into the metal.

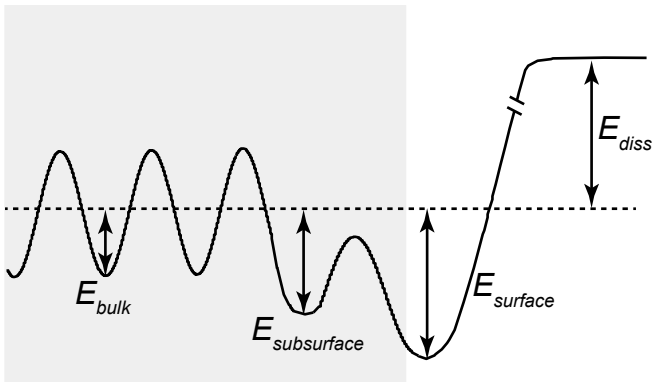


***Figure 3.1**. Sketch of the potential energy landscape for a $H_2$ molecule that approaches a metal surface on the left, dissociates into H atoms and diffuses into the bulk. $E_{diss}$ is the dissociation energy of a $H_2$ molecule, $E_{surface}$ the absorption energy of a H atom at the metal surface, $E_{subsurface}$ the absorption energy at a subsurface site in the metal, and $E_{bulk}$ the absorption energy at a bulk site. Adapted from Behm et al[149].*

## 3.1.2 H-induced lattice strain

When H atoms enter the metal lattice they occupy interstitial sites, which are generally smaller by volume than the size of a H atom. This results in a lattice expansion of the host metal, and the volume change can be expressed as[150]:

$$\Delta V = n_H \Delta v \tag{3.1}$$

where $n_H$ is the number of H atoms dissolved in the metal and $\Delta\upsilon$ is the volume change per hydrogen atom.

The relative volume change of the metal crystal with volume $V$ containing $N$ metal atoms with mean atomic volume $\Omega$ is then:

$$\frac{\Delta V}{V} = \frac{n_H \Delta\upsilon}{N\Omega} = c_H \frac{\Delta\upsilon}{\Omega} \tag{3.2}$$

where $c_H = n_H/N$ is atomic fraction of H atoms.

In face-centered cubic (fcc) metals (such as Pd), H atoms predominantly occupy octahedral (O) and tetrahedral (T) interstitial sites. For a variety of fcc metals and alloys it has been found that the volume change increases linearly with concentration up to 0.7 H/M, and is almost independent of electronic differences or the initial volume of the host metal[151]. The volume change per H atom has been determined to be $\upsilon_H$ = 2.9 Å$^3$. To be more precise[143], depending on the type of the host, its structure and the site occupancy, it is so that i) $\upsilon_H$ is larger for lanthanides than in d-band metals; and 2) in d-band metals $\upsilon_H$ is 2.2 ± 0.3 Å$^3$ for O-site occupancy and 2.9 ± 0.3 Å$^3$ for T-site occupancy. Above 0.7 H/M the volume change does not increase substantially, and Fukai[143] have suggested that it can be related to the formation of superabundant metal-atom vacancies. As a result, the lattice is contracted and extra sites for H are created, which prevents further volume increase.

### 3.1.3 Hydride formation

At low hydrogen gas pressures, a solid solution of H in the host lattice (called the α-phase) is formed. In the α-phase, since the amount of H is rather low and thus the distance between H atoms is large, (attractive) H-H interactions inside the lattice are weak. In this low concentration regime, the system obeys Sieverts' law, which describes the solubility of a gas in a solid solution, assuming ideal gas behavior:

$$\sqrt{p_{H_2}} = n_H \cdot K_S \tag{3.3}$$

where $p_{H2}$ is the partial pressure of $H_2$ gas, $n_H$ is the H concentration in the metal (i.e. H/Pd atomic ratio) and $K_S$ is the Sieverts constant.

As the metal absorbs more and more H, the H atoms will locally strain the lattice of the host. When the H pressure/concentration is increased further, the amount of H in the metal will increase and eventually H-H interactions (resulting from lattice strain and electronic interactions) become appreciable, and the nucleation of regions of the hydride (β-phase) starts. The chemical potential of H in Pd ($\mu_H$) is then composed of four terms[144,152]:

$$\mu_H = \mu_H^0 + RT \cdot ln\frac{n_H}{1-n_H} + \Delta\mu_{H^+} + \Delta\mu_e \quad (3.4)$$

The first term $\mu_H^0$ is the standard potential. The second (configurational) term accounts for the possible atomic arrangements assuming an ideal statistic distribution of the H atoms at octahedral sites ($R$ is the gas constant and $T$ is the temperature). The last two terms describe the deviations from ideal solution behavior, which are to be expected at higher H concentrations in the metal. $\Delta\mu_{H^+}$ denotes the "elastic" contribution coming from the vibrating protons that apply an expansive strain onto the neighboring Pd atoms at the octahedral sites. $\Delta\mu_e$ denotes the "electronic" contribution originating from hydrogen electrons that delocalize upon entering the Pd lattice and interact with its electronic states (and as a consequence the Fermi energy of the metal is raised).

At this stage, the α- and β-phase coexist in equilibrium and an incremental increase in the H concentration around the metal will only result in the growth of the β-phase regions at the expense of the α-phase. Eventually, with continued increase in external H pressure, the entire metal will be transformed into the β-phase, where the hydride formation is complete, and any further increase in H pressure will only result in minor changes in the H content in the hydride.[145] The formed $PdH_x$ has an expanded host lattice structure with a different lattice parameter, varying from 3.89 Å to maximum of 3.894 Å in α-phase and minimum of 4.025 Å in β-phase as a function of hydrogen content. At room temperature, the boundaries of the two-phase region for bulk Pd are at $n_H = 0.008$ for α-phase and $n_H = 0.607$ for β-phase.[144]

A common way to study the H sorption processes is to map (at constant temperature) the H content in the metal versus the increasing applied $H_2$ pressure. In this way, a so-called pressure-composition (*p-C*) isotherm is obtained (Fig. 3.2a). At low H pressures deep in the α-phase region, the isotherm has a slope that obeys the Sieverts relation (Eq. 3.3). The isotherm then exhibits a distinct "plateau" at the pressure where the α- and β-phase coexist, i.e. at the hydride formation pressure. As the temperature is increased, the pressure at which the hydride formation takes place also increases. In this way, by measuring isotherms at several temperatures, the phase diagram of the M-H system can be mapped out. The phase boundaries are located on the low and high concentration sides of the equilibrium plateau, respectively, up to the critical point. At the critical temperature ($T_c$), the phase transition between α- and β-phase becomes 2nd order and the plateau disappears. From the isotherm measurements one can obtain useful information about the hydrogenation process, such as change in enthalpy ($\Delta H$) and entropy ($\Delta S$) during the hydride formation or decomposition. The temperature dependence of the plateau pressure is described by the Van 't Hoff equation[144]:

$$ln\left(\frac{P}{P_0}\right) = -\frac{\Delta H}{RT} + \frac{\Delta S}{R} \quad (3.5)$$

where $P$ is the plateau pressure, $P_0$ is the atmospheric pressure. $\Delta H$ and $\Delta S$ can be found by constructing a Van 't Hoff plot (Fig. 3.2b), i.e. by plotting $ln(P/P_0)$ versus $1/T$, which yields a straight line. Then, $\Delta H$ corresponds to the slope, and $\Delta S$ to the intersection with the pressure axis, respectively.

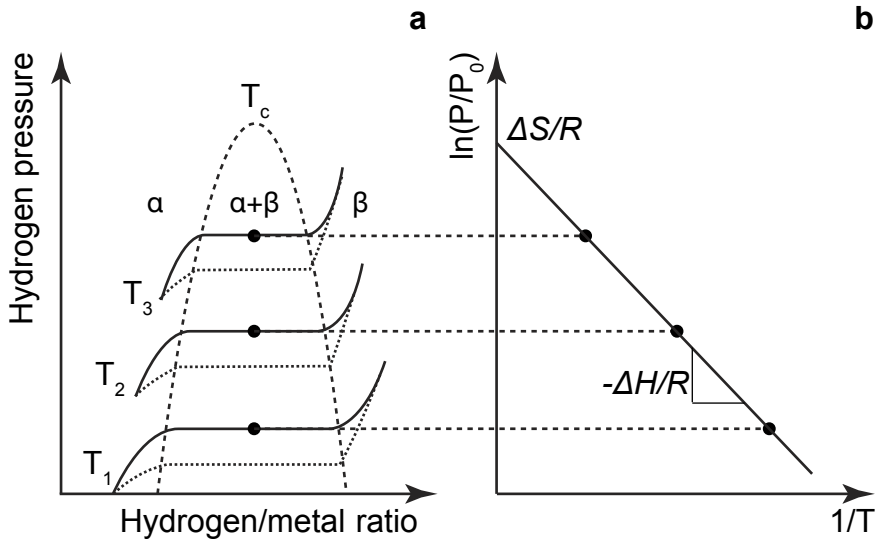


***Figure 3.2.*** *(a) Sketch of typical p-C isotherms measured at different temperatures, which allows mapping the phase diagram of the hydride formation/decomposition (note that the H pressure axis has a log scale). The boundaries of the two-phase region are denoted with the dashed curve. The hydride formation is reversible (dotted line), however the plateau pressure of hydride decomposition often occurs at lower pressure resulting in hysteresis. (b) Sketch of a typical Van 't Hoff analysis of hydrogen absorption isotherms, where the equilibrium plateau pressures are plotted against the inverse temperature. The Van 't Hoff plot reveals information about ΔH (proportional to the slope of the straight line) and ΔS (proportional to the intersect with the pressure axis) of hydride formation/decomposition.*

### 3.1.4 Accuracy of Van 't Hoff analysis and entropy-enthalpy compensation

It is important to note that Van 't Hoff analysis can be problematic in reality. Since the values for $\Delta H$ and $\Delta S$ are extracted from the plot of the plateau pressure as a function of the inverse temperature, the inaccurate determination of the plateau pressure (note that the y-axis is logarithmic) can largely contribute to the uncertainty of the analysis. This is especially relevant when experimental isotherms exhibit sloping plateaus and non-closing hysteresis loops. Another source of uncertainty is the quality of the fit in the Van 't Hoff analysis. An imprecise regression in the Van 't Hoff plot will cause

correlated errors in $\Delta H$ and $\Delta S$, that is, an error in the slope ($\Delta H$) measure is directly reflected in the intercept ($\Delta S$) measure. The phenomenon of correlation in the dependence of the enthalpy and entropy on governing parameters is called enthalpy and entropy compensation, and it may also arise if the temperature range of the experiment is very narrow[153]. The linear correlation between $\Delta H$ and $\Delta S$ follows immediately from $\Delta H - T\Delta S = \Delta G \sim$ constant ($G$ is Gibbs free energy). The slope of this linear relationship $\delta\Delta H/\delta\Delta S$ is the so-called compensation temperature $T_{comp}$, at which all plateau pressures have the same value $p_{comp}$. $T_{comp}$ falling within the range of temperatures used in the experiments is a strong indication that the observed correlation is a statistical artefact. The enthalpy and entropy compensation effect was comprehensively illustrated on example of many recent studies regarding H interaction with Pd nanoparticles[154].

### 3.1.5 Hysteresis

If one reverses the hydrogenation process by decreasing the H pressure from the hydride, the decomposition process will take place in a similar way as the hydride formation described above, and exhibit a plateau where β-phase and α-phase are in thermodynamic equilibrium as the hydride is decomposed. However, the hydride decomposition will in most cases not occur at the same pressure as the formation, but rather at a lower pressure (Fig. 3.2a). Several concepts explaining the origin of the pressure hysteresis in M-H systems have been proposed since its discovery[21,155-159]. At present, there are two commonly recognized theories. According to the first, the hysteresis is attributed to the loss of energy due to formation of dislocations, which are required in order to accommodate the volume changes (expansion/contraction) in the metal, both during absorption and desorption of hydrogen[160-162]. In order to explain the reproducibility of the hysteresis, the theory makes the somewhat debatable assumption that dislocations are annihilated after each hydride formation cycle at the same rate as they are formed. This is to accommodate for the fact that the density of dislocations cannot be increased above a certain saturation point. According to the second, more recent theory, it is proposed that the lattice stresses and strains generated by incorporation of hydrogen into a host metal also create an energy barrier that needs to be surmounted in order for the hydride to form or decompose.[163] However, this is strictly valid only for an open system with coherent interfaces between metal and hydride phase. Coherent transformation implies that during absorption of hydrogen into the metal, the host lattice is not disrupted (e.g. by dislocation formation and movement) but is under significant stress, which leads to elastic energy contributions to the enthalpy (Fig. 3.3a). The elastic energy barrier is proportional to the sample volume and cannot be overcome by thermal fluctuations. In contrast, during incoherent transformation (Fig. 3.3b), dislocations are created in order to relax and thus minimize elastic stresses, and incoherent precipitates nucleate and grow in the corresponding phases (i.e. β-phase during absorption and α-phase during desorption process).

The extent of the hysteresis can be engineered by pre-straining the host metal lattice. Typically this is done be reducing the size of the metal to nanoscale or by alloying the

host metal with a second element, as for example in Pd-Au, Pd-Ag, and Pd-Ni alloys.[164-166]

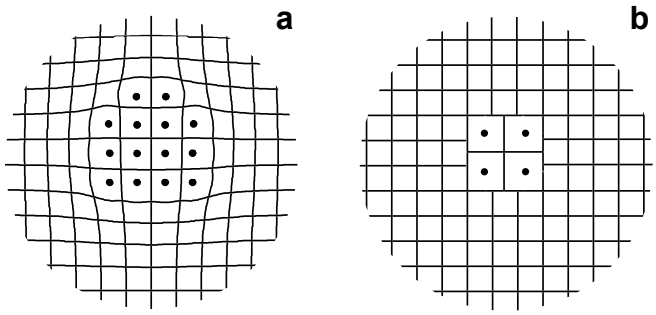


***Figure 3.3.*** *(a) Sketch of coherent and (b) incoherent phase nucleation (dots indicate sub-volumes with interstitial atoms). During the coherent process, there is continuous variation in the lattice spacing, so that coherency strains start to develop. During the incoherent process, dislocations are readily created to minimize elastic stresses, and there is little or no lattice matching across the interface between the matrix and precipitate. Adapted from Wagner[167].*

## 3.1.6 Role of defects in M-H interactions

The properties of a material are strongly affected by its microstructural characteristics. As mentioned earlier regarding surface adsorption, H atom adsorption/absorption is sensitive to the presence of defects, especially at low H coverage[146]. It is known that H is trapped in lattice defects such as vacancies[168], dislocations[169] and grain boundaries[170]. This can be explained by the larger binding energy at the defect site compared to the interstitial site[168]. Hydrogen is not only trapped in the defects, but can also introduce new defects into the metal, for example vacancies[143] and dislocations[171]. In the following, some of the defects that interact with hydrogen are summarized.

### 3.1.6.1 Vacancies

Vacancies are the simplest form of point defects and correspond to lattice sites with a missing atom. They can be created during solidification due to imperfect packing. Vacancies can be formed also during processing at elevated temperatures due to atom displacement by thermal vibrations. The number of vacancies $n_v$ increases exponentially with temperature as[172]:

$$n_v = Ne^{-E_v/k_BT} \tag{3.6}$$

where $N$ is the total number of lattice sites, $E_v$ is the energy required to form a vacancy, $k_B$ is the Boltzman constant. Hydrogen is easily trapped in vacancies due to

favorable energy conditions. For this reason, they are sometimes regarded as internal surfaces.

### 3.1.6.2 Dislocations

Dislocations are linear defects that involve misalignment of the atoms in the lattice structure. They are important since they provide mechanisms that allow for mechanical deformation and thus determine the strength and ductility of the metal. Dislocations can be of edge, screw or mixed type (Fig. 3.4). Edge dislocations are defects, where an additional half-plane of atoms is introduced in the crystal lattice, thereby distorting its atomic planes. The screw dislocation has its name due to the spiral surface formed by the atomic planes around the screw dislocation line. Mixed dislocations are intermediate between the edge and screw dislocation, and illustrate that it is possible for a dislocation to change its character inside the crystal as shown in Fig. 3.4c. An important characteristic of a dislocation, is that it cannot end inside the crystal, but must end at a surface such as grain boundary or the crystal surface.[172]

The edge dislocations are of primary importance for M-H systems, since they strongly interact with hydrogen atoms and influence plastic flow and H mobility[168]. For the Pd-H system, the interaction with dislocations results in increased solubility in the α-phase[169]. Interstitial sites in the expanded regions due to edge dislocations serve as hydrogen traps, where hydrogen atoms accumulate. Dislocations not only interact with H, but can be formed during hydrogen loading and/or unloading[160]. This occurs in order to accommodate the lattice mismatch between metal host and precipitate.

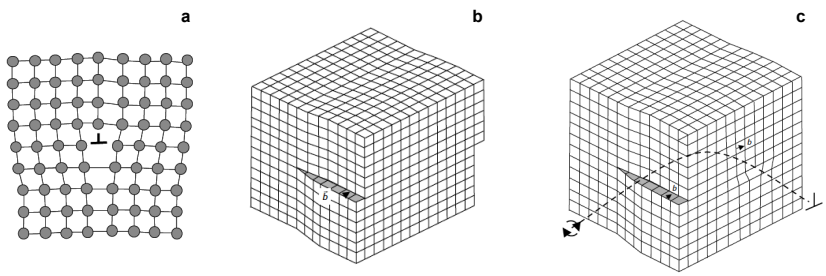


***Figure 3.4.*** *(a) Edge dislocation, (b) screw dislocation and (c) mixed dislocation.* $\vec{b}$ *is the Burgers vector. Adapted from Campbell*[172].

### 3.1.6.3 Grain Boundaries

A grain boundary is a two-dimensional defect constituting an interface between two grains (crystals) in a polycrystalline material. Since atomic bonds at the grain boundary act as a conjugation interface between the two grains, atoms within grain boundaries are subject to high strain and distortion. This results in different energetic states, rendering the properties of the grain boundaries different from the crystal interior. Since grain boundaries are regions with many irregularly placed atoms,

dislocations and voids, they can serve as sinks for disappearance of vacancies and dislocations.

The crystals on either side of the grain boundary differ only in their orientation. Hence, grain boundaries can be categorized to the extent of their misorientation such as low-angle grain boundaries (LAGBs) and high-angle grain boundaries (HAGBs). The misorientation angle for LAGBs is less than about 15°, and correspondingly more than that for HAGBs[173]. In comparison to HAGBs, LAGBs have less severe defects, obstruct plastic flow less and are less susceptible to segregation of alloying components. Twin boundaries can be regarded as a special type of grain boundaries with high symmetry, where often one grain is a mirror image of the other. Twin boundaries are usually flat and have lower energy than HAGBs, therefore they are less effective as sources and sinks of other defects and are less active in deformation and corrosion.[172]

Grain boundaries are preferential regions for accumulation and segregation of many types of impurities, as well as phase precipitation or absorption of species such as hydrogen and oxygen. Grain boundaries were extensively studied in the context of M-H interactions using materials with high density of grains such as nanocrystalline Pd (n-Pd), where the size of the grains is less than few tens of nm. For n-Pd, where the mean grain size is 10 nm, it has been shown[170,174] that the miscibility gap is narrowed, and according to the proposed model this is due to the fact that grain boundaries do not participate in hydride formation. This can be understood in the following way. In order to reduce its total energy the system may interact with solute atoms via grain boundaries, and the solute atoms may accumulate there. At low H concentrations the H atoms fill the low-energy sites offered by the grain boundaries and increase the solubility of the α-phase up to 0.03 H/Pd (compared to 0.015 for polycrystalline Pd-H system). At high H concentrations, only regions that behave bulk-like transform into hydride (i.e. only crystal interiors and not grain boundaries). This results in decreased solubility in the β-phase down to 0.44 H/Pd (compared to 0.58 for polycrystalline Pd-H system). Consequently, a narrowed miscibility gap is the result of both changes of the α-and β-phase solubility. In contrast, in a study based on X-ray diffraction experiments[175], it was shown that the entire sample volume of n-Pd is readily transformed into hydride, including grain boundary regions. The narrowing of the miscibility gap was in this case attributed to the larger ratio of entropy to enthalpy of mixing in the n-Pd compared to polycrystalline Pd.

Finally, accumulation of H at grain boundaries results in large stresses in the grain interior. At large interface-to-volume ratio (as is the case for n-Pd), this stress causes significant nonlocal interaction between interfaces and bulk[176]. The grain boundary stress in Pd-H expands the crystal lattice, and the bulk hydrogen concentration at equilibrium is affected. As we demonstrate in **Paper IV**, also for polycrystalline Pd nanoparticles, the strain generated by the grain boundaries affects their chemical potential, and correspondingly their hydrogen absorption pressures.

## 3.2 Metal-hydrogen systems at the nanoscale

Reducing the size of the M-H system to the nanoscale has immediate effects on its chemical and physical properties. The surface-area-to-volume ratio increases and the role of microstructural components such as surface and subsurface sites, grain boundaries, interfaces and other defects becomes significant. This is because their number becomes comparable with the total number of sites in the system. Surface tension gains a prominent role in the hydrogen absorption properties of the material. Since nanosystems usually have to be deposited/dispersed on substrates to avoid immediate aggregation/sintering and in many cases are stabilized by surfactants[177] (remaining from colloidal synthesis) or infiltrated into a scaffold material[69,178], their influence on the M-H system has to be taken into consideration. In addition, the kinetics of hydrogen loading can be improved due to shorter diffusion lengths, and hydrogen loading becomes possible even for metals with low hydrogen diffusivity. Nano-sized metals can be classified as thin films (1D), rods or wires (2D), nanoparticles and clusters (3D).[25] Here, I will focus on nanoparticles and clusters.

Strong size effects are typically expected and have also been experimentally observed for Pd nanoparticles smaller than 10 nm. At these length scales, one of the key factors resulting in the dependence of the thermodynamics on the particle size is surface tension, which gives rise to a decrease of the H binding energy via compression of the Pd lattice as nanoparticle size decreases[179]. Moreover, for such small nanoparticles, the fraction of atoms that reside on corners or edges is significant. These atoms are less coordinated and therefore exhibit higher reactivity toward hydrogen.[26] Furthermore, strong indications of the important influence of subsurface sites have been found[180,181]. The effects of decreasing Pd nanoparticle size on hydrogen storage properties have been studied for sizes that range from 1 nm to 8 nm. Various effects were observed including: a suppression of the critical temperature with decreasing particle size[182,183], decrease in width of the plateau[181-185], increased slope of the plateau and decreased hysteresis[181,184-187], as well as faster kinetics[188]. Recently[39] size-dependent trends in thermodynamics and kinetics were observed also for unexpectedly large Pd nanoparticles with sizes ranging from 14 to 110 nm. However, as was mentioned earlier in the Section 3.1.4, such observations could be related to the fact that the isotherms in this study have strongly sloping plateaus and non-closing hysteresis loops (for smaller particles) leading to imprecise Van ‘t Hoff analysis. Importantly, all these studies were done for ensembles of nanoparticles.

## 3.3 Single particle studies of metal hydrides

For a better understanding of the role of nanoparticle-specific features in the hydride formation/decomposition process, it is useful to perform single particle studies to completely avoid ensemble-averaging effects. Wet-chemical synthesis of nanocrystals[177] allows fine-tuning of the size, shape and crystal facets of the particle of interest, consequently facilitating studies that directly correlate particle specific features related to size or shape with particle functionality. To this end, a significant

number of studies has been published recently, investigating both ensembles[39] of and single[61-65] Pd nanoparticles, which in most cases were single crystalline.

Probing H sorption in metal nanoparticles is challenging in general and even more so for single particles. The studies in the literature attempting such investigations use diverse techniques in order to measure H in Pd nanoparticles, such as electron energy-loss spectroscopy (EELS) in environmental TEM[61-63] and coherent X-ray diffractive imaging (CXDI)[64,65]. Ensemble measurements[39] on 14 - 110 nm particles (predominantly nanocubes, measured at temperatures between 295 and 385 K) showed that absorption and desorption isotherms exhibit sloping plateaus and non-closing hysteresis loops, and their analysis leads to conclusion of size-dependent thermodynamics. The authors argue that this is a consequence of a thermally driven first-order phase transition with incoherent coexistence of α- and β-phases. In addition, they suggest that a free energy barrier is responsible for the observed size-dependent hysteresis width. This strongly contrasts the results from an EELS-based single particle study[61] performed on the same kind of Pd nanocubes but with smaller size (13 to 29 nm) and measured only at 246 K. There it was found that the absorption isotherms exhibit flat plateaus and that they are consistent with a coherent absorption process without coexistence of two phases. The size dependence of the absorption plateau pressures was explained by coherency strain induced by a subsurface hydrogen layer. In a follow-up study by the same authors[63], the hydrogen absorption process was directly visualized in the environmental scanning TEM for an extended particle size range (15 to 80 nm). The authors suggest that the coherent phase transition during hydrogen absorption prevails even for particles, which are at least 80 nm. The reason for this surprising result (surprising due to the very high energy barrier predicted for a coherent phase transformation in such large particles[163]) is that the hydride phase nucleation and growth process does not follow the spherical shell mechanism previously suggested[61], but rather a "hydride cap" is formed that grows across the crystal and creates a linear interface between α-and β-phases. Consequently, it is less energetically costly to maintain a coherent interface between α-and β-phases even for nanoparticles larger than 35 nm and dislocation formation is not triggered. This is in line with a recent mean field model[154], which captures quantitatively most of the latest work on Pd nanoparticles and from which robust and generic patterns regarding the size dependence of the hysteresis during hydride formation in Pd nanoparticles can be extracted. The model proposes coherent hydrogen loading process but an incoherent unloading process. The results of our work presented in **Paper III** and **Paper IV** corroborate this model in terms of the dominant role of elastic lattice strain in the hydrogen absorption process in Pd nanoparticles.

## 3.4 Nanoplasmonic H sensing of metal hydrides

Recently, the interest in studying the Pd-H thermodynamics and kinetics by means of nanoplasmonic sensing has advanced from conventional thin films and arrays of Pd nanostructures to the single particle level. However, the investigation of a small Pd nanoparticle on its own is complicated by its low scattering efficiency, and by large

intrinsic damping that broadens its resonance profile[82] and prohibits the use of dark-field scattering spectroscopy otherwise typically used for single particle experiments. These issues may be overcome by the concept of the plasmonic nanoantenna, which can significantly enhance nanoscale optical effects. The principle is that the antenna unit should be able to detect changes experienced by the nanoparticle of interest. In case of $H_2$ absorption in a Pd nanoparticle, there are two pronounced effects, namely, alterations in both structural (lattice expansion) and electronic properties (change in dielectric function) of the nanoparticle.[101] These changes can be detected through the coupling between the plasmonic antenna and the H-absorbing particle.

The first attempts on single particle sensing of the hydrogenation process by means of nanoplasmonics were made by Liu *et al.*[59] and Shegai *et al.*[60] Both studies were aimed at lithographically fabricated single Au-Pd heterodimer arrangements such as Au triangle – Pd disc and Au cone with Pd or magnesium (Mg) particle on top, respectively. Although the two approaches demonstrated powerful constructions of well-organized nanostructures at surfaces, they did not provide deeper insight to the understanding of the corresponding physics of the M-H interactions. The concept of nanoplasmonic hydrogen sensing was taken one step further in this thesis as demonstrated in **Papers III** and **IV**, where the influence of size, shape and defects on hydride formation thermodynamics is studied on individual single- and polycrystalline Pd nanoparticles.

# 4 NANOFABRICATION

Nanofabrication is the process of making functional structures with at least one dimension that has the size of 100 nm or less. Ever since it has evolved from microfabrication, a large number of different nanofabrication methods have been developed. Generally, one can distinguish two fabrication approaches known as "top-down", when bulk material is cut, milled and shaped into desired nanostructures with the help of externally controlled tools; and "bottom-up", where nanostructures are built using chemical and physical properties of atoms, molecules or colloidal particles to self-assemble into useful conformations. These two approaches, in turn, can be divided into three major classes in terms of patterning the final structure: pattern writing, pattern replicating and self-assembly techniques. Each of these classes will be briefly described below.

## 4.1 Pattern writing techniques

These techniques allow "writing" of the structures on the surface with high flexibility in terms of structural shapes and patterns. Charged beams of ions (in focused ion beam lithography) or electrons (in electron beam lithography (EBL)) can be focused into extremely small volumes to perform structuring of the bulk material either by exposure of energy-sensitive polymer resists or by removing material directly. The current resolution limit of these two methods is of the order of 5 - 30 nm. In scanning probe-based lithographies (SPL), which include several techniques (e.g. lithographies based on STM, AFM, spin-polarized STM and dip pen nanolithography), the microscopic or nanoscopic stylus moves mechanically across the surface to form structures with sizes less than 5 - 10 nm. It is in some cases with SPL possible to manipulate individual atoms. The key limitation of these pattern-writing techniques is a very low throughput, which is accompanied by expensive and complicated equipment. [189]

## 4.2 Pattern replicating techniques

The common feature of these methods is that they all use templates or masks in order to reproduce predefined micro/nanostructures. In photolithography (PL) the mask is patterned by irradiating photons onto a layer of photoresist coated on the substrate surface, which is thereafter developed to form planar structures. Nano imprint lithography is a method where nanopatterns are created using mechanical deformation

of imprint resist (typically, nanoimprinting polymers can be cured by heat or UV light) and subsequently processed to remove excess material (e.g. demolding or etching)). In ion projection lithography (IPL) and electron projection lithography, a broad ion (hydrogen or helium) beam or electron beam is projected through a stencil mask to expose the resist material. As opposed to pattern writing techniques, these methods are characterized with high throughput of structured surface. Their resolution limits are quite reasonable and steadily pushed forward (currently, well below 100 nm). However, these methods have low flexibility if tuning of the structure parameters is required, because every new configuration has to be done with a new mask or template. For example in IPL, the masks are also difficult to make, inspect and repair.[189]

## 4.3 Self-assembly techniques

The previously described two methods are top-down methods, and the available fabrication tools always limit their resolution. On the other hand, self-assembly techniques employ nature's own ability to produce extremely complex living organisms "from scratch" by self-organization and self-construction. The aim of these techniques is first of all to achieve nanostructures in true nanoscale (molecule level) and secondly (and as important as first) at low cost. According to a classification made by Zhirnov *et al*[190]:

- chemical self-assembly covers molecular-scale ordering of compounds with precisely designed atomic architectures into more macroscopic structures;

- physical self-assembly concerns the ordering of atoms resulting from physical deposition processes such as molecular beam epitaxy or chemical vapour deposition (CVD);

- colloidal self-assembly refers to the processes by which nanoparticles aggregate into clusters within the tens of nanometer to tens of micrometer range.

In this thesis, two types of nanostructures were fabricated and studied: the ones nanostructured via colloidal lithography and the ones made by wet-chemical synthesis. These techniques will be discussed in the following sections.

### 4.3.1 Colloidal Lithography

A large part of this thesis was dedicated to the development of nanofabrication methods that are based on colloidal self-assembly or rather, colloidal lithography (CL) in order to be able to build complex plasmonic nanostructures with a catalyst or hydride-absorbing nanoparticle in the hot spot (**Paper I**) or core-shell nanostructures comprising plasmonic nanoantenna encapsulated in the dielectric shell with catalyst particles on top (**Paper VI**). CL uses particles synthesized via wet chemistry (e.g. emulsion polymerization or sol-gel synthesis). These colloidal particles are characterized by their ability to form large surface area 2D or 3D arrays with a certain

level of order: from highly ordered closely packed patterns (often referred to as "colloidal crystals") to sparse monolayers with short-range order. These particle patterns can be used for the development of evaporation or etching masks. CL has attracted much attention due to its relative processing simplicity, low cost and impressive flexibility. The resulting patterns can be controlled by simply varying colloidal particle size, separation and processing conditions. Colloidal particles may be synthesized with desired chemical or physical properties, in order to functionalize them for intended purposes. Processing of CL patterns does not require advanced and expensive tools. The parallel nature of the self-assembly process also makes it suitable for patterning large sample areas (~ $cm^2$). The feature size of resulting nanostructures can be obtained with resolution of few tens of nanometers, and moreover several shapes that are not trivial to produce with EBL can be easily achieved (e.g. cones, hollow cylinders or rings and crescents). All these factors make CL a versatile and cost-effective nanofabrication method. [189-192]

#### 4.3.1.1 Hole-mask colloidal lithography

Hole-mask colloidal lithography (HCL) is a CL variation developed by Fredriksson *et al*.[193] The essential feature of this method is the presence of a sacrificial layer on the substrate surface prior to deposition of colloidal particles. A thin film layer evaporated on top of the colloidal particles (which are subsequently removed) has motivated the name "hole-mask" for this method. The hole-mask is used for evaporation and/or etching that defines parameters of the final structure, and then it is removed with the help of the sacrificial layer in a lift-off process. HCL allows nanofabrication with a broader range of materials and material combinations, and a variety of new nanoarchitectures that can be easily realized as compared to other versions of CL, e.g. nanosphere lithography and sparse colloidal lithography. [193,194]

The specific HCL fabrication steps utilized in this thesis to prepare nanostructures on a substrate are briefly summarized below and accompanied with a sketch for each step (Fig. 4.1):

***Step 1***: Substrates are cleaned with step-by-step sonication in acetone, isopropyl alcohol (IPA) and methanol. ***Step 2***: Clean substrates are spin-coated with poly(methyl methacrylate) (PMMA) and then soft baked on a hotplate. ***Step 3***: The substrate with the thin PMMA layer is etched shortly in oxygen plasma in order to reduce the hydrophobicity of the surface. ***Step 4***: Water-suspended positively charged polyelectrolyte (poly diallyldimethylammonium (PDDA)) is dispersed on the surface. The substrate is then rinsed with de-ionized water to remove excess of PDDA, and dried with nitrogen flow. PDDA thus forms a very thin positively charged layer on the PMMA surface. ***Step 5***: A colloidal suspension of negatively charged polystyrene (PS) particles is deposited on the surface. Here, the chosen size of the PS particles dictates the diameter of the hole-mask and, consequently, the final fabricated structures. Electrostatic repulsion between the PS particles and attraction between PS and the PDDA-treated surface, respectively, creates an amorphous (no long-range order) PS nanoparticle array. ***Step 6***: A thin film of a material, which is resistant to reactive

oxygen plasma etching, typically Au or chromium (Cr), is evaporated to form the mask layer (10 - 20 nm thick). ***Step 7***: After mask deposition, the PS particles are "stripped" away with tape, which leaves nanoholes in the plasma-resistant film layer ("hole-mask"). ***Step 8***: Reactive oxygen plasma etching is applied to selectively remove the exposed PMMA layer below the holes. The etching creates a partial undercut in the PMMA as clearly seen in the corresponding SEM image in Fig. 4.1f. The depth of the undercut varies with applied etch time and also depends on the size of the PS particles used. ***Step 9***: At this stage, the processing route of HCL can take different directions in order to achieve various nanostructure shapes. For example, nanodiscs can be obtained by simply depositing material through the hole-mask at normal incidence (Fig. 4.1a). Nanocones can conveniently be made if the evaporation is continued until the holes in the mask completely close due to the shrinking of the hole as material is deposited on the rims of the holes (Fig. 4.1b). Nanodisc dimers are obtained by evaporation of the material at two opposite angles from the surface normal (Fig. 4.1c). Note, that due to the hole shrinking when material is deposited on the edges, in this case, it will result in uneven size distribution of nanodiscs in each pair. In order to have even size of the discs in each pair, the angle of evaporation has to be alternated every 5 nm of deposited material.

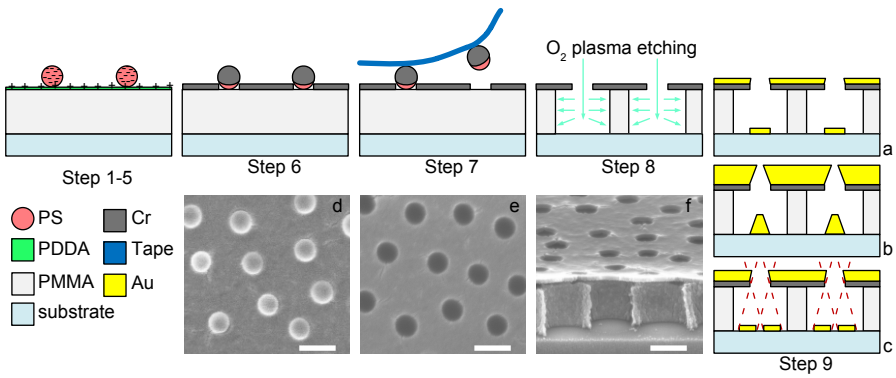


***Figure 4.1.*** *Schematic illustration of the generic HCL evaporation mask fabrication steps 1 - 8. The possible routes after these initial 8 steps in HCL are to, for example, either make: (a) nanodiscs, (b) nanocones or (c) nanodisc dimers in step 9. (d) Top-view SEM image of the sample structure before and (e) after tape stripping. (f) SEM image of the sample cross-section after plasma etching showing the characteristic under-etching of the PMMA resist layer. The scale bar in all SEM images is 200 nm.*

### 4.3.1.2 Shrinking-hole colloidal lithography

Shrinking-hole colloidal lithography (SHCL) is a new variation of CL that I have developed and is covered in full detail in the appended **Paper I**. SHCL is a further development of HCL technique, and it provides unique possibilities for fabrication of self-aligned complex multimaterial nanostructures that are interesting for plasmonics and catalysis applications. In brief, SHCL utilizes the effect of the shrinking hole that

arises from deposition of the material through the holes in the mask prepared by HCL. When material is deposited through the holes in the mask, it builds up not only on top of the mask but also on the rims of each hole, thus causing the shrinking of the holes in the mask layer. Three approaches were developed in order to achieve the shrinking-hole effect and these utilize sacrificial materials such as C and Cr. These strategies are described below:

**C cone approach**

This approach is illustrated on the example of an initial Au nanodisc dimer structure (prepared by HCL), to the gap of which a catalyst particle (e.g. Pd) is "delivered". ***Step 10***: C is e-beam evaporated at normal incidence through the hole-mask and forms a cone due to the successive shrinking of the nanoholes of the mask upon C deposition onto the rims of the hole. The rate and the thickness during C evaporation are carefully controlled to make sure that the holes in the mask do not close completely in order to provide enough space for subsequent deposition of the material that will form the particle to be delivered to the antenna hot spot. ***Step 11***: the particle material (here, Pd) is deposited directly after C at normal incidence through the small hole that is left from the previous step. In this way it forms a small particle on top of the sacrificial C cone structure (Fig. 4.2a). The diameter of the particle is controlled by the thickness of the evaporated C layer (cone height). Evaporating C and/or particle material at a small angle from the normal will, additionally, result in a tunable lateral particle position (Fig. 4.2 e&f vs. g&h). ***Step 12***: the sample is placed in acetone to dissolve the PMMA layer in a lift-off together with all the excess material on top. ***Step 13***: the sacrificial C cone is etched away in mild oxygen plasma. The oxygen radicals thereby attack the C cone uniformly from all directions, such that the particle is delivered into the gap of the gold dimer as illustrated in the sequence of SEM images in Fig. 4.2a-d. The C cone approach works well for delivering the particle of interest into the gap of the nanodisc dimer. The drawback (or equally advantage if an oxide particle is to be delivered) of this method is that oxygen plasma etching, which is used to remove the C, also may oxidize the particle or nanoantenna material (for example when Ag is used).

**Cr cone approach**

In order to eliminate the issues related to unwanted oxidation, Cr can be used as an alternative sacrificial nanostructure material in a second version of SHCL. To illustrate this approach, instead of an Au nanodisc dimer, a single Au nanodisc is used as the initial nanoantenna structure. ***Step 10:*** as shown in Fig. 4.3a, Cr is deposited at normal incidence instead of C to form the sacrificial cone structure. In this way the diameter of the hole in the mask, and thus the size of the final nanoparticle, can again be finely adjusted via the hole-closing effect. ***Step 11***: the material to form the second particle is deposited at an angle from the normal (to avoid deposition onto the Cr cone) through the tuned hole-mask to be delivered to the close vicinity of the antenna disc (Fig. 4.3b). Tuning of the particle evaporation angle will yield various particle positions relative to the Au nanodisc. Alternatively, if e.g. a nanodisc dimer were the initial antenna structure, one would deposit the Cr cone at an angle and then the particle material at normal incidence to deliver the particle to the dimer hot spot. ***Step 12***: the

PMMA layer with excess material on top is removed by lift-off in acetone. ***Step 13***: the Cr cone is removed by dipping the sample in a liquid Cr-etch, leaving only the antenna with a particle in the hot spot on the surface (Fig. 4.3c).

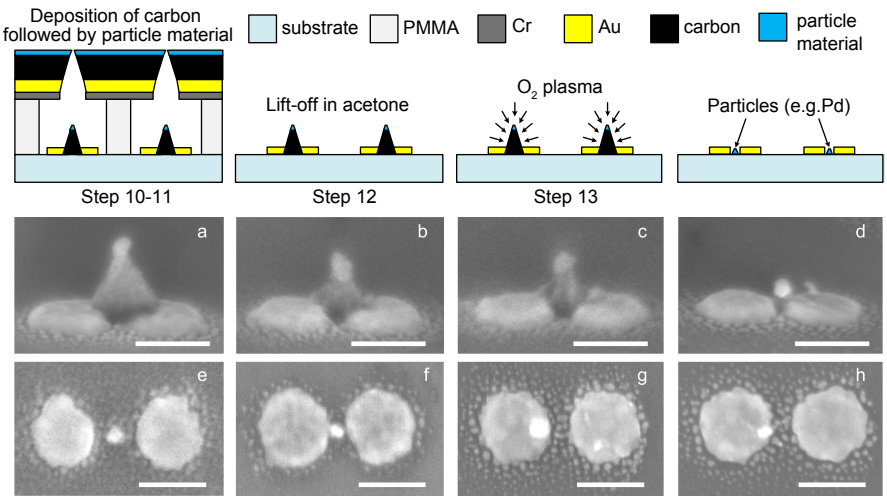


***Figure 4.2.*** *Schematic illustration of the first SHCL nanofabrication strategy used here for placing a small Pd particle in the gap of an Au nanodisc dimer by using a C cone as the sacrificial particle transfer structure. (a-d) 70° tilted SEM images of a sample made on a Si wafer substrate after 1, 2, 3 and 4 minutes in oxygen plasma, respectively. Clearly, the homogeneous removal of the sacrificial C structure by the oxygen plasma is seen with the consequent "delivery" of the Pd particle in the antenna gap. (e&f) SEM images of Au nanodisc dimers with different gap sizes and with a Pd particle in the gap. (g&h) SEM images of Au nanodisc dimers with a gap of 30 nm, and with small Pd particles with two different sizes (21 nm and 10 nm) placed at different lateral positions and in the gap. The scale bar in all SEM images is 100 nm.*

This second SHCL approach, which exploits a sacrificial Cr cone, is very efficient and straightforward to implement. However, also in this case there are a number of limitations in the range of materials that can be used for nanoantenna structure and particle material, dictated by the compatibility with Cr-etch. Moreover, concerns may arise about possible contamination of the sample from the wet etch step, e.g. when catalytic/chemical processes on the formed particle are of interest.

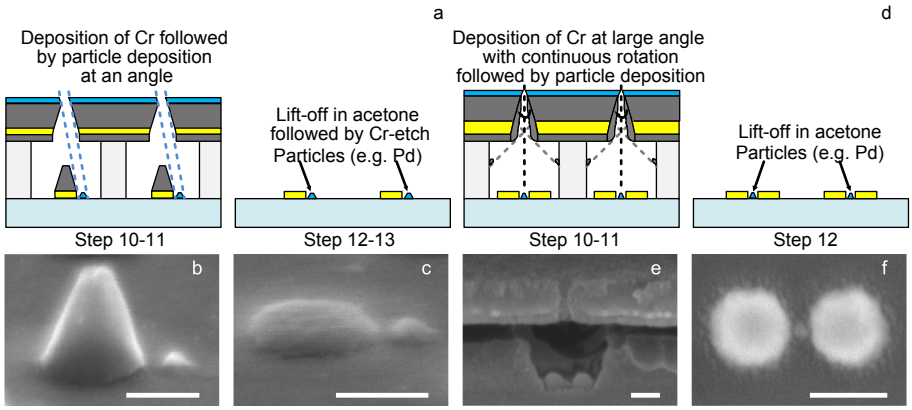


***Figure 4.3.*** *Schematic illustrations of the second (Cr-cone, left) and third (Cr-funnel, right) SHCL nanofabrication strategies used here for placing a Pd nanoparticle next to a Au nanodisc antenna or in the gap/hot spot of a Au dimer, respectively. (a) Sacrificial Cr-cone strategy: Cr is deposited at normal incidence to shrink the hole in the mask and forms a cone on top of the Au antenna. When the desired hole-size has been reached, the second particle (here Pd) is deposited through the mask at a small angle from the normal. After lift-off to remove the mask, the sacrificial Cr cone is removed using a liquid Cr-etch. (b) SEM image of a Cr cone with a Au nanodisc underneath and a small Pd particle next to it. (c) SEM image of a Au nanodisc and smaller Pd particle next to it after the Cr-etch step. (d) Sacrificial Cr-funnel strategy: Cr is deposited at a large angle form the normal with continuous sample rotation to form a funnel while shrinking the hole in the mask. In this way the Cr is deposited only onto the mask and onto the walls of the (underetched) PMMA resist layer in the hole, i.e. no Cr is deposited onto the sample surface. Therefore all the excess material can be removed directly during the final lift-off and no reactive or wet etch is required. (e) SEM image of a sample cross-section before lift-off. The sample features Ag nanodisc dimers with a Pd particle in the gap. (f) Representative SEM image of a Au nanodisc dimer with a Pd particle in the gap fabricated using the Cr funnel approach. The scale bar in all SEM images is 100 nm.*

### Cr funnel approach

As a solution to overcome all the concerns with the previous two approaches, there is a third option that, as the only additional requirement, relies on an e-beam evaporation system, which features sample tilt and rotation simultaneously during deposition. In this way it is possible to eliminate any etching step by again employing Cr to grow a sacrificial structure to tune the diameter of the hole in the mask. Now, however, it is deposited onto the hole-mask at a large angle and with continuous rotation of the sample. In this way, owing to the significant under-etching of the PMMA in the hole-mask, a Cr funnel structure is grown around the nanoantenna in the hole (Fig. 4.3e). The Cr is deposited until the hole in the mask decreases sufficiently for the desired

diameter of the particle to be delivered to the antenna (***step 10***) and then the particle material is deposited through the remaining hole either orthogonally to the surface or at an angle to control the lateral position with respect to the nanoantenna (***step 11***). Given that the angle of Cr evaporation is chosen appropriately (which exact angle to use depends on the size of the initial hole of the hole-mask and on the PMMA thickness), it will be deposited only on the walls of the PMMA layer (i.e. not onto the sample surface itself), such that all the sacrificial material can be removed directly during the lift-off in acetone (***step 12***), and without having to use the Cr-etch at a later step. Hence, any incompatibilities with oxidation-sensitive or non-wet-etch-resistant materials are completely eliminated, as well as the risk for contamination. At the same time the flexibility to build complex polymaterial nanoantenna structures in a completely self-aligned way is retained.

In this way, by exploiting sacrificial materials that are deposited in order to shrink the hole in the mask and then are removed afterwards, it is possible to fabricate complex nanostructures consisting of several nanoparticles of different materials and/or of different sizes. See, for example, a selection of nanostructures that can be fabricated with the SHCL method in Fig. 4.4. In addition, the method is self-aligned in nature and thus allows precise control over the particle sizes and the distances between the particles (i.e. gaps). Since the method is a derivative of the HCL method, it preserves the ability of patterning large areas (few $cm^2$) with aligned complex nanostructures (Fig. 4.5).

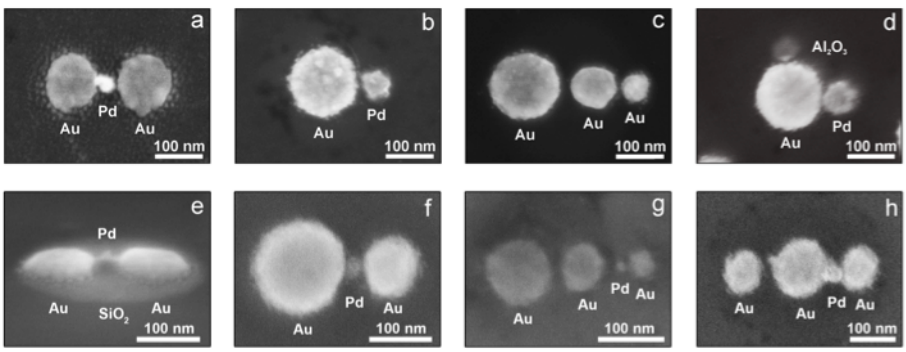


***Figure 4.4***. *A selection of nanostructures that can be made with SHCL: (a) a Au nanodisc dimer with a Pd particle in the gap; (b) a Au nanodisc with a smaller Pd particle on its side; (c) a cascaded Au nanodisc trimer; (d) a Au nanodisc with a smaller Pd and aluminium oxide ($Al_2O_3$) particle on each side; (e) a Au nanodisc dimer covered with a thin silicon oxide ($SiO_2$) layer (deposited by chemical vapour deposition) prior to placement of a small Pd nanoparticle in the dimer gap; (f) an asymmetric Au nanodisc dimer with a small Pd nanoparticle in the gap; (g) a cascaded Au nanodisc trimer with a small Pd nanoparticle in one of the gaps; (h) a symmetric Au nanodisc trimer with a small Pd nanoparticle in one of the gaps.*

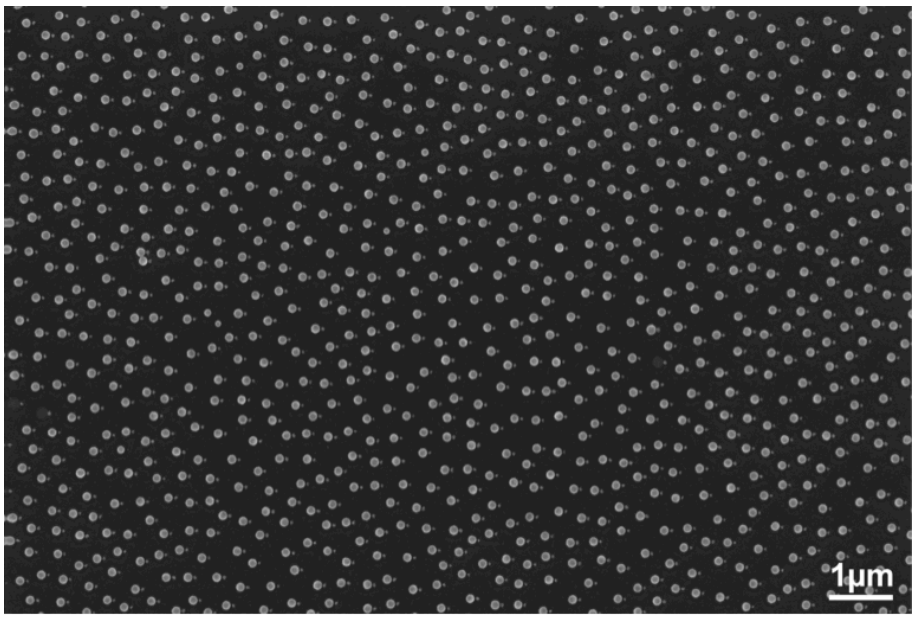


***Figure 4.5.*** *Overview SEM image at low magnification showing the quasi-random arrays of nanoantennas (here Au element with adjacent smaller Pd element) that lack long-range order. Note the excellent yield of small Pd elements.*

#### 4.3.1.3 Fabrication of core-shell nanostructures with HCL

HCL was developed further in this thesis to enable the nanofabrication of arrays of core-shell nanostructures on surfaces with a high level of flexibility in terms of possible material combinations, which is challenging for other methods such as colloidal synthesis. Typically, the targeted nanostructures consist of a metal core and an external shell layer(s) that are of different chemical composition(s). The main motivation for me to create such systems is the possibility to combine distinct properties of different materials in one nanostructure, as a first step towards hybrid systems that achieve new functionalities by concerting the different materials in a constructive way. This concept can be of high importance in a variety of applications such as catalysis, optics or electronics. Full details of the fabrication method are covered in **Paper VI**. In brief, two strategies for fabrication of surface-associated arrays of core-shell nanostructures were developed using a soft (a) and hard (b) sacrificial layer. Specifically, a soft layer is comprised of PMMA polymer, and a hard layer is a Cr thin film. The two routes are similar, and the only difference is that in case of the soft layer, it is deposited first onto the cleaned substrate and then the patterning with PS particles starts. In the hard sacrificial layer route, the deposition of PS is instead done directly on the substrate and only thereafter the sacrificial Cr layer is deposited.

The following is a description of each fabrication step for both versions of the developed nanofabrication (Fig. 4.6 and 4.7):

**Step 1**: Substrates are cleaned with step-by-step sonication in acetone, IPA and methanol. **Step 2 (a)**: PMMA is deposited by spin-coating. The thickness should be lower than in usual HCL, i.e. less than 100 nm (depending on PS size), in order to facilitate shell layer deposition at later steps (for easier penetration of reactants in the holes during ALD or PECVD). Thereafter the PMMA is soft-baked on a hotplate and shortly etched in $O_2$ plasma in order to reduce the hydrophobicity of the surface. **Step 2 (b)** or **Step 3 (a)**: Water-suspended positively charged polyelectrolyte (PDDA) is dispersed on the surface, to form a very thin positively charged layer on the sample surface. **Step 3 (b**) or **Step 4 (a)**: A colloidal suspension of negatively charged PS particles is deposited on the surface. Here, the chosen size of the PS particles dictates the diameter of the holes in the hole-mask and, consequently, the final fabricated structures. Electrostatic repulsion between the PS particles and attraction between PS and the PDDA-treated surface, respectively, creates an amorphous (no long-range order) PS nanoparticle array. **Step 4 (b)**: A thin film of Cr is evaporated on top of PS-covered surface. **Step 5**: A thin film of a material, which is compatible with $O_2$ plasma etching and lift-off in acetone and/or Cr wet-etch (e.g. Au, but can be Cr for route a), is evaporated to form the mask layer (10 - 20 nm thick). Note, that the combined thickness of sacrificial Cr/PMMA layer and Au mask has to be 20 – 30 % smaller than diameter of the PS, in order to ensure the successful tape stripping of the PS beads. **Step 6**: After mask deposition, the PS particles are "stripped" away with tape, which leaves nanoholes in the wet-etch/oxygen-plasma-resistant film layer ("hole-mask"). Note that in case of the hard sacrificial layer, after tape stripping, the size of the holes becomes larger than initial PS size typically by 10 – 30 % due to Cr/Au material closest to the edges of the holes being stripped away together with PS. It is possible to avoid the enlargement of the holes by depositing sacrificial Cr layer and Au mask by rotational evaporation at an angle from the surface normal (instead of surface normal deposition), since in this case material is deposited under the PS beads. This results in holes in the mask, which are smaller than the PS sphere diameters. **Step 7 (a)**: In case of the soft PMMA layer a reactive oxygen plasma etching is applied to selectively remove the exposed PMMA below the holes. The etching creates a partial undercut in the PMMA. **Step 7 (b)**: After tape stripping the hole pattern already extends down to the substrate surface in case of the hard sacrificial layer, however it is necessary to create an undercut in the Cr layer for subsequent shell-layer deposition in order to ensure that the shell covers the metal core from all the sides. Therefore, the sample is immersed in Cr wet-etch solution diluted with deionized water for a short time (from 30 s up to several minutes). The depth of the undercut varies with applied etch time and also depends on the size of the PS particles used. Also note, that one of the reasons why the PS beads have to be deposited directly on the substrate surface as opposed to deposition on top of sacrificial Cr layer similar to standard HCL processing with PMMA, is the isotropic etching profile with Cr-wet-etch solution. In contrast to directional etching with $O_2$ plasma of PMMA, the use of wet-etch solution for undercut of hole-mask on top of sacrificial Cr layer will result in collapsing of the

mask due to isotropic etching. **Step 8**: Nanodisks are obtained by evaporation of the material through the hole-mask. Note that the thickness of Cr/PMMA layer limits the thickness of the targeted disk, which can be subsequently covered by a shell layer. **Step 9 (a)**: A dielectric layer is deposited through the hole-mask by a method, which is compatible with PMMA (i.e. doesn't involve high T or harsh oxidizing plasma conditions). For example, plasma enhanced CVD at room temperature. **Step 9 (b)**: Alumina is deposited through the hole-mask by plasma ALD. In this particular ALD system that we used, the successful ALD deposition of alumina through the hole-mask was possible with thin enough combined thickness of Cr layer and Au mask (i.e. 30 + 15 up to 40 + 20 nm), as well as big enough hole size (i.e. PS 60 nm up to PS 140 nm). Potentially one can improve the results by increasing cycle time of ALD, which might help the precursors to penetrate smaller holes in the mask more efficiently. **Step 10**: In case of the soft sacrificial layer, any material that tolerates lift-off in acetone can be deposited through the hole-mask. In case of the hard Cr layer, it is important to consider materials that are resistant to Cr-wet-etch. Here, a very thin layer (0.5 – 2 nm) of Pt/Pd is deposited through the hole-mask, which forms a granular film that can be subsequently transformed into single crystal clusters with average diameter from 3 to 12 nm by high temperature annealing. **Step 11 (a)**: PMMA layer with excess material on top is removed by lift-off in acetone. **Step 11 (b)**: The hard Cr mask and the excess material on top of it are removed by immersing the sample in concentrated Cr wet-etch solution, which can be heated to 50 °C on the hotplate to speed up the lift-off. Note that the Cr wet-etch will also slowly etch the ALD alumina layer with approximate rate of 1 nm/hour at room T and ~ 8.5 nm/ hour in 50 °C heated solution; therefore it is not advisable to leave the sample in the wet-etch for a long time.

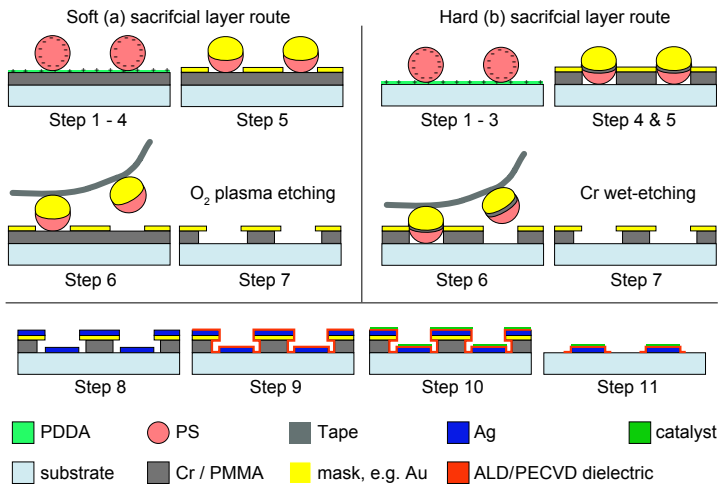


***Figure 4.6**. Fabrication scheme for arrays of core-shell nanostructures based on a soft (left) and hard (right) sacrificial layer route. Details for each step are described in the text.*

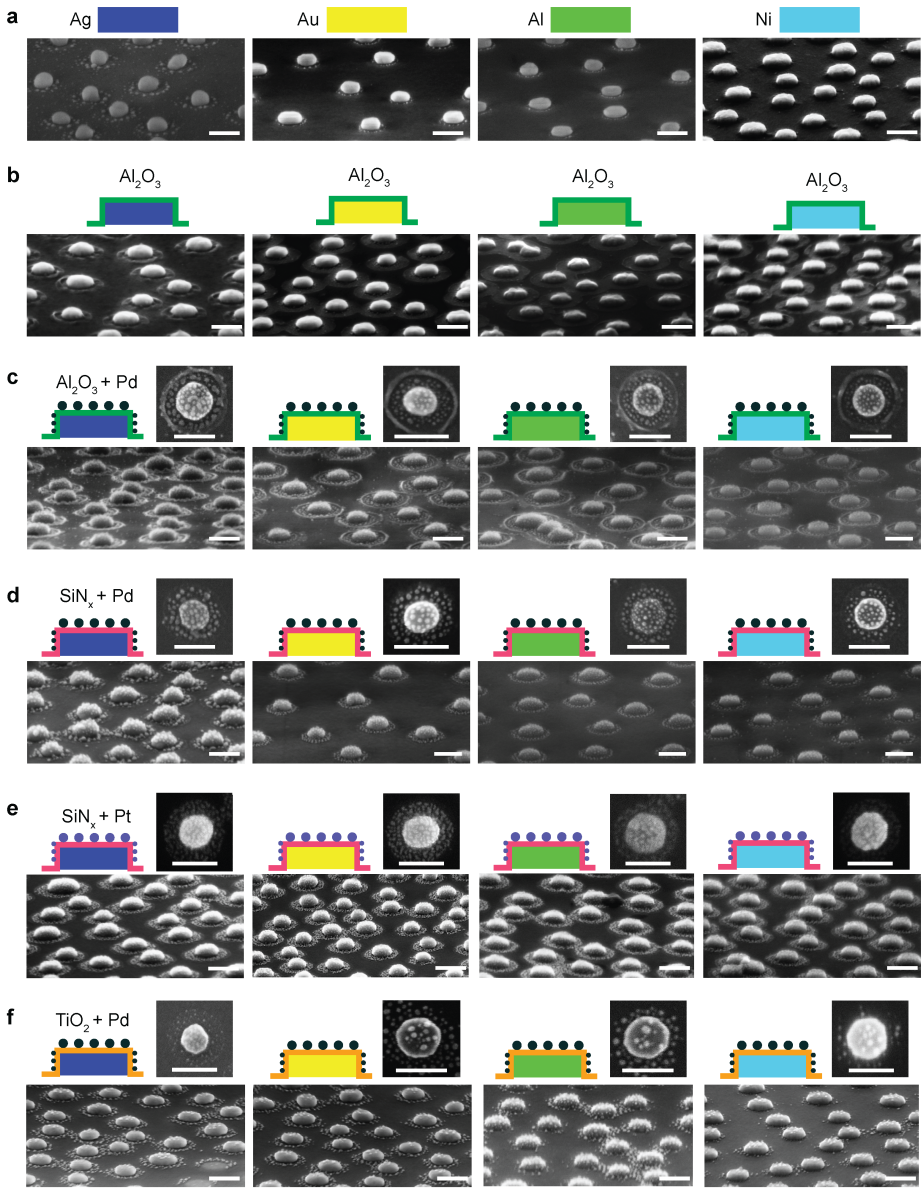
a
Ag
Au
Al
Ni
b
$Al_2O_3$
$Al_2O_3$
$Al_2O_3$
$Al_2O_3$
c
$Al_2O_3$ + Pd
d
$SiN_x$ + Pd
e
$SiN_x$ + Pt
f
$TiO_2$ + Pd

***Figure 4.7****. Schematics of different stages of the core-shell particle array nanofabrication with corresponding top-view SEM images: (a) nanodisk metal cores comprised of Ag (blue), Au (yellow), Al (green) and Ni (light blue) (however, can be any other material that can be deposited by evaporation); (b) a metal core is encapsulated by a thin dielectric layer, here for example, alumina (dark green) grown by ALD. Final result with small Pd nanoparticles (black) on top of core-shell nanostructures with (c) alumina (dark green), (d) silicon nitride (magenta) and (f) titania (orange) constituting dielectric shell layer. In (e) we show that it is possible to deposit any other material that can be deposited by evaporation on top of the core-shell nanostructure, here Pt (light purple). Insets in the right upper corner of c-f show top-view SEM images of corresponding sample with small Pd or Pt nanoparticles clearly visible on top and around single core-shell nanostructures. Note that each sample was annealed before SEM at 320 °C for 6 h in 4 % $H_2$ in Ar. Scale bar in all SEM images is 100 nm.*

## 4.4 Wet-chemical synthesis of metal nanoparticles

This section concerns fabrication methods that are completely different from the ones discussed previously in this chapter. It is about the growth of solid metal nanoparticles via chemical reactions in a liquid reaction medium. The two approaches, i.e. “top down” and “bottom up”, discussed in the beginning of the chapter, are also applicable to the wet-chemical synthesis of colloidal metal particles. The first one involves breaking down bulk metals to obtain metal particles, which have to be stabilized with protecting agents in order to preserve the obtained particle shape and avoid aggregates. The method is versatile for fabrication of a wide range of metal colloids; however, it requires complicated machinery that is difficult to adjust so that narrow particle size distributions can be achieved. The second, “bottom up” approach, which is more widely used, involves the following methods:

1) *Chemical reduction of metal salts*, which is done at the embryonic stage of the nucleation to obtain metal atoms of zero valences that can collide in solution with further metal ions/atoms/clusters and form irreversible “seeds” of stable metal nuclei.

2) *Electrochemical synthesis* of metal nanoparticles comprises several steps, which involve oxidative dissolution of a sacrificial bulk metal anode to metal ions that reductively form zero-valent metal atoms at the cathode, and then proceed to further form metal particles via nucleation and growth.

3) *Controlled decomposition of metastable organometallic compounds* is associated with transition metals. Both organometallic complexes and, in some cases, organic derivatives of the transition metals can be decomposed into short-lived nucleation particles of zero-valent metals with the help of heat, light or ultrasound. The nucleation particles are then stabilized using colloidal protective agents.

4) *Preparation in micelles, reverse micelles and encapsulation*, is related to the use of colloidal self-assemblies (e.g. micelles, water-in-oil reverse micelles, vesicles), which serve as amphiphilic "microreactors" to trap metal ions that upon introduction of reducing agents can form metal particles.

Similar to the "top down" case, a variety of stabilizing agents, e.g. donor ligands, polymers and surfactants, has to be applied to the "bottom up" produced nanoparticles, in order to control their growth and to prevent agglomeration. There are two different modes of particle stabilization, i.e. *electrostatic* and *steric*. Electrostatic stabilization employs Coulomb repulsion between particles, which is caused by electric double layer formation of species (e.g. carboxylates, polyoxoanions) adsorbed at the particle surface and the corresponding counter ions. Steric stabilization is usually achieved by the use of macromolecules (e.g. polymers, oligomers) that adsorb on the particle surface and thus provide a protective shield. There is also a third mode of stabilization, which is the combination of the above two modes and is called *electrosteric* stabilization. It is achieved by the use of ionic surfactants that are characterized by a polar head group capable of creating an electric double layer, and a lypophilic chain that provides steric repulsion.

Wet-chemical synthesis is a powerful toolbox to obtain nanoparticles in a wide range of material, shape and size (down to 1 - 100 nm) in both water (hydrosols) and organic solvents (organosols). Prepared nanoparticles can easily be dispersed on supports characterization and applications. The main concern with wet-chemically synthesized nanoparticles is that experiments have to be carefully designed and take into account the presence of surfactant molecules covering the particle. The surfactant might hinder the activity and cause unwanted response of the particle by "blocking" the surface. Thus, it is important to establish proper cleaning procedures to remove surfactants, while preserving the particle properties, e.g. shape, size and composition. [195,196]

The Au-Pd heterodimers investigated in this thesis were made using a new electrostatic self-assembly process developed by our collaborators in the Moth-Poulsen group at Chalmers (**Paper II**). While plasmonic Au spheres were purchased from Sigma Aldrich and used as received, the Pd particles of different sizes and shapes were synthesized by adapting procedures described in the literature[177,197,198]. Briefly, the method for Pd particle synthesis comprised a chemical reduction of the metal salt (hydrogenchloropalladate ($H_2PdCl_4$)) with ascorbic acid in aqueous solution of a surfactant material (cetyltrimethylammonium bromide (CTAB) or chloride (CTAC)). The Pd seeds obtained this way were further used to make cubes of larger sizes (or other shapes) by means of seed-mediated growth. Fig. 4.8 represents a selection of various heterodimer structures that can be obtained with this approach.

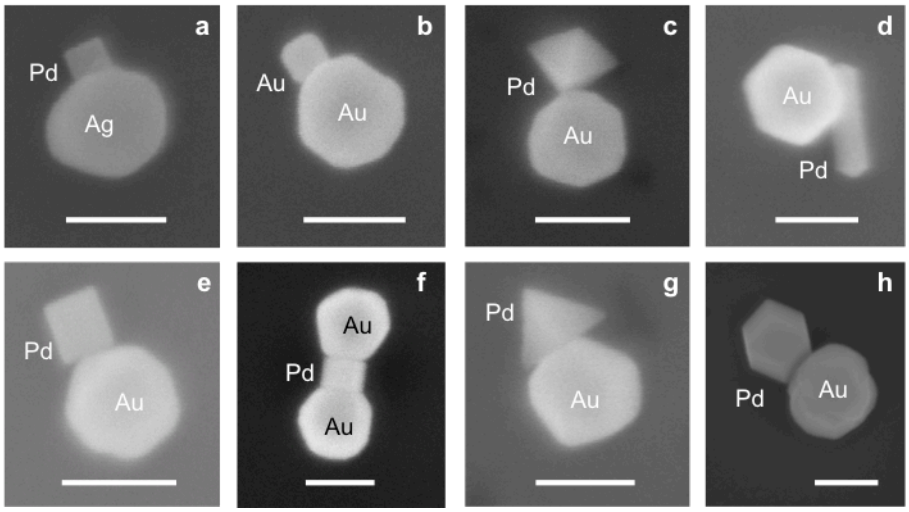


***Figure 4.8.*** *A selection of the heterodimer structures that can be made via wet-chemical synthesis and electrostatic self-assembly (**Paper II**): (a) a Ag sphere with a Pd cube; (b) a Au sphere with a Au cube; (c) a Au sphere with a Pd octahedron; (d) a Au sphere with a Pd rod; (e) a Au sphere with a Pd cube; (f) two Au spheres with a Pd cube in-between; (g) a Au sphere with a Pd tetrahedron; (h) a Au sphere with a Pd dodecahedron. The scale bar in all SEM images is 100 nm.*

# 5 FABRICATION TOOLS

As discussed in the previous chapter, the nanostructures were produced by implementing a new SHCL method and further development of the generic HCL platform. These methods involve various processing techniques, and this chapter gives an overview of the tools and processes that were used.

## 5.1 Spin coating

Spin coating makes it possible to achieve uniform films, with well-controlled thickness, of a material that can be dissolved in a solvent (e.g. polymers) on the surface of the substrate. In spin coating, typically, few droplets of a fluid (usually a solution of polymer in a solvent or a colloidal suspension) are deposited on the centre of the substrate that is subsequently subjected to a high-speed rotation. The rotations make the fluid spread by centrifugal force to the edges of the substrate, and eventually a uniform thin film is formed on the surface. Film thickness and quality of the coated film depend on the fluid properties (composition, viscosity, wetting, solvent evaporation rate), properties of the substrate (surface roughness, wetting) and conditions of the spinning process (spin speed, acceleration time, exhaust conditions).

The next step after dispensing is rotational acceleration leading into the typical final speed range of 1000 - 6000 rpm. The exact speed should be chosen considering the properties of both fluid and substrate. Other factors that affect evaporation rate and consequently, film thickness, are turbulence and ambient humidity. Spinning is usually performed in a closed spinner bowl environment to reduce the effect of airflow around the spinning substrate and also to maintain full exhaust during the spinning. After spinning, the substrate is usually baked at temperatures in the range of 100 to 250°C to remove the solvent and to leave only the film of the resin material on the surface.[199]

## 5.2 Plasma etching

Plasma can be considered as a fourth state of matter along with solid, liquid and gas, although its properties are similar to the gas state. Plasma consists of atoms, molecules, radicals, ions, neutrals and free electrons. It is locally polarized but the number densities of positive and negative charges are equal on average. In micro- and nanofabrication plasma is widely used for deposition and etching processes.

In this thesis, all plasma processes were performed in the commercially available system Plasma Therm BatchTop PE/RIE m/95. It is a reactive ion etching (RIE) system that operates at radio frequency (RF 13.56 MHz) and has a maximum power of 500 W and pressure up to 500 mTorr. The main chamber is pumped by a turbo pump and a mechanical roughing pump. Inside the chamber there is a bottom electrode (cathode) where samples are placed. The cathode is capacitively coupled to a radio frequency (RF) generator and is water-cooled. The top electrode (anode) and the chamber walls are grounded. The plasma is generated by applying glow discharge between two electrodes to the gases that are supplied through the gas inlets. The process gases include $O_2$, $CF_4$, Ar and $H_2$. A strong electromagnetic field causes the gas molecules to be stripped of electrons and become ionized, and thus, plasma is created. After plasma ignition, due to the fact that electron mobility is much higher than the mobility of ions, the cathode acquires negative charge and the sample placed on top of the cathode is exposed to positive ion bombardment. At the same time there are also plasma-generated reactive species that diffuse and adsorb on the surface of the sample, where they form highly volatile compounds. The volatile reaction products are desorbed into the gas phase. This process is greatly accelerated by ion bombardment via sputtering. The volatile reaction products are then pumped out from the system. Thus, the etching in the plasma system occurs simultaneously via two mechanisms: physical – by ion bombardment, and chemical – through the chemical reaction between sample material and reactive species of the plasma.[194,200,201]

In this thesis, $O_2$ plasma etching was used in order to remove the sacrificial polymer layer utilized for sample fabrication with HCL, as well as for removal of sacrificial C cone structures in SHCL. As mentioned earlier, the etching can be quite a harsh process that can change properties of materials exposed to it. Care should therefore be taken in the duration of etching with $O_2$ plasma since it may oxidize the particles such as Pd or Pt, which is not desirable if the oxide cannot be removed without harming the entire structure. For example, as can be seen from SEM images taken from the synthesized Pd cube before and after $O_2$ plasma cleaning (Fig. 5.1), long exposure times can affect the surface of the particle. In this case, the appropriate cleaning procedure to remove/reduce the oxide could be for example flushing the sample with $H_2$ gas at slightly elevated temperature.

$H_2$ plasma etching, due to its reducing rather than oxidizing nature, was utilized for cleaning the wet-chemically synthesized particles from surfactant material covering the particles used in this work. We also found that it was more efficient in this respect, compared to oxygen plasma.

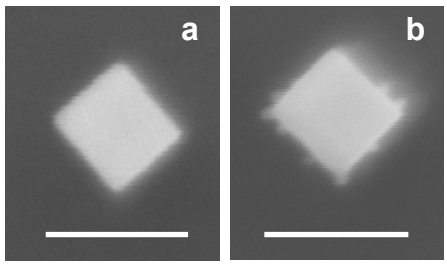


***Figure 5.1.*** *SEM images of a synthesized Pd cube (a) before and (b) after 7 min of $O_2$ plasma treatment. The small features that appear after plasma treatment around the Pd cube are presumably indicators of oxidation. The scale bar in SEM images is 100 nm.*

## 5.3 Vacuum deposition of materials

Vacuum deposition is a physical vapour deposition (PVD) process. The source material is heated thermally, which causes atoms or molecules from the source to travel directly to the substrate where they form a thin film of vaporized material by re-condensing on its surface. The vacuum conditions allow the particles to reach the target sample without (or very few) collisions with residual gas molecules in the deposition chamber. Such a process requires a good vacuum in order to obtain a long mean free path between collisions; although, at such pressure there is still a lot of residual gases that can contaminate the film by impinging on the substrate during deposition. In order to get films with high purity it is important to use high ($10^{-7}$ Torr) or ultrahigh (< $10^{-9}$ Torr) vacuum.

The thermal vaporization source is one of the simplest sources to produce vapours of materials. As the name suggests, it is a source where thermal energy is used to produce the vapour of the deposited material. There are several common heating techniques for such evaporation, which include resistive heating, high-energy electron beams, low energy electron beams, and inductive heating. In this thesis, resistive heating and e-beams were used and these techniques will be described below.

### 5.3.1 Resistively heated sources

Materials that vaporize at temperatures below 1500 °C can be heated to sufficiently high temperatures by passing high electric current through a filament container (with source material), which has finite electrical resistance. There are several requirements on such an evaporation source. First of all, the source simply has to be able to contain the source material and prevent it from falling from the heated surface. The reason is that many materials become liquid at the temperatures that are required to get reasonable deposition rate. The source has for such purpose, typically a form of a container (crucibles, boats, baskets, wires, etc.) and can also have a wetting surface,

which allows good thermal contact between the hot surface and the material being vaporized. There are also other materials that instead of evaporating get sublimated (e.g. Cr, C, Mg, Pd, cadmium (Cd), arsenic (As)), which means that they do not melt or flow, and for such materials a rod type source can be used or the evaporant material can be in powder or tablet form, which in turn is placed in suitable container. Another requirement for the source is that it has to provide thermal energy to the evaporant at high temperatures without extensively vaporizing itself. Finally, the most important requirement is that the source has to be compatible with the evaporant, which means that no extensive chemical reaction or alloying between the source and the evaporant material is acceptable. Most common materials that are used as resistively heated sources are tungsten (W), tantalum (Ta), molybdenum (Mo) or C, which are known to have the highest melting points and lowest vapour pressures among elements. High current connections to the source are usually made of materials that have high electrical conductivity (e.g. Cu).[202,203]

In the early stages of this thesis work, a commercially available Edwards 306 Evaporator was used for thermal evaporation of the hole-mask and Au nanodimers. The fully automatic turbo-molecular pumping system of the Edwards gives a base pressure of less than $5\times10^{-7}$ mbar. The evaporator is equipped with a 4-position resistive evaporation source and has a tilt stage, which allows high precision angle evaporation. The sample is placed upside down on tiltable stage facing the evaporant source, which is heated. An almost uniform film of material is evaporated all over the chamber including the sample position.

### 5.3.2 Electron beam heated sources

Electron beam evaporation involves intense high-energy e-beams and it allows for a wide variety of materials to be evaporated at high rate and with minimum consumption of energy. As opposed to resistive heating evaporation, e-beam evaporation can also be used for deposition of materials that evaporate at temperatures above 1500 °C such as most ceramics, glasses, carbon and refractory metals, or in cases when a large amount of material is needed to be evaporated.

Electrons are usually generated in a thermionic source or by ionizing gaseous atoms and molecules, which act as a cathode. The evaporation material acts as the anode and it is contained in a crucible that is usually water-cooled. When the e-beam hits the surface of the material electrons start to interact with the atoms of the evaporant. As a result, the kinetic energy of the electrons is converted into various forms of energy, most of which constitutes thermal energy (~ 85 %). The thermal energy produced in this way is used to melt or sublimate the evaporant to achieve a desired vapour pressure. Another advantage of e-beam deposition is that the highest temperature of the evaporation occurs only where the e-beam hits the evaporant surface. Therefore, if the evaporant material can be melted, and a water-cooled copper crucible is used – the melted material forms a “skull” of its own by solidifying itself near the interface of the area that is hit by the e-beam. Thus, the melted material is contained in its own solid

"mould", which helps to avoid reaction of the evaporant with the crucible material.[202,203]

As can be seen in some of the SEM images in **Paper I** as well as in Fig. 5.2, there are small particles visible around some of the Au nanodiscs (e.g., Figures 1a and 3a−h of the **Paper I**). These small particles are Au particles, which are formed most likely due to "splashing" that occurs when evaporated Au atoms/clusters traveling to the sample substrate collide with the edges of the hole-mask, and therefore slightly change their direction and end up off the main target area determined by the hole-mask. It is a characteristic and inevitable feature in the cases when underetching of the mask is present (also, e.g., when EBL double-layer resists are used). However the effect can be reduced to some extent using e-beam evaporation rather than resistive evaporation (Fig. 5.2).

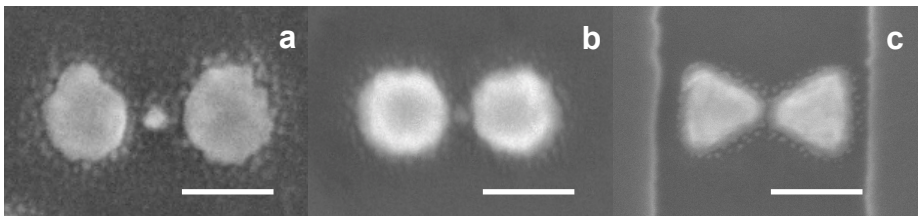


***Figure 5.2.*** *SEM images of the Au nanodisc dimers made (a) with resistive evaporation and (b) e-beam evaporation. As can be seen the latter technique results in smaller amount of Au "splashes" around the nanodiscs. (c) An SEM image of a pair of Au triangles made by EBL (image courtesy of Joachim Fritzsche), where tiny "splashes" of Au are also visible. The scale bar in all SEM images is 100 nm.*

## 5.4 Chemical vapour deposition

Chemical vapour deposition (CVD) processing is widely used in micro- and nanofabrication. CVD is a chemical process to produce thin films, where typically the substrate is exposed to volatile precursors, which react and/or decompose on the substrate surface to form the desired deposit. Chemical reactions occur both in the gas phase and on the substrate surface. There are several types of CVD and in the following I will describe the ones used in this thesis.

### 5.4.1 Plasma-enhanced CVD

Plasma-enhanced CVD (PECVD) is a film-deposition process, where the chemical reactions involved occur after generation of plasma of the reacting gases. PECVD reactors are similar to plasma etchers. Plasma is usually generated by RF field or direct-current (DC) discharge between two electrodes, where the space between them is filled with reacting gases. Processing plasmas are operated at pressures of a few mTorr to a few Torr. Energy generated by the discharge is transferred to the gas mixture, which transforms into reactive radicals, ions, neutral atoms and molecules.

These species react with the substrate and, depending on the nature of their interactions, either etching or deposition occurs on the substrate. With increasing RF power the deposition rate increases, since more reactants are ionized and available for reaction, however further increase can lead to lowering of the rate due to sputtering of the formed film by ion bombardment. The main advantage of PECVD is the low deposition temperature, since formation of the reactive and energetic species occurs in the gas phase, and the substrate can be maintained at low temperature. The usual PECVD operating temperature is around ≤ 300 °C. However, the resulting film properties are strongly temperature dependent. In particular, the hydrogen content is known to increase with lowering of temperature, which makes the films less dense. In PECVD process the deposition takes place everywhere, i.e. not only on the substrate but also on the reactor walls and the electrodes, therefore it is common to perform regular etching to remove these deposited layers from the chamber walls.[199]

A PECVD machine (Plasmalab 100/ICP180) from Oxford Instruments Plasma Technology was used in this thesis for deposition of silicon nitride or oxide. For these processes, silane gas ($SiH_4$) is injected near the substrate in the process chamber. Argon is ionized in the inductively coupled plasma (ICP) chamber. ICP is the type of plasma source, where energy is supplied by electric current produced by electromagnetic induction (i.e. time-varying magnetic fields). No electrode RF-power is used in this deposition process, as kinetic ions would induce high compressive stress in the deposited films. The exited molecules from the ICP dissociate the $SiH_4$ and enhance chemical reactions on the surface of the substrate. If molecular nitrogen ($N_2$) is added to the Ar in the ICP, silicon nitride is deposited on the substrate and on the process chamber walls. The silicon nitride will likely not have a precise stoichiometry, therefore, the film is usually denoted $SiN_x$. If nitrous oxide ($N_2O$) is added to the Ar in the ICP, silicon dioxide ($SiO_2$) is deposited.

### 5.4.2 Atomic layer deposition

Atomic layer deposition (ALD) is the CVD method that allows precise atomic layer-by-layer growth of conformal films on the substrate. In the ALD process, typically two precursors are introduced to the substrate one at a time, where they reach monolayer saturation on the surface. All excess precursor molecules and volatile reaction by-products are removed from reaction chamber by the inert gas purge accompanying each cycle. Precursors are never present simultaneously and react with the surface in a self-limiting way, so that reaction terminates when all the surface sites are occupied.

Practical deposition rates are around 1 Å/cycle, and cycle length can be different from material to material. One cycle includes the time a surface is exposed to each precursor (dose), as well as the flushing time for each precursor to evacuate the chamber (purge), which gives a dose-purge-dose-purge sequence for binary ALD processes. Overall rates are typically few nanometers per minute, which means that ALD is a very slow method compared to PVD methods such as evaporation or sputtering. However, there are many applications where very thin layers are needed and the quality of the films

cannot be compromised. ALD allows producing very uniform thin films of wide variety of materials with control of thickness down to atomic level. [199,204]

In this work an Oxford FlexAl ALD system was used for deposition of $Al_2O_3$ at substrate temperature ranging between 100 °C to 400 °C. The tool operates in two modes: thermal ALD and plasma ALD. Precursors for $Al_2O_3$ are trimethylaluminum (TMA) and correspondingly $H_2O$ for thermal and $O_2$ plasma for plasma-assisted processes.

# 6 CHARACTERIZATION TECHNIQUES

## 6.1 Scanning Electron Microscopy

Scanning electron microscopy (SEM) is a versatile technique that allows for imaging of organic and inorganic materials with a resolution in the μm to nm range. The examined area is irradiated by a focused electron beam, which can be swept across the sample surface in a raster pattern. Several types of signals are generated when the electron beam interacts with the sample: secondary electrons, backscattered electrons, characteristic X-rays, transmitted electrons and specimen currents. The most common operating modes of SEM use the signal from secondary and backscattered electrons to form a high-resolution image of the examined sample area.[205]

Backscattered electrons are high-energy electrons that come from the beam and that get reflected from the sample by elastic scattering. They give information about the chemical composition of the sample as the intensity of the signal is strongly correlated with the atomic number Z. Heavier atoms backscatter electrons more strongly than light atoms and, thus, appear brighter in the image. Secondary electrons are ejected from the outer shells of the sample atoms by inelastic scattering when interacting with the e-beam. They have much lower energy than backscattered electrons and come from within few nanometers of the sample surface and, thus, give good topographic information. The three-dimensional-like image of the sample is obtained due to the large depth of field of SEM (i.e. how much of the object under observation remains in focus at the same time) and the good contrast between backscattered and secondary electrons.

For conventional SEM imaging, there are several requirements. Besides being of reasonable size to fit in the SEM chamber, samples should be conductive, at least at the surface, in order to prevent charge accumulation. Another requirement is vacuum condition during imaging to prevent spreading and attenuation of the e-beam. The latter requirement complicates the investigation of samples that vaporize. However, in cases when samples are non-conducting or vaporize, they can be covered with a very thin layer of conducting material such as Au, Pt, Cr or C. Another way to solve these issues is to use environmental SEM (ESEM) or SEM at low voltages, where no coating is required. In ESEM, the sample is placed in relatively high-pressure environment rather than in high vacuum. During such conditions, the e-beam starts interacting with gas species. This results in positively charged ions, which neutralize negative charges on the sample surface. For SEM at low voltages, typically field-

emission gun (FEG) SEM machines are used, as they allow reasonable brightness and contrast at low accelerating voltages. [205]

In this thesis, all samples for single particle spectroscopy were fabricated on pieces of a thermally oxidized Si wafer with the thickness of the oxide being 50 nm. The presence of the thin oxide layer was crucial in order to perform dark field scattering spectroscopy as explained in the Section 6.2.1. The oxide layer on the substrate was the cause of SEM images having slightly lower resolution, compared to the case if nanostructures would have been fabricated on plain Si. $SiO_2$ is a non-conducting medium and it results in some charge build-up on the sample surface. However, since it is quite thin, the effect is not as severe as it would be if samples were fabricated on glass substrate (Fig. 6.1). Nevertheless, the image quality was sufficient to identify suitable nanostructures, and make approximate estimates of nanostructure dimensions.

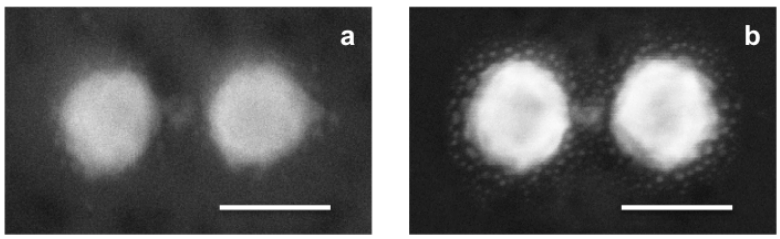


***Figure 6.1.*** *SEM images of two Au dimer nanostructures with a small Pd particle in the gap made under identical conditions (i.e. in parallel) with the only difference being the used substrate: a) thermally oxidized silicon ($SiO_2$ ~ 50 nm); b) regular silicon wafer. The nanostructure on silicon is seen with much more detail and with better resolution, as opposed to the one made on the oxidized silicon substrate, where the thin non-conducting layer of oxide causes slight charge build-up and, thus, worsens the image resolution. The scale bar in both SEM images is 100 nm.*

### 6.1.1 Identification of SEM-imaged nanostructures in the optical microscope

SEM was a key tool in this thesis in order to find and characterize individual nanoantenna structures, which were further used in the single particle plasmonic sensing experiments, thus allowing correlation of measured signals from the nanoantenna structure and nanoparticle of interest with their appearance in SEM. To find identified nanostructures in the optical microscope, where the plasmonic sensing experiments were performed, after SEM imaging I developed the following procedure. First, with the aid of a scribing pen, the sample was marked with one or two scratches that were clearly visible in the optical microscope. Then SEM imaging was done nearby one of the scratches, however not very close (at about 200 - 300 μm distance), since a scratch on the sample surface produces a lot of stray light in the optical microscope, which would interfere with the plasmonic nanoparticle scattering signal

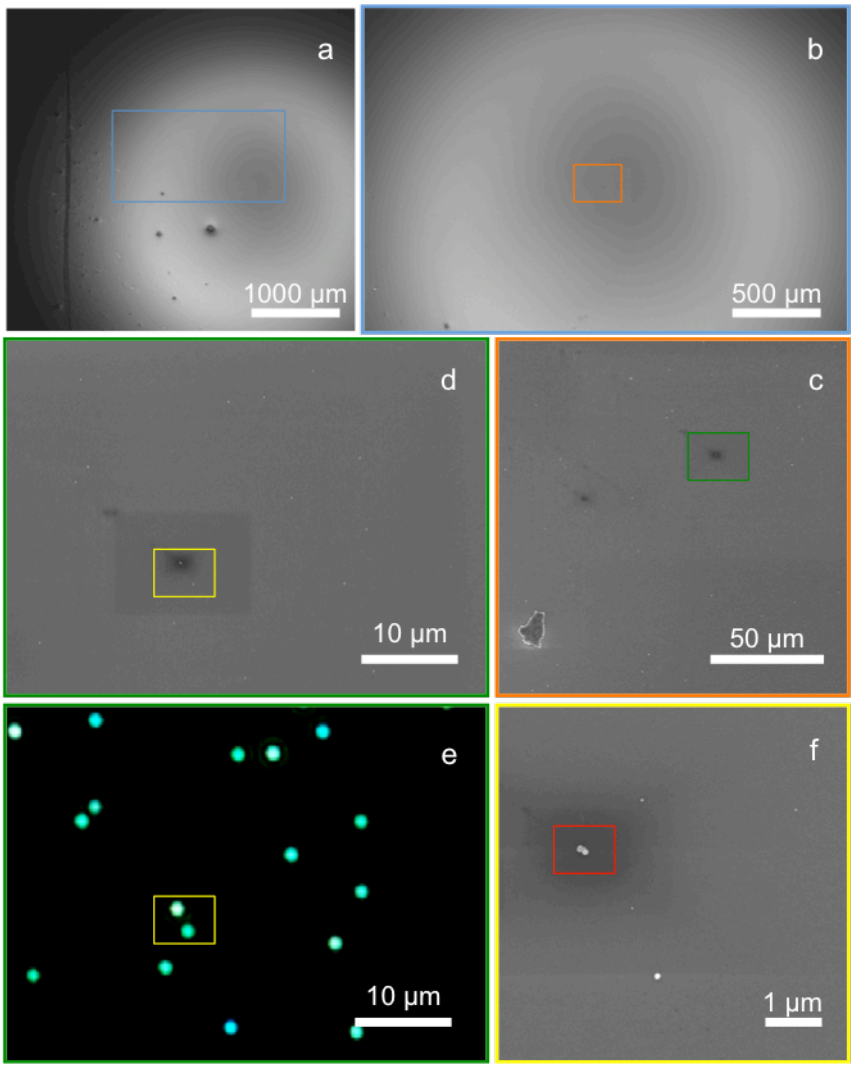


***Figure 6.2.*** *The "map" for finding a particle in the optical microscope after SEM imaging: a) SEM image at low magnification (145×) of the sample area near the scratch (dark vertical line to the left); b) zoomed in view (235×) on an area marked with a blue square in (a); c) zoomed in view (2000×) on an area marked with an orange square in (b); d) zoomed in view (6000×) on an area marked with a green square in (c); e) optical microscope view of an area depicted in the SEM image in (d); f) zoomed in view (26000×) on an area marked with a yellow square in (d) and (e). Zoomed in view on the particle in a red square (f) can be found in Fig. 6.3.*

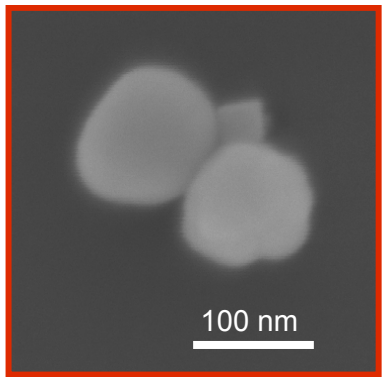


***Figure 6.3.*** *SEM image of two Ag spheres with Pd cube in between, that can be found with the "map" constructed in Fig. 6.2 and is located in the red square of the panel f.*

if the particle was too close to it. When a suitable nanostructure was found, it was imaged at high magnification in order to be able to clearly see the structural details and estimate the size of the particle. After this the nanostructure was imaged at several decreasingly lower magnifications in order to create a "map" of the sample topography that would step by step allow finding the particle of interest "from scratch" in the optical microscope. Such a "map" is shown in Fig. 6.2 for a sample with spin-casted wet-chemically synthesized heterodimers of Ag–Pd, where the map was made to find the particle depicted in Fig. 6.3. Each part of the "map" in Fig. 6.2a-d has some kind of feature that makes it possible to navigate on the sample surface in the optical microscope. For example, there is a big scratch mark in the left part of Fig. 6.2a, few dirt pieces in the left lower corner of Fig. 6.2b (which are probably small splinters from the substrate after making a scratch mark), an even smaller piece of dirt in Fig. 6.2c, and then the ensemble of nanoparticles that create a unique pattern in Fig. 6.2d, and that can be visible as a corresponding pattern of bright spots in the optical microscope with dark-field illumination in Fig. 6.2e.

## 6.2 Transmission Kikuchi Diffraction

Transmission Kikuchi diffraction (TKD) is a rather new method for characterization of crystallographic properties of nanomaterials (Fig. 6.4). It is performed in an SEM instrument and is based on the electron backscatter diffraction (EBSD), which is a technique that provides information about microstructural parameters of crystalline and polycrystalline materials such as crystal orientation, defects, texture, grain morphology and deformation. In EBSD, a tilted bulk crystalline sample is irradiated with the beam of electrons, which undergo various interactions with the atoms in the crystal lattice. Since the specimen is thick enough a large number of scattered electrons is generated that travel in all directions. Some of the electrons are backscattered, and some of the emerging electrons may exit at the Bragg condition

from the crystal planes and form so-called Kikuchi patterns or bands. The Kikuchi bands correspond to each of the diffracting crystal planes in the lattice. A fluorescent phosphor screen can capture the patterns, if it is placed close to the sample, so that electrons collide and excite the phosphor that starts to fluoresce. In this way, crystal orientation maps can be formed that show all the grains and their orientation and position in the sample, as well as grain boundaries. [206]

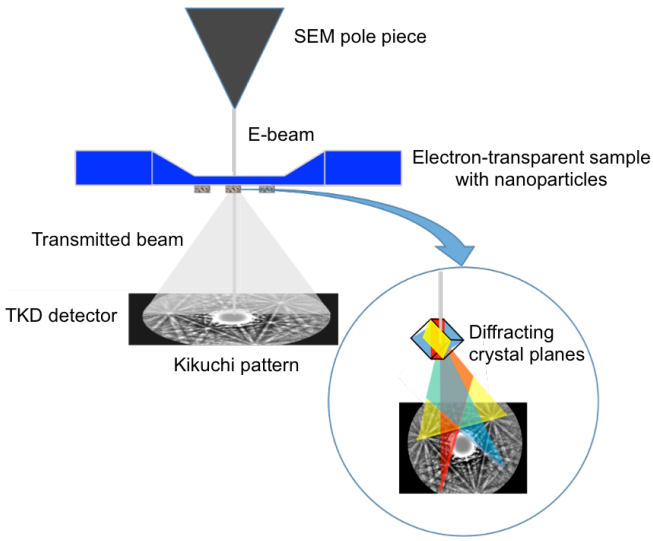


***Figure 6.4.*** *Schematic drawing of TKD setup, where nanoparticles on the TEM window are facing away from the SEM pole piece. The electron beam is scanned over the sample and for each scanned point the diffraction patterns are captured by the detector located underneath the sample. Each line on the pattern represents a crystallographic plane of the crystal and the characteristic Kikuchi pattern gives the full orientation of the crystal at the electron beam exit surface.*

EBSD becomes difficult to use when the sample volume is lowered such as in nanoparticles or small grains in thin films, because the number of backscattered electrons that can be detected significantly decreases. In addition, nanostructures lack a planar surface, which can cause shadowing effects or direct the beam away from the detector. In order to overcome this problem, the TKD method was developed, which is also referred to as transmission EBSD or transmission electron *forward* scatter diffraction (t-EFSD). TKD was introduced in 2012 by Keller and Geiss[207]. The technique uses standard EBSD equipment but requires electron transparent samples with thickness on the order of 50 to 150 nm. The diffraction patterns resemble EBSD patterns, but are formed with transmitted rather than backscattered electrons. This means that, as opposed to conventional EBSD, the thin specimen is placed with the surface normal away from the detector, thereby minimizing backscattering into the

detector, and maximizing detection of electrons that have scattered through large angles in transmission. Existing EBSD software was initially adapted for automated indexing of TKD patterns. However, due to the different and restricted geometry of this new configuration, the pattern centre is often located outside the detector screen, causing geometrical pattern distortion and complicating indexing. Only recently a new configuration was introduced by Fundenberger et al.[208] and commercialized by Bruker Nano GmbH, where the phosphorous screen is located *beneath* the thin specimen on the optical axis of the microscope. In this new configuration, the pattern distortion is removed and the electron intensity is increased, allowing reduction of beam current and, consequently, further improvements in spatial resolution. Compared to conventional diffraction techniques in transmission electron microscopy (TEM) the main advantage of TKD is its full automatization, which allows detailed microstructure characterization over large areas of the specimens at very high speed. In comparison to EBSD, the spatial resolution is improved, due to the smaller interaction volume, and can be 5 nm or better. Furthermore, TKD is not limited to flat specimens and can be applied to investigating nanoparticles and nanowires, among others. In **Paper IV**, TKD was used for characterization of grains in polycrystalline Pd nanoparticles and measurements were carried out by Dr. Alice Bastos da Silva Fanta at Center for Electron Nanoscopy (CEN) at the Technical University of Denmark (DTU).

## 6.3 Transmission electron microscopy

Transmission electron microscopy (TEM) is a very powerful characterization technique in physical, chemical and biological sciences with high spatial and analytical resolution. With TEM it is possible to resolve structure of materials down to the atomic level. In contrast to SEM, the electron beam in TEM is transmitted *through* the sample in order to form an image. For the electrons to be able to pass through, the samples have to be very thin, i.e. electron transparent. This implies, depending on the desired image resolution, density and composition of the material, thicknesses from 100 down to 5 nm. Therefore, in order to make very thin specimens, special sample preparation techniques are required such as electropolishing, chemical or ion-beam etching in materials science and ultramicrotomy or staining in biological sciences. For studying nanoscale materials (films, rods, nanoparticles and clusters) with TEM, it is usually sufficient to deposit them in diluted concentrations on special substrates such as grids, films or membranes, where as a common denominator they have very thin areas in the support material allowing TEM imaging. [209]

Electrons in TEM are supplied from an electron emission source (typically Schottky, (cold) field emission or thermionic source). The electron beam is accelerated (with 80 – 120 kV in standard instruments and up to 500 kV – 3 MV in high-voltage EM) and focused via electromagnetic lenses on the specimen. When electrons pass through the sample they interact with the atoms and generate signals (Fig. 6.5), most of which can be detected in various TEM modes. When the electron beam has passed the sample it results in a non-uniform distribution of electrons that contains all the structural, chemical and other relevant information about the specimen. The result is collected by

a system of magnifying lenses, which focus the image from the modified beam onto an imaging device, usually a fluorescence screen or charged-coupled device (CCD). Both the spatial and angular distribution of electrons is changed when they emerge from the specimen. The first can be observed as contrast in the specimen images, and the latter – in the form of scattering patterns called diffraction patterns.

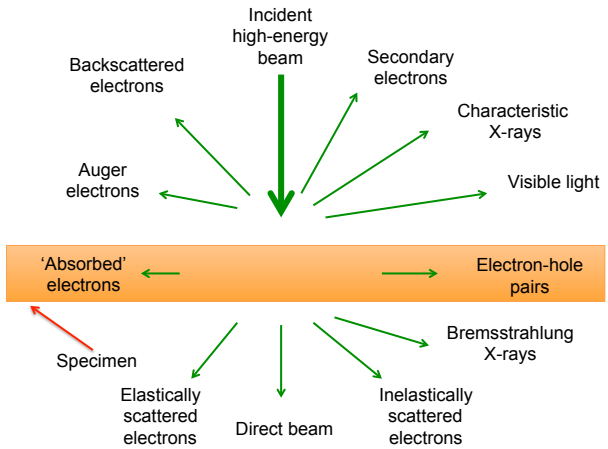


***Figure 6.5.*** *Signals generated in TEM by high-energy beam of electrons upon interaction with specimen. Adapted from Williams & Carter*[209].

By adjusting the configuration and/or strength of the condenser, magnifying and objective lens systems, TEM can be used in different modes, which provide various kinds of information about the specimen. In the bright-field mode, the contrast is formed by transmitted electrons (only the direct beam is let through). Areas of the specimen with higher atomic number or thickness will appear dark, whereas areas with no specimen in the beam path will appear bright, hence the name "bright-field". In the dark-field mode the microscope configuration is such that only some of the diffracted electrons (particular diffraction should be specified) are allowed to pass. The resulting image will have dark regions wherever no sample scattering to the selected peak occurred. Thus, a dark-field image is formed and gives information about planar defects, stacking faults or feature sizes. In the EELS mode, it is possible to analyse the energy distribution of electrons that have passed through the specimen. A magnetic prism is used to deflect the beam the more it looses the energy, thus electrons can be rejected based upon their energy values. The amount of lost energy is measured by an electron spectrometer and can be interpreted in terms of what caused the energy loss (i.e. types of atoms, number of atoms of each type and the scattering angle). In high-resolution TEM (HRTEM) the image constitutes an interference pattern between the forward scattered and diffracted electron waves from the specimen. Thus image formation relies on phase contrast that arises from the change in relative phases of

electrons transmitted through the specimen. This causes diffraction contrast in addition to the contrast in the transmitted beam, which is already present. The interpretation of such phase-contrast images can be very challenging and can rarely be done by a naked eye; instead complex computer simulations are required. However, due to its remarkable sensitivity it is possible to resolve the *atomic* structure of thin specimens.[209]

When the magnetic lenses are adjusted such that the back focal plane of the lens rather than the imaging plane is placed on the imaging device, a diffraction pattern of the specimen can be generated. This mode of operation is called selected area electron diffraction. It gives information about sample's crystallinity. For amorphous samples the atoms are randomly arranged, which leads to the amplitude (and hence the intensity) of diffraction being stronger at some angles than the others, so diffuse rings are seen on TEM screen. For crystalline samples, the intensity of the diffracted beam is highest at specific angles because of very well defined spacing between the lattice planes; therefore one can see patterns of dots. The diffraction pattern of single crystalline samples depends on the orientation of the sample and the structure illuminated by the electron beam.

The limitations of the TEM accompany all of its advantages. This concerns sampling, which gets worse with higher resolution – one can look only at very small parts of the specimen at any moment in time. Another drawback is projection-limitation, which is related to the fact that all kinds of TEM information (images, diffraction patterns or spectra) are averaged through the thickness of the specimen, so there's no depth sensitivity. Another limiting aspect of TEM one has to think about is electron beam damage, which may destroy the specimen or induce changes in it during imaging. The detrimental effect of ionizing radiation can affect not only the specimen, but also, if one is not careful, the operator.

Our collaborators in the Moth-Poulsen group at Chalmers performed TEM characterization of the samples in **Papers II** and **III**, whereas in **Paper IV** TEM analysis was done by Dr. Beniamino Iandolo at CEN in DTU.

## 6.4 Dark-field scattering spectroscopy

Light can be transmitted, absorbed or scattered by a material. Dark-field scattering spectroscopy (DFSS) is used for the detection of scattered light, and it requires dark-field illumination. For plasmonic nanoparticles, scattering properties are strongly wavelength dependent and are predominantly enhanced at the plasmon resonance frequency. DFSS is a very useful technique for single particle characterization with the aid of plasmonic particles, and it can be performed using a standard optical microscope in dark-field mode. Dark-field illumination implies that the incident light is directed to illuminate the sample and that the detector should not capture any directly irradiated light, except the one scattered by the sample.[210]

Dark-field illumination can be achieved in several experimental configurations, which in turn can be classified as transmission and reflection modes in general terms. In the first case, the specimen has to be transparent to allow transmission of light, and this configuration usually requires positioning of a dark-field condenser with high numerical aperture (NA) below the sample. In this thesis, reflected dark-field illumination or *epi-illumination* was used, where it is sufficient to have a reflected light dark-field objective (that serves both as condenser and objective) and the sample can be opaque. In both illumination cases, the central portion of the cone of irradiated light is blocked; so that the sample is illuminated with a hollow cone of light as illustrated in Fig. 6.6. In transmission dark-field mode (Fig. 6.6a), the high NA dark field condenser focuses collimated illumination light at an angle steeper than can be collected by the objective, which thus gathers only light scattered by the sample. [210,211]

In the case of dark-field epi-illumination (Fig. 6.6b), the collector transforms the light coming from the microscope lamp into a roughly parallel beam. Most of the light is blocked by the condenser-aperture-diaphragm, which has a central stop, so that only peripheral rays of the beam pass through. The light is then reflected by a 45° mirror with a circular hole in the centre, so that the light travels to the specimen vertically down on the outside of the actual objective lens. Then the light is focused on the sample by an inner mirror at the end of the objective housing. Light is scattered by the nanoparticles on the illuminated sample surface, and part of it is passed back via the objective lens to the eyepiece. The resulting image constitutes a collection of bright spots of different colours and intensities (depending on the particle shape, size and material) against dark background (hence the name "dark-field"), see, for example, Fig. 6.2e. Notice that in the corresponding SEM image in Fig. 6.2f, there is an arrangement of two Ag spheres with a Pd cube in between and, slightly lower, there is a single Ag sphere. These two nanostructures appear as two bright dots in the optical microscope image (Fig. 6.2e, yellow square). However, if we look back at the SEM image (Fig. 6.2f) then it is possible to see also three single Pd cubes, which are not visible in the optical microscope due to the fact that Pd doesn't scatter light very efficiently. This is a nice illustration of why a strongly scattering plasmonic nanoantenna unit such as Au or Ag is needed when using DFSS for studying small nanoparticles (< 40 nm), in particular the ones consisting of materials that have poor scattering properties due to high intrinsic absorption.

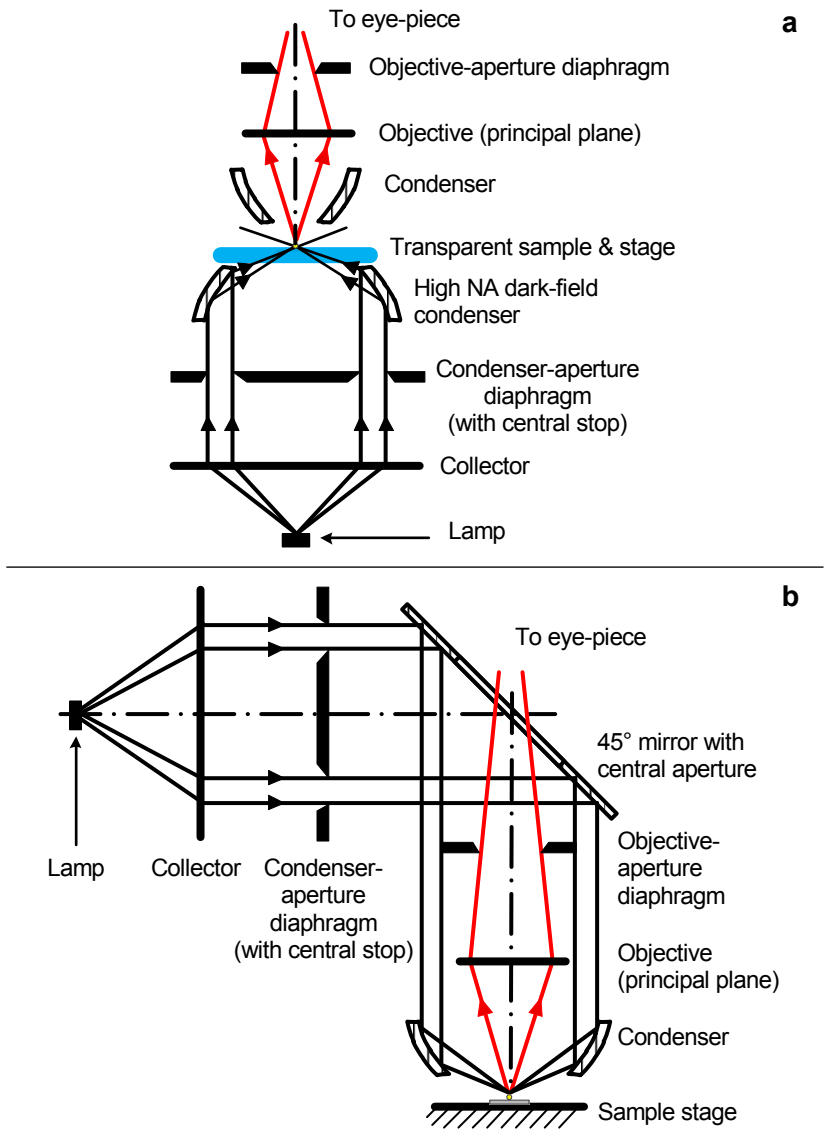


***Figure 6.6.*** *Schematic drawing of the ray-path in (a) transmitted dark-field illumination with high NA condenser; and (b) reflected-light dark-field illumination with an ellipsoidal ring-mirror reflector (beam-splitter) and a concave ring-mirror condenser. Note that all lenses are only shown as a line indicating their principal plane. Incident light and scattered light are shown as black and red arrows respectively. The scattered light from the sample is collected by the objective and directed to the eyepiece. Figure adapted from Nusz*[211] *and Piller*[210].

### 6.4.1 The role of the substrate in DFSS

As already mentioned in Section 6.1, the use of a conductive Si wafer substrate was crucial in order to be able to characterize the individual nanoparticles in SEM and subsequently correlate the measured signals from these single particles with their appearance (i.e. size and shape). The presence of the thin (50 nm) thermally grown $SiO_2$ layer on the Si wafer was necessary, in order to perform DFSS. The reason for this is that nanoparticles on the bare Si substrate are hardly visible with reflected-light dark-field illumination, due to the fact that substantial amount of light is scattered from the nanoparticles into the substrate[212]. Placing a transparent dielectric layer such as $SiO_2$ on top of the reflective Si substrate gives rise to interference effects[213] between the incoming wave and the wave reflected by the Si substrate. This stems from the different refractive indices of the two materials, which are strongly wavelength dependent. The incoming wave of light undergoes multiple reflections and refractions at the interfaces. The dielectric thickness modulates the phase of light and the interference at the interfaces modulates the intensity of the propagating light. Bilayer substrates of this kind are used e.g. for SERS[214] and for detection of atomic layers of graphene in the optical microscope[215]. The interference effect strongly depends on the thickness of the dielectric layer as well as the incidence angle of the incoming light. The presence of the plasmonic nanoparticle on the surface further complicates the physics behind this phenomenon and will not be discussed here. For my work it was sufficient to use 50 nm $SiO_2$ to be able to clearly see the plasmonic particles in the optical microscope and measure the scattering spectra from the individual nanoparticle arrangements. However, it will be very interesting in the future to study different effects that arise with changing substrate arrangements, i.e. different reflecting material, different material and thickness of the dielectric, multiple reflecting and transparent layers and the size of the plasmonic particle.

In **Paper IV**, DFSS measurements were combined with TEM and TKD, which both require electron transparent substrates. Conventional TEM grids or membranes are, however, problematic for the use in DFSS setup because the relatively small grid spacing or etched cavities in the membranes cause stray light scattering or block some of the incoming/scattered light at the low angles that are typically required. To overcome these limitations, I developed a method, which was based on TEM 'windows' that consist of a 40 nm electron-transparent amorphous $Si_3N_4$ membrane[216], combined with the reversible physical vapour deposition of a 10 nm Cr layer on the backside of the membrane (Fig. 6.7). As Finite-Difference Time-Domain (FDTD) simulations of the light scattering by a single Pd nanodisk reveal, the Cr layer acts as a mirror that creates interference effects (see Figure 2 a,b and Supporting Information in **Paper IV**). These effects enhance the intensity of light back-scattered from the Pd nanoparticles (which generally are poor scatterers[217]), and thus make them visible on a CCD-chip. After the experiment, the Cr mirror layer is removed by wet etching from the backside (assuring that the etch does not interact with the nanoparticles) to transform the sample to its electron microscopy compatible state. This facilitates TKD and TEM analysis on the same single nanoparticles as the ones probed *in operando* by

plasmonic nanospectroscopy. The cycle can be repeated multiple times by subsequently growing and removing the Cr layer.

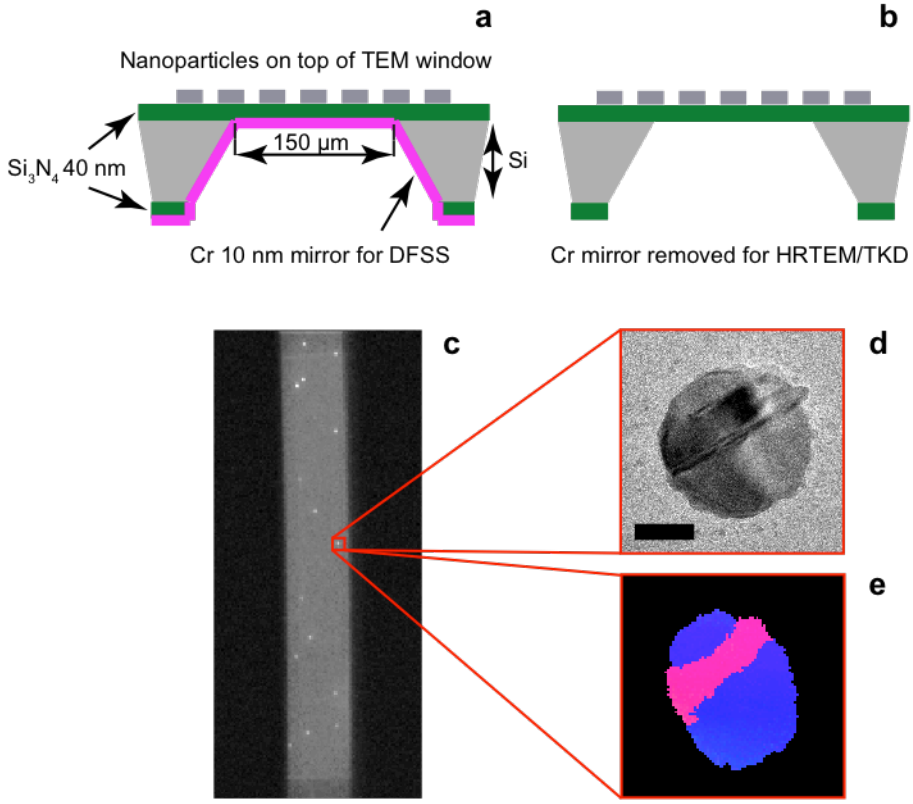


***Figure 6.7.*** *Schematic drawing of a TEM "window" with a 10 nm Cr layer at the back (a) that allows DFSS measurements as indicated by the microscope/spectrometer CCD-image in (c). Removing the Cr layer by wet etching returns the TEM window (b) to its electron-transparent state to facilitate characterization of individual nanoparticles measured in DFSS by HRTEM (d) and TKD (e). The scale bar is 50 nm in (d).*

## 6.5 Single particle spectroscopy setup

In order to study single nanoparticles using nanoplasmonic sensing, a single particle spectroscopy setup had to be assembled for this project. The setup had to have several parts, which would serve certain purpose. First of all, there had to be a measurement cell to host the sample with nanostructures and to allow temperature control over the sample, as well as to establish a sealed environment with controlled flow and

composition of different gases around the sample. Furthermore, the cell had to fit the stage of the optical microscope, which would be used to address the individual nanoparticles using dark-field microscopy. Finally, there had to be a spectrometer to be able to measure the scattering signal from the nanostructures in a spectrally resolved fashion. The following is the description of the setup I assembled, fulfilling all of these conditions.

The measurement cell was purchased from Linkam and it is a temperature-controlled stage THMS600 with working range from -196 to 600 °C. The setup is depicted schematically in Fig. 6.8, where one can see the Linkam chamber mounted on the microscope stage (Nikon Eclipse LV100 upright optical microscope). The Linkam stage is connected to a set of mass flow controllers (Bronkhorst) that have several different working ranges to supply the desired flow of reactants to the sample that is put inside the stage in a small quartz cup (see Fig. 6.9). Above the sample cup, the cell has a quartz window, through which it is possible to focus on the nanostructures using the microscope objective, in this case usually a Nikon 50× BD. The sample is directly illuminated with the microscope's 50 W halogen lamp (Nikon LV-HL50W LL). The scattered light from individual plasmonic nanostructures can be collected in two ways: 1) by an optical fibre (**Papers I, II, III**) or 2) an open optics system (**Paper IV**). In (1), an optical fiber (Ocean Optics, UV-vis 200 or 600 μm core) is connected to the microscope eye-piece tube via a custom made fibre adapter. In the open optics configuration, the scattered light is collected via a lens tube containing one broadband dielectric mirror and two visible achromats. The collected light is directed to the entrance slit (500 or 1000 μm) of a spectrometer (Andor Shamrock SR303i) and dispersed using a grating (150 lines/mm, blaze wavelength 800 nm). The scattering spectra are recorded using a thermoelectrically cooled charge-coupled device (CCD) camera (Andor Newton). The microscope with measurement cell and spectrometer stands on a floating optical table (Newport), which provides a flat and stable surface and helps to eliminate vibrations from the environment.

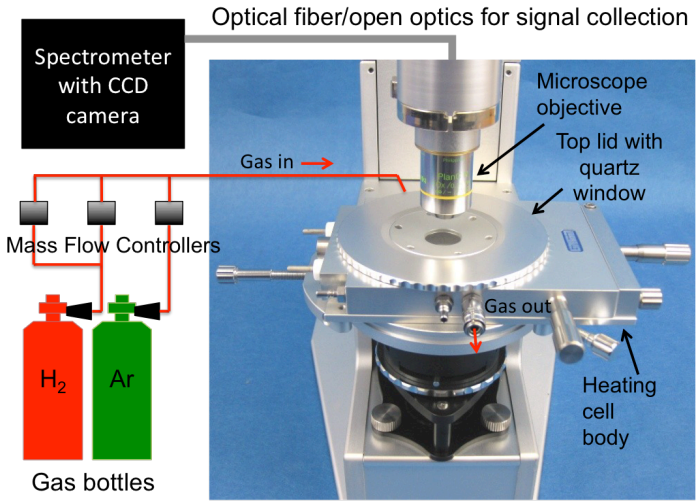


***Figure 6.8.*** *The schematics of the whole setup: gases are supplied through a range of MFCs to the Linkam chamber located on the optical microscope stage. The chamber has a quartz window, through which one can focus on the sample inside the chamber via a microscope objective. The scattering signal from the nanoparticles dispersed on the sample in focus is collected with an optical fibre or an open optics system (not shown). The signal is directed to the spectrometer equipped with a CCD camera.*

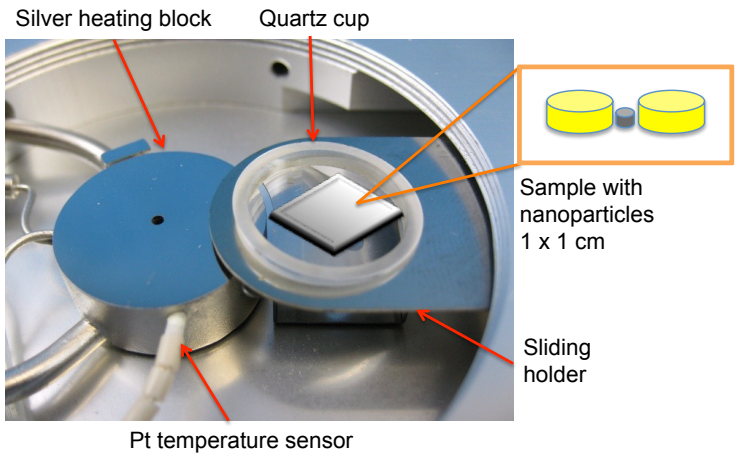


***Figure 6.9.*** *View of the Linkam chamber with the top lid removed: one can see the Ag heating block and the partly retracted quartz cup containing the sample. The cup with the sample piece is placed exactly above the heating block with the help of a sliding holder. The Pt resistor T-sensor mounted inside the Ag block, accurate to 0.1°C, provides a stable temperature signal and feedback to the temperature controller.*

### 6.5.1 Signal acquisition

At 50× objective magnification that was used in the measurements, the estimated sampling area with a 600 μm core fibre is about 12.5 $\mu m^2$, which allows for selective collection of the scattered light from individual nanoparticles fabricated/dispersed at low density on the sample surface (Fig. 6.10).

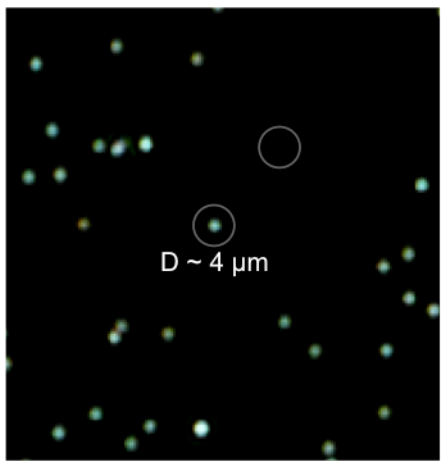


***Figure 6.10.*** *Dark-field microscope image of the sample, where each bright spot corresponds to a single Ag nanosphere. The white circle around one of the particles in the centre of the image indicates an area with diameter ~ 4 μm from which light is collected by the fiber. Another circle without nanoparticle indicates a possible area for dark background measurement. Note that each spot can be measured with the fiber only one at a time.*

With an open optics system, the microscope field of view is imaged on the entrance slit of the spectrometer (Fig. 6.11), which can be operated in the image mode or spectroscopy mode depending if a mirror (or a grating in zero order position) or a grating is positioned in the light path. In the mirror position, the particles are visible as points of light, and the particle of interest can be centered in the slit. When switched to the grating position, the light from the particle will be spread out by wavelength. In this configuration (as opposed to using a fiber), it is possible to measure several particles (up to 10 - 12 individual particles as long as they are well separated from each other and are not on the same horizontal line) at the time using the "Multi-track" mode of the Andor Solis control software, by defining multiple tracks on the CCD. This is also useful to measure a background spectrum together with the particle spectrum.

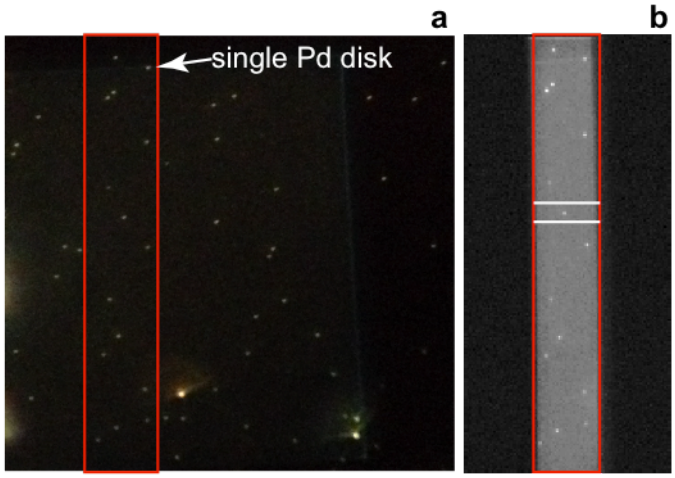


***Figure 6.11.*** *(a) Sample overview from the microscope with the region of interest indicated by a red rectangle. Each bright spot corresponds to a single nanoparticle. (b) View from CCD camera connected to spectrometer in the imaging mode with the slit narrowed (1000 μm) such that only particles from the region of interest are visible. The two white lines indicate the height of the track (10 pixels) chosen for one of the particles. Several tracks can be chosen along the vertical line of the slit. When the grating is inserted in the light path, the spectra can be collected from each of the selected tracks simultaneously, allowing spectral imaging of several particles at the same time, as well as background collection.*

Normalized scattering spectra with intensity $I_{sc}$ are obtained from individual plasmonic particles as a function of wavelength $\lambda$ using the relation $I_{sc}(\lambda) = (S(\lambda) - D(\lambda))/CRS(\lambda)$, where $S(\lambda)$ is the collected signal from an area with nanoparticle, $D(\lambda)$ is the signal from the nearby area without nanoparticle (dark signal for background correction), and $CRS(\lambda)$ is the signal collected from a diffuse white certified reflectance standard (Labsphere SRS-99-020). $CRS(\lambda)$ was used in order to correct the signal for the lamp emission spectrum, which is strongly wavelength-dependent. The acquisition time for each spectrum was varied depending on the measurement needs from 0.125 s to 10 s.

## 6.6 Mass spectrometry

Mass spectrometry (MS) is an analytical technique, which measures the masses and amounts of sample components.[218] The sample (in gas, liquid or solid form) is ionized to produce gas-phase ions (e.g. by electron, ion or photon bombardment, thermally or by electric fields). All the ions are separated in the mass spectrometer according to their mass-to-charge ratio ($m/z$), and then detected according to their abundance. A mass spectrum of molecular species is thus produced, which represents the relative abundance of detected ions as function of the mass-to-charge ratio. Most mass

spectrometers operate under high vacuum conditions and consist of three main parts: 1) ionizer to form charged particles; 2) ion-analyzer (mass filter) to sort ions by their mass-to-charge ratio and 3) detector to measure the value of an indicator quantity and to provide data for calculating the abundance of each ion. Mass spectrometers may differ by the type of ion-analyzer (also called mass filter), and there are four types commonly used: 1) sector field devices that utilize magnetic field for deflection of moving charge carriers; 2) time-of-flight mass spectrometers utilize differing velocities of molecules of equal energy; 3) ion traps, where ion trajectories are influenced by a high-frequency field and 4) quadrupole mass spectrometers utilize the resonance of moving ions in a high-frequency field. Ions that went through mass analyzer then hit the ion detector, which is usually an electron multiplier or microchannel plates that emit a cascade of electrons when each ion hits the detector plate. From the obtained mass spectrum one can derive the elemental or isotopic composition of the sample, presence and number of certain elements, as well as masses and chemical structure of the molecules. A literature search and specialized computer programs can help with interpretation of the results.[218]

In **Paper V**, MS measurements were carried out by Dr. Su Liu.

# 7 SUMMARY AND OUTLOOK

The results of this thesis are presented in six appended papers, for which a brief summary is given in this chapter, followed by a short outlook.

## 7.1 Summary of appended papers

The work presented in **Paper I** was motivated by the fact that, in order to utilize the strong electric field enhancement in the hot spot of plasmonic nanoantennas for sensing in a materials science context, it is crucial to be able to place a nanoobject of interest with high accuracy in such a hot spot. This is problematic with state-of-the-art nanofabrication approaches, especially when several materials are to be used, small gaps are required and large surface areas are to be patterned. In the paper, we present a novel fabrication method called Shrinking-Hole Colloidal Lithography (SHCL), which is a further development of the established Hole-mask Colloidal Lithography (HCL) technique. In SHCL we introduce three different variations of a critical step that exploits a "shrinking hole" effect to enhance the versatility of HCL. The effect of the "shrinking hole" arises from the fact that, as material is deposited through the hole-mask created in the HCL process, it also continuously builds up at the rims of the hole, thus causing it to shrink continuously. We show that this effect can be utilized systematically in combination with the growth of sacrificial nanostructures. Depending on the specifics of the targeted application and desired material combinations of the final structure, the sacrificial nanostructure that is grown in order to shrink the hole in the mask to the required size (so that it can be used to grow a smaller nanoparticle) can constitute (i) a C nanocone, (ii) a Cr nanocone or (iii) a Cr funnel. If exploited carefully, as demonstrated in the paper, this approach provides unique possibilities for the self-aligned crafting of complex multimaterial nanostructures with high level of control over the size and position of the constituent elements. As in HCL, the method also preserves the ability of patterning large areas (few $cm^2$) with aligned complex nanostructures. To illustrate the possibilities, we demonstrate the fabrication of several complex plasmonic nanoantennas, such as: Au nanodisc dimer with small Pd particle in the hot-spot, cascaded Au trimer, Au-Pd disc heterodimer and Au disc with small Pd and $Al_2O_3$ particles on each side. In the second part of the paper we show on two specific examples what kind of sensing functionality that can be achieved with the fabricated structures. In the first example, we demonstrate an all-optical self-referenced hydrogen sensor based on light polarization that is comprised of an array of a Au nanodiscs with a smaller adjacent Pd particle. In

the second example, we demonstrate the single particle hydrogen sensing capability of a Au nanodisc dimer with small Pd particle in the dimer gap.

The main focus of **Paper II** is the development of a synthesis strategy for the self-assembly of two different individual colloidal nanoparticles into *hetero*dimers. Utilizing electrostatic interactions, we show the possibilities to combine oppositely charged individual nanoparticles of different sizes, shapes and materials into heterodimer combinations. Using this approach, the following heterodimers were obtained: Au or Ag spheres of 90 nm paired with Au cubes (30 nm) or Au rhombic dodecahedra (50 nm), as well as combinations of Pd nanoparticles of different sizes and shapes (cubes of 25 or 70 nm, rhombic dodecahedra of 110 nm, truncated cubes of 120 nm, octahedra of 130 nm) with Au or Ag spheres of 90 nm. We show that the aggregation process can be controlled to produce the highest possible yield of dimers by tuning the ratio between the two different nanoparticle components. The synthesis results are rationalized with the aid of theoretical modelling. Such coupled nanoparticle systems possess new properties and are interesting for numerous applications. As a basic example, we demonstrate the possibility of sensing a catalytic process such as hydrogen dissociation and absorption in a single Pd nanocube by using the Au plasmonic unit as the probe for the reaction that is taking place on the adjacent Pd particle.

In **Paper III**, we make use of the Au-Pd heterodimers synthesized with the method described in **Paper II**, and further utilize the sensing capabilities of the plasmonic Au unit in order to investigate processes happening in/on adjacent Pd nanoparticle at the single particle level. Specifically, we study size and shape effects on the thermodynamic properties of hydrogen absorption in Pd. The incentive of our work is a deeper understanding of the role of particle specific features in the metal-hydrogen interactions at the nanoscale, since this can help optimizing the performance of hydride-forming materials, as well as to unearth the physics of phase transitions in shape-selected nanocrystals. Moreover, the detailed studies of hydrogen interaction with nanoscale Pd systems (focusing mainly on ensembles of Pd nanoparticles) have began only recently and yield contradicting results, as well as provoke interesting questions regarding the details of the process. Single particle studies enable elimination of the issues caused by the inhomogeneous sample effects that potentially blur important details of the role of nanoparticle size, shape and local chemical composition on both hydrogen sorption thermodynamics and kinetics. We investigate the hydrogen absorption in Pd nanocubes with size ranging from 65 to 17 nm and measure phase transition isotherms. We quantify the thermodynamics of the process by analysing changes in enthalpy and entropy of hydrogen absorption for individual cubes. In addition, we investigate other Pd particle shapes, such as octahedron and rod. As a result, we find consistent size- and shape-independent thermodynamics and significantly wider hysteresis than in bulk, with details depending on the specifics of individual nanoparticles. Generally, the absorption branch of the hysteresis loop is size-dependent in the sub-30nm regime, whereas desorption is size- and shape-independent. The former is consistent with a coherent phase transition during hydride formation, influenced kinetically by the specifics of nucleation, whereas the latter

implies that hydride decomposition either occurs incoherently or via different kinetic pathways.

The plasmonic nanospectroscopy approach for probing individual nanoparticles is further developed and applied also in **Paper IV** to study the role of grain boundaries and grain size in hydride phase transformations of individual polycrystalline Pd nanoparticles. This is motivated by the fact that grain boundaries can be important mediators of phase transformations by contributing to diffusion and plastic deformation processes, and by accumulating impurities. There are numerous experimental and theoretical studies of grain boundaries and their role in the bulk, but they are scarcely explored for nanomaterials. In such systems, grain boundaries are expected to be of significant importance due to the relative abundance of grain boundary sites compared to bulk materials with larger grains. In the paper, we use a multichannel plasmonic nanospectroscopy approach that enables measurements of the individual response from 10 and more nanoparticles simultaneously, during both hydrogen absorption and desorption. This is a significant advance compared to the state of the art, where new experiment is necessary for each studied nanoparticle, which means that artifacts due to experiment-to-experiment variations cannot be avoided. The spectroscopic measurements are then correlated with TEM and transmission Kikuchi diffraction (TKD) characterization, which reveal details of Pd nanoparticle-grain-boundary structure, type and orientation. We find correlation between length and type of grain boundaries in individual nanoparticles, and their hydride formation pressure. Using an analytical model, we identify tensile lattice strain, induced by hydrogen atoms near grain boundaries, as the main factor controlling the phase transition during hydrogen absorption. This indicates that polycrystalline nanoparticles can be understood as agglomerate of single crystallites that exhibit similar characteristics to "free" nanocrystals, whose interaction is mediated by the grain boundaries.

In **Paper V**, mass spectrometry is combined with *in operando* plasmonic nanospectroscopy of single catalyst nanoparticles in a customized new instrument. The presented experimental setup is a step forward in catalyst characterization techniques as it for the first time enables the analysis of reaction products in combination with the information about the state of single catalyst nanoparticles as obtained by plasmonic nanospectroscopy. This makes it possible to, for example, directly correlate catalyst nanoparticle state and its activity or selectivity. First, the approach is demonstrated by studying the kinetic phase transition phenomenon during the oxidation of hydrogen over silica supported Pt nanocatalysts at the ensemble level, to demonstrate the complementarity between the information obtained by plasmonic nanospectroscopy and mass spectrometry. The single-nanoparticle-experiment capabilities are demonstrated on the example of hydride formation detection in a single Pd nanoparticle, as well as carbon monoxide oxidation over single Pt and Pd catalyst nanoparticles.

In **Paper VI**, we present a method for the nanofabrication of core-shell nanostructures, where the particle core is made of a metal and the shell constitutes a dielectric layer,

which further can be decorated by small nanoparticles of a material of choice. The motivation for this work is that nanostructures of variable composition can combine multiple properties, which cannot be achieved by single-material nanoparticles. This concept can be of high importance in variety of applications such as catalysis, optics or electronics. Specifically here, the target application of the fabrication method was the preparation of a tailored model system suitable for studying plasmon-assisted light absorption in small catalyst nanoparticles grown on the dielectric shell encapsulating the plasmonic nanoantenna. The purpose of the plasmonic core is to enhance photocatalytic effects mediated by hot electrons created by light absorption. The dielectric layer is crucial for protection of the nanoantenna in harsh experimental conditions characteristic for catalysis, such as high temperatures and aggressive gas environments. In addition, the dielectric layer enables both tailoring of the surface chemistry for a specific catalyst formulation and maximizing the near-field coupling in the hybrid-plasmonic photocatalyst material. The key results of this work are: (1) the first demonstration of large-scale nanofabrication of arrays of core-shell nanostructures with widely tailored material compositions in terms of all constituents (beyond what currently is possible by colloidal synthesis, which is the standard way of making core-shell structures); (2) the manifestation of significant absorption enhancement in small catalyst nanoparticles grown on the core-shell structures, and (3) photocatalytic reaction rate enhancement as well as quenching on such structures, depending on the specific system and reactant mixing regime.

## 7.2 Outlook

There are many possibilities to continue the work presented in this thesis, since it to a large extent dealt with the development of the necessary tools for single particle plasmonic nanospectroscopy for materials science and catalysis applications. With these tools now at hand, the fun part only begins. For example, as continuation of **Paper I**, it would be interesting to test sensing capabilities of other arrangements such as cascaded nanodisc trimers, asymmetric dimers and symmetric trimers as shown in Fig. 4.4 f – h. According to theoretical studies[219,220] the field enhancement in these structures should be even higher than the one in a homogeneous dimer arrangement, with the consequence of higher sensitivities. This implies the prospects to be able to investigate even smaller catalytic particles, ideally in the sub 10 nm size range, where strong size-effects are predicted.

Another interesting route is to test various dielectric spacer layers, as shown in Fig. 4.4e, for the protection of the plasmonic antenna structure, which is relevant for the use of the antenna at elevated temperatures and in harsh gas environments. Heat treatment causes the Au nanoparticles to recrystallize and change their shape at temperatures starting already at 100°C. At even higher temperatures Au atoms become highly mobile and there is a tendency to reduce the total surface area of the particle, which is energetically more favourable[221]. In case of, for example, Ag nanoparticles, which actually support stronger LSPR (and thus have narrower peaks, which is advantageous for sensing) than Au, adding a spacer layer may help to protect them

from oxidation to which Ag is prone even in air. Moreover, no matter the plasmonic material, there is always a risk that high temperatures may cause fusion of the sensor elements with a particle deposited in the gap, which also could be avoided by capping the antenna elements with a dielectric layer. This idea was already implemented in **Paper VI**, but for the most basic structure one can make with HCL, i.e. nanodisc. With more complicated structures, it becomes technically more difficult. It is also important to note that the use of dielectric spacer layers can make it possible to investigate the role of the catalyst support material in a catalytic reaction, which in many cases is critical for the catalyst activity and selectivity.

With respect to the results of **Paper II** and **III**, it is obvious that the plasmonic particle used, i.e. the Au sphere, is not the most advantageous shape for sensing purposes as it features much lower field enhancement compared to nanoparticles with more distinct shapes. Therefore, it will be interesting to try new arrangements, for example, a Au rod, a Au triangle, or any other shape that has pointy edges or sides that feature strong field enhancements, with an interesting particle attached to it. Similarly, as mentioned above for nanofabricated nanoparticles, adding a spacer layer around the plasmonic unit of the synthesized nanoparticles is of high interest. There are possibilities to grow spacer layers around metal nanoparticles with wet chemistry methods, for example, shells of $SiO_2$[222].

As was mentioned earlier, the nanolithography approaches for nanofabrication are efficient for making ordered arrays of complex nanostructures on surfaces. However, they lack the ability to precisely control the shape, size and crystallinity of the particle of interest since they are limited by the resolution provided by the used mask. Therefore, it would be interesting to combine the fabrication approaches of **Paper I** and **Papers II**, **III**, i.e. nanolithography with wet chemical synthesis. For example, the fabricated dimer or trimer arrangements could have a particle with specific chemistry deposited in their junctions, and then the synthesised particle with well-defined size and shape could be bound to the hot spot. The latter could be possible using a tailored linker molecule (present on the surface of the synthesized particle), which specifically binds to the specific surface chemistry provided in the hot spot only by locally growing, e.g. small patches of $TiO_2$, $Al_2O_3$, which contrast the surface chemistry of the rest of the support. In such a way, it could be possible to bind not only synthesized particles but also, for example, quantum dots (QD) specifically to the hot spot. The latter are interesting due to their tunable fluorescent properties, as well as the possibility to boost these properties by placing a QD in the region of the high field enhancement, and to investigate phenomena such as strong coupling of two oscillators.

**Paper IV** is an outcome of successful combination of plasmonic nanospectroscopy with correlated TKD characterization. The alliance of these two techniques can give insight into the role of particle-specific structure and defects in hydrogen-metal interaction of other hydride forming metal nanosystems (e.g. metal alloys (PdAu[223]), Mg[60,224] and yttrium[225] (Y)), as well as other processes like oxidation/reduction of metallic nanostructures[226].

Similarly, **Paper V** is only a very first study combining mass spectrometry with *in operando* plasmonic nanospectroscopy of single catalyst nanoparticles, which opens up new possibilities for more detailed investigations of other catalytic processes using any of the nanoparticle arrangements provided as a result of Papers I, II and VI. These studies should be aimed at revealing size/shape/microstructure effects of the particle in question with respect to the investigated catalytic process. That could be, for example, formation of water on the surface of Pt or Pd by reacting hydrogen and oxygen, the oxidation of carbon monoxide or the conversion of nitrogen oxides ($NO_x$) on Pt.

Another part of **Paper VI** dealt with plasmonic photocatalysis, which is also an area of research, where structure-function relationships based on the size/shape of the (photo)catalyst particle are only starting to emerge[227]. This is important since LSPR wavelength and plasmon decay mechanisms of plasmonic nanoparticles are strongly dependent on the particle geometry. Therefore, characteristics of the plasmon driven photocatalysts such as wavelength dependence, reaction selectivity and reaction efficiency are expected to be tunable with structure of the plasmonic nanoparticles.

In general, as demonstrated in this thesis, single particle studies enabled by plasmonic nanospectroscopy can give valuable information about particle functionality, which is governed not only by the size/shape of individual nanoparticles but also by the particle-specific microstructure. The developed plasmonic nanospectroscopy approach can be applied in combination with other techniques such as TEM, TKD, XPS, and mass spectrometry, to provide unprecedented insight into the structure-correlated activity of individual nanoparticles during various physical/chemical processes that are highly relevant for the fields of materials science and catalysis.

# 8 ACKNOWLEDGEMENTS

I would like to acknowledge the Chalmers Area of Advance Nanoscience and Nanotechnology for financing my work, the ERC Starting Grant "SINCAT", the Swedish Research Council project 2014-4956, and the Knut and Alice Wallenberg Foundation projects 2015.0057, 2016.0210 as well as their support of the μ-fab cleanroom infrastructure in Sweden.

I would also like to thank all the people who made this thesis happen:

First of all, my supervisor:

Christoph, thank you very much for giving me the opportunity to work with you! It was a real privilege and a lot of fun! I learned a lot. Thank you that you were always there to support, motivate and inspire me when I needed it most!

Henrik, my examiner, Igor, my former supervisor and Anders, my assistant supervisor – thank you very much for your help throughout this work, and for the very valuable comments during writing of this thesis.

Carl, thank you very much for our collaborations, discussions and travels together!

Kasper, Yuri, Tina and Giammarco, for our collaborations on Pd nanocrystals.

Vladimir and Tomasz, thank you very much for our theoretical collaborations!

Arturo, thank you very much for working very hard on preparing our manuscript in time!

Su, Ferry, Sara, Stephan and Iwan for our lab collaborations.

The Nanofabrication laboratory staff at the Department of MC2 at Chalmers, for maintaining excellent cleanroom facility and all the help. Special thanks to Henrik Frederiksen for all the advice and help in the cleanroom.

Joachim, my officemate, for productive discussions and chocolate.

All past and present members of the Chemical Physics group, which is a very nice group to be a part of!

My family and friends!

# 9 BIBLIOGRAPHY


1 Glover, R. D., Miller, J. M. & Hutchison, J. E. Generation of Metal Nanoparticles from Silver and Copper Objects: Nanoparticle Dynamics on Surfaces and Potential Sources of Nanoparticles in the Environment. *ACS Nano* **5**, 8950-8957 (2011).

2 Lungu, M., Neculae, A., Bunoiu, M. & Biris, C. *Nanoparticles' Promises and Risks: Characterization, Manipulation, and Potential Hazards to Humanity and the Environment*. (Springer International Publishing, 2014).

3 Barber, D. J. & Freestone, I. C. An Investigation of the Origin of the Colour of the Lycurgus cup by Analytical Transmission Electron Microscopy. *Archaeometry* **32**, 33-45 (1990).

4 Walter, P., Welcomme, E., Hallégot, P., Zaluzec, N. J., Deeb, C., Castaing, J., Veyssière, P., Bréniaux, R., Lévêque, J-L. & Tsoucaris, G. Early Use of PbS Nanotechnology for an Ancient Hair Dyeing Formula. *Nano Letters* **6**, 2215-2219 (2006).

5 Haveli, S. D. Walter, P., Patriarche, G., Ayache, J., Castaing, J., Van Elslande, E., Tsoucaris, G., Wang, P-A. & Kagan, H. B. Hair Fiber as a Nanoreactor in Controlled Synthesis of Fluorescent Gold Nanoparticles. *Nano Letters* **12**, 6212-6217 (2012).

6 Deng, D., Gopiraman, M., Kim, S. H., Chung, I.-M. & Kim, I. S. Human Hair: A Suitable Platform for Catalytic Nanoparticles. *ACS Sustainable Chemistry & Engineering* **4**, 5409-5414 (2016).

7 Sciau, P. *Nanoparticles in Ancient Materials: The Metallic Lustre Decorations of Medieval Ceramics*. (INTECH Open Access Publisher, 2012).

8 Vance, M. E., Kuiken, T., Vejerano, E. P., McGinnis, S. P., Hochella, M. F., Rejeski, D. & Hull, M. S. Nanotechnology in the Real World: Redeveloping the Nanomaterial Consumer Products Inventory. *Beilstein Journal of Nanotechnology* **6**, 1769-1780 (2015).

9 Haley, B. & Frenkel, E. Nanoparticles for Drug Delivery in Cancer Treatment. *Urologic Oncology: Seminars and Original Investigations* **26**, 57-64 (2008).

10 Huang, H. S. & Hainfeld, J. F. Intravenous Magnetic Nanoparticle Cancer Hyperthermia. *International Journal of Nanomedicine* **8**, 2521-2532 (2013).

11 Agasti, S. S., Rana, S., Park, M-H., Kim, C. K., You, C-C. & Rotello, V. M. Nanoparticles for Detection and Diagnosis. *Advanced Drug Delivery Reviews* **62**, 316-328 (2010).

12 Baglioni, P., Carretti, E. & Chelazzi, D. Nanomaterials in Art Conservation. *Nature Nanotechnology* **10**, 287-290 (2015).

13 Munafò, P., Quagliarini, E., Goffredo, G. B., Bondioli, F. & Licciulli, A. Durability of Nano-engineered $TiO_2$ Self-cleaning Treatments on Limestone. *Construction and Building Materials* **65**, 218-231 (2014).

14 Duncan, T. V. Applications of Nanotechnology in Food Packaging and Food Safety: Barrier Materials, Antimicrobials and Sensors. *Journal of Colloid and Interface Science* **363**, 1-24 (2011).

15 Visions for a Molecular Future. *Nature Nanotechnology* **8**, 385-389 (2013).

16 Pradeep, T. & Anshup. Noble Metal Nanoparticles for Water Purification: A Critical Review. *Thin Solid Films* **517**, 6441-6478 (2009).

17 Gehrke, I., Geiser, A. & Somborn-Schulz, A. Innovations in Nanotechnology for Water Treatment. *Nanotechnology, Science and Applications* **8**, 1-17 (2015).

18 Yunus, I. S., Harwin, Kurniawan, A., Adityawarman, D. & Indarto, A. Nanotechnologies in Water and Air Pollution Treatment. *Environmental Technology Reviews* **1**, 136-148 (2012).

19 Karn, B., Kuiken, T. & Otto, M. Nanotechnology and *in situ* Remediation: A Review of the Benefits and Potential Risks. *Ciencia Saude Coletiva* **16**, 165-178 (2011).

20 Zang, L. *Energy Efficiency and Renewable Energy Through Nanotechnology*. (Springer, 2011).

21 Lacher, J. R. A Theoretical Formula for the Solubility of Hydrogen in Palladium. *Proceedings of the Royal Society of London. Series A, Mathematical and Physical Sciences* **161**, 0525-0545 (1937).

22 Völkl, J. & Alefeld, G. in *Hydrogen in Metals I: Basic Properties* (eds Georg Alefeld & Johann Völkl) 321-348 (Springer Berlin Heidelberg, 1978).

23 Steyrer, G. & Peisl, J. Coherent Phase Transition in $NbH_x$ Studied by Neutron Radiography. *EPL (Europhysics Letters)* **2**, 835 (1986).

24 Miceli, P. F., Zabel, H. & Cunningham, J. E. Hydrogen-induced Strain Modulation in Nb-Ta Superlattices. *Physical Review Letters* **54**, 917-919 (1985).

25 Kirchheim, R. & Pundt, A. in *Physical Metallurgy (Fifth Edition)* (ed Kazuhiro Hono) 2597-2705 (Elsevier, 2014).

26 Berube, V., Radtke, G., Dresselhaus, M. & Chen, G. Size Effects on the Hydrogen Storage Properties of Nanostructured Metal Hydrides: A review. *Int. J. Energy Res.* **31**, 637-663 (2007).

27 Bogdanović, B., Ritter, A. & Spliethoff, B. Active $MgH_2$-Mg Systems for Reversible Chemical Energy Storage. *Angewandte Chemie International Edition in English* **29**, 223-234 (1990).

28 Paskevicius, M., Sheppard, D. A., Williamson, K. & Buckley, C. E. Metal Hydride Thermal Heat Storage Prototype for Concentrating Solar Thermal Power. *Energy* **88**, 469-477 (2015).

29 Hübert, T., Boon-Brett, L., Black, G. & Banach, U. Hydrogen Sensors – A Review. *Sensors and Actuators B: Chemical* **157**, 329-352 (2011).

30 Flis, J. *Corrosion of Metals and Hydrogen-related Phenomena: Selected Topics*. (Elsevier, 1991).

31 Louthan, M. R. Hydrogen Embrittlement of Metals: A Primer for the Failure Analyst. *Journal of Failure Analysis and Prevention* **8**, 289-307 (2008).

32 Baturina, O. A. & Smirnova, A. E. in *New and Future Developments in Catalysis* 69-97 (Elsevier, 2013).

33 Bell, A. T. The Impact of Nanoscience on Heterogeneous Catalysis. *Science* **299**, 1688-1691 (2003).

34 Rodriguez, J. A., Hanson, J. C. & Chupas, P. J. *In-situ Characterization of Heterogeneous Catalysts*. (Wiley, 2013).

35 Zlotea, C., Oumellal, Y., Provost, K. & Ghimbeu, C. M. Experimental Challenges in Studying Hydrogen Absorption in Ultrasmall Metal Nanoparticles. *Frontiers in Energy Research* **4** (2016).

36 Fritzsche, H., Huot, J. & Fruchart, D. *Neutron Scattering and Other Nuclear Techniques for Hydrogen in Materials*. (Springer International Publishing, 2016).

37 Pasturel, M., Slaman, M., Schreuders, H., Rector, J. H., Borsa, D. M., Dam, B. & Griessen, R. Hydrogen Absorption Kinetics and Optical Properties of Pd-doped Mg Thin Films. *Journal of Applied Physics* **100**, 023515 (2006).

38 Gremaud, R., Broedersz, C. P., Borsa, D. M., Borgschulte, A., Mauron, P., Schreuders, H., Rector, J. H., Dam, B. & Griessen, R. Hydrogenography: An Optical Combinatorial Method To Find New Light-Weight Hydrogen-Storage Materials. *Advanced Materials* **19**, 2813-2817, (2007).

39 Bardhan, R., Hedges, L. O., Pint, C. L., Javey, A., Whitelam, S. & Urban, J. J. Uncovering the Intrinsic Size Dependence of Hydriding Phase Transformations in Nanocrystals. *Nature Materials* **12**, 905-912 (2013).

40 Wadell, C., Syrenova, S. & Langhammer, C. Plasmonic Hydrogen Sensing with Nanostructured Metal Hydrides. *ACS Nano* **8**, 11925-11940 (2014).

41 Meier, J., Friedrich, K. A. & Stimming, U. Novel Method for the Investigation of Single Nanoparticle Reactivity. *Faraday Discussions* **121**, 365-372 (2002).

42 Tel-Vered, R. & Bard, A. J. Generation and Detection of Single Metal Nanoparticles Using Scanning Electrochemical Microscopy Techniques†. *The Journal of Physical Chemistry B* **110**, 25279-25287 (2006).

43 Xiao, X. & Bard, A. J. Observing Single Nanoparticle Collisions at an Ultramicroelectrode by Electrocatalytic Amplification. *Journal of the American Chemical Society* **129**, 9610-9612 (2007).

44 Roeffaers, M. B. J., Sels, B. F., Uji-i, H., De Schryver, F. C., Jacobs, P. A., De Vos, D. E. & Hofkens, J. Spatially Resolved Observation of Crystal-face-dependent Catalysis by Single Turnover Counting. *Nature* **439**, 572-575 (2006).

45 van Schrojenstein Lantman, E. M., Deckert-Gaudig, T., Mank, A. J. G., Deckert, V. & Weckhuysen, B. M. Catalytic Processes Monitored at the Nanoscale with Tip-enhanced Raman Spectroscopy. *Nature Nanotechnology* **7**, 583-586 (2012).

46 de Smit, E., Swart, I., Creemer, J. F., Hoveling, G. H., Gilles, M. K., Tyliszczak, T., Kooyman, P. J., Zandbergen, H. W., Morin, C., Weckhuysen, B. M. & de Groot, F. M. F. Nanoscale Chemical Imaging of a Working Catalyst by Scanning Transmission X-ray Microscopy. *Nature* **456**, 222-225 (2008).

47 Langhammer, C. & Larsson, E. M. Nanoplasmonic *In Situ* Spectroscopy for Catalysis Applications. *ACS Catalysis* **2**, 2036-2045 (2012).

48 Langhammer, C., Zorić, I., Kasemo, B. & Clemens, B. M. Hydrogen Storage in Pd Nanodisks Characterized with a Novel Nanoplasmonic Sensing Scheme. *Nano Letters* **7**, 3122-3127 (2007).

49 Langhammer, C., Larsson, E. M., Kasemo, B. & Zorić, I. Indirect Nanoplasmonic Sensing: Ultrasensitive Experimental Platform for Nanomaterials Science and Optical Nanocalorimetry. *Nano Letters* **10**, 3529-3538 (2010).

50 Li, K., Qin, W., Xu, Y., Peng, T. & Li, D. Optical Approaches in Study of Nanocatalysis with Single-molecule and Single-particle Resolution. *Frontiers of Optoelectronics*, **8**, 379-393 (2014).

51 Sambur, J. B. & Chen, P. Approaches to Single-Nanoparticle Catalysis. *Annual Review of Physical Chemistry* **65**, 395-422 (2014).

52 Hansen, P. L., Wagner, J. B., Helveg, S., Rostrup-Nielsen, J. R., Clausen, B. S. & Topsøe, H. Atom-Resolved Imaging of Dynamic Shape Changes in Supported Copper Nanocrystals. *Science* **295**, 2053-2055 (2002).

53 Boyes, E. D., Ward, M. R., Lari, L. & Gai, P. L. ESTEM Imaging of Single Atoms under Controlled Temperature and Gas Environment Conditions in Catalyst Reaction Studies. *Annalen der Physik* **525**, 423-429 (2013).

54 Vendelbo, S. B., Elkjær, C. F., Falsig, H., Puspitasari, I., Dona, P., Mele, L., Morana, B., Nelissen, B. J., van Rijn, R., Creemer, J. F., Kooyman, P. J. & Helveg, S. Visualization of Oscillatory Behaviour of Pt Nanoparticles Catalysing CO Oxidation. *Nature Materials* **13**, 884-890 (2014).

55 Creemer, J. F., Helveg, S., Hoveling, G. H., Ullmann, S., Molenbroek, A. M., Sarro, P. M. & Zandbergen, H. W. Atomic-scale Electron Microscopy at Ambient Pressure. *Ultramicroscopy* **108**, 993-998 (2008).

56 Jinschek, J. R. Achieve Atomic Resolution in *in situ* S/TEM Experiments to Examine Complex Interface Structures in Nanomaterials. *Current Opinion in Solid State and Materials Science* **21**, 77-91 (2017).

57 Thomas, J. M. Reflections on the Value of Electron Microscopy in the Study of Heterogeneous Catalysts. *Proceedings of the Royal Society A: Mathematical, Physical and Engineering Science* **473** (2017).

58 Kooyman, P. J. in *Operando Research in Heterogeneous Catalysis* (eds Joost Frenken & Irene Groot) 111-129 (Springer International Publishing, 2017).

59 Liu, N., Tang, M. L., Hentschel, M., Giessen, H. & Alivisatos, A. P. Nanoantenna-enhanced Gas Sensing in a Single Tailored Nanofocus. *Nature Materials* **10**, 631-636 (2011).

60 Shegai, T. & Langhammer, C. Hydride Formation in Single Palladium and Magnesium Nanoparticles Studied By Nanoplasmonic Dark-Field Scattering Spectroscopy. *Advanced Materials* **23**, 4409-4413 (2011).

61 Baldi, A., Narayan, T. C., Koh, A. L. & Dionne, J. A. *In situ* Detection of Hydrogen-induced Phase Transitions in Individual Palladium Nanocrystals. *Nature Materials* **13**, 1143-1148 (2014).

62 Narayan, T. C., Baldi, A., Koh, A. L., Sinclair, R. & Dionne, J. A. Reconstructing Solute-induced Phase Transformations within Individual Nanocrystals. *Nature Materials* **15**, 768-774 (2016).

63 Narayan, T. C., Hayee, F., Baldi, A., Leen Koh, A., Sinclair, R. & Dionne, J. A. Direct Visualization of Hydrogen Absorption Dynamics in Individual Palladium Nanoparticles. *Nature Communications* **8**, 14020 (2017).

64 Ulvestad, A., Welland, M. J., Collins, S. S. E., Harder, R., Maxey, E., Wingert, J., Singer, A., Hy, S., Mulvaney, P., Zapol, P. & Shpyrko, O. G. Avalanching Strain Dynamics During the Hydriding Phase Transformation in Individual Palladium Nanoparticles. *Nature Communications* **6**, 10092 (2015).

65 Ulvestad, A., Welland, M. J., Cha, W., Liu, Y., Kim, J. W., Harder, R., Maxey, E., Clark, J. N., Highland, M. J., You, H., Zapol, P., Hruszkewycz, S. O. &

Stephenson, G. B. Three-dimensional Imaging of Dislocation Dynamics During the Hydriding Phase Transformation. *Nature Materials* **16**, 565-571, (2017).

66 Ghosh Chaudhuri, R. & Paria, S. Core/Shell Nanoparticles: Classes, Properties, Synthesis Mechanisms, Characterization, and Applications. *Chemical Reviews* **112** (2012).

67 Gawande, M. B., Goswami, A., Asefa, T., Guo, H., Biradar, A.V., Peng, D-L., Zboril, R. & Varma, R. S. Core-shell Nanoparticles: Synthesis and Applications in Catalysis and Electrocatalysis. *Chemical Society Reviews* **44**, 7540-7590 (2015).

68 Liu, R. & Priestley, R. D. Rational Design and Fabrication of Core-shell Nanoparticles through a One-step/pot Strategy. *Journal of Materials Chemistry A* **4**, 6680-6692 (2016).

69 Li, G., Kobayashi, H., Taylor, J. M., Ikeda, R., Kubota, Y., Kato, K., Takata, M., Yamamoto, T., Toh, S., Matsumura, S. & Kitagawa, H. Hydrogen Storage in Pd Nanocrystals Covered with a Metal–organic Framework. *Nature Materials* **13**, 802-806 (2014).

70 Mie, G. Beiträge zur Optik trüber Medien, speziell kolloidaler Metallösungen. *Annalen der Physik* **330**, 377-445 (1908).

71 Bohren, C. F. & Huffman, D. R. *Absorption and scattering of light by small particles*. (Wiley, 1983).

72 Mirkin, C. A. & Niemeyer, C. M. *Nanobiotechnology II: More Concepts and Applications*. (John Wiley & Sons, 2007).

73 Mishchenko, M. I., Hovenier, J. W. & Travis, L. D. *Light Scattering by Nonspherical Particles: Theory, Measurements, and Applications*. (Academic Press, 2000).

74 Jain, P. K., Lee, K. S., El-Sayed, I. H. & El-Sayed, M. A. Calculated Absorption and Scattering Properties of Gold Nanoparticles of Different Size, Shape, and Composition: Applications in Biological Imaging and Biomedicine. *The Journal of Physical Chemistry B* **110**, 7238-7248 (2006).

75 Hao, E. & Schatz, G. C. Electromagnetic Fields around Silver Nanoparticles and Dimers. *The Journal of Chemical Physiscs* **120**, 357-366 (2004).

76 Hao, F., Nehl, C. L., Hafner, J. H. & Nordlander, P. Plasmon Resonances of a Gold Nanostar. *Nano Letters* **7**, 729-732 (2007).

77 Wang, H., Brandl, D. W., Le, F., Nordlander, P. & Halas, N. J. Nanorice: A Hybrid Plasmonic Nanostructure. *Nano Letters* **6**, 827-832 (2006).

78 Wu, Y. & Nordlander, P. Plasmon Hybridization in Nanoshells with a Nonconcentric Core. *The Journal of Chemical Physics* **125**, - (2006).

79 Knight, M. W. & Halas, N. J. Nanoshells to Nanoeggs to Nanocups: Optical Properties of Reduced Symmetry Core–shell Nanoparticles beyond the Quasistatic Limit. *New Journal of Physics* **10**, 105006 (2008).

80 Wokaun, A., Gordon, J. P. & Liao, P. F. Radiation Damping in Surface-Enhanced Raman Scattering. *Physical Review Letters* **48**, 957-960 (1982).

81 Shalaev, V. M. & Kawata, S. *Nanophotonics with Surface Plasmons*. (Elsevier, 2007).

82 Langhammer, C., Yuan, Z., Zorić, I. & Kasemo, B. Plasmonic Properties of Supported Pt and Pd Nanostructures. *Nano Letters* **6**, 833-838 (2006).

83 Kanehara, M., Koike, H., Yoshinaga, T. & Teranishi, T. Indium Tin Oxide Nanoparticles with Compositionally Tunable Surface Plasmon Resonance Frequencies in the Near-IR Region. *Journal of the American Chemical Society* **131**, 17736-17737 (2009).

84 Zhao, Y., Pan, H., Lou, Y., Qiu, X., Zhu, J. & Burda, C. Plasmonic $Cu_{2-x}S$ Nanocrystals: Optical and Structural Properties of Copper-Deficient Copper(I) Sulfides. *Journal of the American Chemical Society* **131**, 4253-4261 (2009).

85 Dorfs, D., Härtling, T., Miszta, K., Bigall, N. C., Kim, M. R., Genovese, A., Falqui, A., Povia, M. & Manna, L. Reversible Tunability of the Near-Infrared Valence Band Plasmon Resonance in $Cu_{2-x}Se$ Nanocrystals. *Journal of the American Chemical Society* **133**, 11175-11180 (2011).

86 Grigorenko, A. N., Polini, M. & Novoselov, K. S. Graphene Plasmonics. *Nature Photonics* **6**, 749-758 (2012).

87 Tassin, P., Koschny, T., Kafesaki, M. & Soukoulis, C. M. A Comparison of Graphene, Superconductors and Metals as Conductors for Metamaterials and Plasmonics. *Nature Photonics* **6**, 259-264 (2012).

88 Ma, X., Dai, Y., Yu, L. & Huang, B. Noble-metal-free Plasmonic Photocatalyst: Hydrogen Doped Semiconductors. *Scientific Reports* **4** (2014).

89 Geim, A. K. & Novoselov, K. S. The Rise of Graphene. *Nature Materials* **6**, 183-191 (2007).

90 Bonaccorso, F., Sun, Z., Hasan, T. & Ferrari, A. C. Graphene Photonics and Optoelectronics. *Nature Photonics* **4**, 611-622 (2010).

91 Michaels, A. M., Jiang & Brus, L. Ag Nanocrystal Junctions as the Site for Surface-Enhanced Raman Scattering of Single Rhodamine 6G Molecules. *The Journal of Physical Chemistry B* **104**, 11965-11971 (2000).

92 Rechberger, W., Hohenau, A., Leitner, A., Krenn, J. R., Lamprecht, B. & Aussenegg, F. R. Optical Properties of Two Interacting Gold Nanoparticles. *Optics Communications* **220**, 137-141 (2003).

93 Gunnarsson, L., Rindzevicius, T., Prikulis, J., Kasemo, B., Käll, M., Zou, S. & Schatz, G. C. Confined Plasmons in Nanofabricated Single Silver Particle Pairs: Experimental Observations of Strong Interparticle Interactions. *The Journal of Physical Chemistry B* **109**, 1079-1087 (2004).

94 Song, J.-H., Hong, S.-Y., Kim, Y.-G., Lee, K.-W. & Kim, Y.-Y. Observation of Plasmon Hybridization in Gold Nanoparticle Pairs. *Journal of the Korean Physical Society* **50**, 558-562 (2007).

95 Jain, P. K. & El-Sayed, M. A. Surface Plasmon Coupling and its Universal Size Scaling in Metal Nanostructures of Complex Geometry: Elongated Particle Pairs and Nanosphere Trimers. *Journal of Physical Chemistry C* **112**, 4954-4960 (2008).

96 Jain, P. K. & El-Sayed, M. A. Noble Metal Nanoparticle Pairs: Effect of Medium for Enhanced Nanosensing. *Nano Letters* **8**, 4347-4352 (2008).

97 Acimovic, S. S., Kreuzer, M. P., Gonzalez, M. U. & Quidant, R. Plasmon Near-Field Coupling in Metal Dimers as a Step toward Single-Molecule Sensing. *ACS Nano* **3**, 1231-1237 (2009).

98 Dadosh, T., Sperling, J., Bryant, G. W., Breslow, R., Shegai, T., Dyshel, M., Haran, G. & Bar-Joseph, I. Plasmonic Control of the Shape of the Raman Spectrum of a Single Molecule in a Silver Nanoparticle Dimer. *ACS Nano* **3**, 1988-1994 (2009).

99 Cheng, Y., Wang, M., Borghs, G. & Chen, H. Gold Nanoparticle Dimers for Plasmon Sensing. *Langmuir* **27**, 7884-7891 (2011).

100 Halas, N. J., Lal, S., Chang, W.-S., Link, S. & Nordlander, P. Plasmons in Strongly Coupled Metallic Nanostructures. *Chemical Reviews* **111**, 3913-3961 (2011).

101 Tittl, A., Kremers, C., Dorfmueller, J., Chigrin, D. N. & Giessen, H. Spectral Shifts in Optical Nanoantenna-enhanced Hydrogen Sensors. *Optical Materials Express* **2**, 111-118 (2012).

102 Jain, P. K. & El-Sayed, M. A. Universal Scaling of Plasmon Coupling in Metal Nanostructures: Extension from Particle Pairs to Nanoshells. *Nano Letters* **7**, 2854-2858 (2007).

103 Jain, P. K., Huang, W. & El-Sayed, M. A. On the Universal Scaling Behavior of the Distance Decay of Plasmon Coupling in Metal Nanoparticle Pairs: A Plasmon Ruler Equation. *Nano Letters* **7**, 2080-2088 (2007).

104 Lassiter, J. B., Aizpurua, J., Hernandez, L. I., Brandl, D. W., Romero, I., Lal, S., Hafner, J. H., Nordlander, P. & Halas, N. J. Close Encounters between Two Nanoshells. *Nano Letters* **8**, 1212-1218 (2008).

105 Boyer, D., Tamarat, P., Maali, A., Lounis, B. & Orrit, M. Photothermal Imaging of Nanometer-Sized Metal Particles Among Scatterers. *Science* **297**, 1160-1163 (2002).

106 Billaud, P., Marhaba, S., Grillet, N., Cottancin, E., Bonnet, C., Lermé, J., Vialle, J-L., Broyer, M. & Pellarin, M. Absolute Optical Extinction Measurements of Single Nano-objects by Spatial Modulation Spectroscopy using a White Lamp. *Review of Scientific Instruments* **81**, 043101 (2010).

107 Kumar, C. S. S. R. *Raman Spectroscopy for Nanomaterials Characterization*. (Springer, 2012).

108 Shen, Y. R. Surface Properties Probed by Second-harmonic and Sum-frequency Generation. *Nature* **337**, 519-525 (1989).

109 Ohtsu, M. *Progress in Nanophotonics 1*. (Springer, 2011).

110 Douillard, L., Charra, F., Fiorini, C., Adam, P. M., Bachelot, R., Kostcheev, S., Lerondel, G., Lamy de la Chapelle, M. & Royer, P. Optical Properties of Metal Nanoparticles as Probed by Photoemission Electron Microscopy. *Journal of Applied Physics* **101**, 083518 (2007).

111 Grubisic, A. Ringe, E., Cobley, C. M., Xia, Y., Marks, L. D., Van Duyne, R. P. & Nesbitt, D. J. Plasmonic Near-Electric Field Enhancement Effects in Ultrafast Photoelectron Emission: Correlated Spatial and Laser Polarization Microscopy Studies of Individual Ag Nanocubes. *Nano Letters* **12**, 4823-4829 (2012).

112 Chaturvedi, P., Hsu, K. H., Kumar, A., Fung, K. H., Mabon, J. C. & Fang, N. X. Imaging of Plasmonic Modes of Silver Nanoparticles Using High-Resolution Cathodoluminescence Spectroscopy. *ACS Nano* **3**, 2965-2974 (2009).

113 García de Abajo, F. J. & Kociak, M. Probing the Photonic Local Density of States with Electron Energy Loss Spectroscopy. *Physical Review Letters* **100**, 106804 (2008).

114 Ringe, E., Sharma, B., Henry, A.-I., Marks, L. D. & Van Duyne, R. P. Single Nanoparticle Plasmonics. *Physical Chemistry Chemical Physics* **15**, 4110-4129 (2013).

115 Clavero, C. Plasmon-induced Hot-electron Generation at Nanoparticle/metal-oxide Interfaces for Photovoltaic and Photocatalytic Devices. *Nature Photonics* **8**, 95-103 (2014).

116 Smith, J. G., Faucheaux, J. A. & Jain, P. K. Plasmon Resonances for Solar Energy Harvesting: A Mechanistic Outlook. *Nano Today* **10**, 67-80 (2015).

117 Narang, P., Sundararaman, R. & Atwater, H. A. Plasmonic Hot Carrier Dynamics in Solid-state and Chemical Systems for Energy Conversion. *Nanophotonics* **5**, 96-111 (2016).

118 Brongersma, M. L., Halas, N. J. & Nordlander, P. Plasmon-induced Hot Carrier Science and Technology. *Nature Nanotechnology* **10**, 25-34 (2015).

119 Chen, X., Zheng, Z., Ke, X., Jaatinen, E., Xie, T., Wang, D., Guo, C., Zhao, J. & Zhu, H. Supported Silver Nanoparticles as Photocatalysts under Ultraviolet and Visible Light Irradiation. *Green Chemistry* **12**, 414-419 (2010).

120 Christopher, P., Xin, H. & Linic, S. Visible-light-enhanced Catalytic Oxidation Reactions on Plasmonic Silver Nanostructures. *Nature Chemistry* **3**, 467-472 (2011).

121 Mukherjee, S., Libisch, F., Large, N., Neumann, O., Brown, L. V., Cheng, J., Lassiter, J. B., Carter, E. A., Nordlander, P. & Halas, N. J. Hot Electrons Do the Impossible: Plasmon-Induced Dissociation of $H_2$ on Au. *Nano Letters* **13**, 240-247 (2013).

122 Marimuthu, A., Zhang, J. & Linic, S. Tuning Selectivity in Propylene Epoxidation by Plasmon Mediated Photo-Switching of Cu Oxidation State. *Science* **339**, 1590-1593 (2013).

123 Zhou, L., Zhang, C., McClain, M. J., Manjavacas, A., Krauter, C. M., Tian, S., Berg, F., Everitt, H. O., Carter, E. A., Nordlander, P. & Halas, N. J. Aluminum Nanocrystals as a Plasmonic Photocatalyst for Hydrogen Dissociation. *Nano Letters* **16**, 1478-1484 (2016).

124 Zorić, I., Zäch, M., Kasemo, B. & Langhammer, C. Gold, Platinum, and Aluminum Nanodisk Plasmons: Material Independence, Subradiance, and Damping Mechanisms. *ACS Nano* **5**, 2535-2546 (2011).

125 Wadell, C., Antosiewicz, T. J. & Langhammer, C. Optical Absorption Engineering in Stacked Plasmonic Au–$SiO_2$–Pd Nanoantennas. *Nano Letters* **12**, 4784-4790 (2012).

126 Antosiewicz, T. J., Apell, S. P., Wadell, C. & Langhammer, C. Absorption Enhancement in Lossy Transition Metal Elements of Plasmonic Nanosandwiches. *The Journal of Physical Chemistry C* **116**, 20522-20529 (2012).

127 Antosiewicz, T. J. & Apell, S. P. Optical Enhancement of Plasmonic Activity of Catalytic Metal Nanoparticles. *RSC Advances* **5**, 6378-6384 (2015).

128 Antosiewicz, T. J., Wadell, C. & Langhammer, C. Plasmon-Assisted Indirect Light Absorption Engineering in Small Transition Metal Catalyst Nanoparticles. *Advanced Optical Materials* **3**, 1591-1599 (2015).

129 Swearer, D. F., Zhao, H., Zhou, L., Zhang, C., Robatjazi, H., Martirez, J. M. P., Krauter, C. M., Yazdi, S., McClain, M. J., Ringe, E., Carter, E. A., Nordlander, P. & Halas, N. J. Heterometallic Antenna−reactor Complexes for Photocatalysis. *Proceedings of the National Academy of Sciences* **113**, 8916-8920 (2016).

130 Linic, S., Christopher, P. & Ingram, D. B. Plasmonic-metal Nanostructures for Efficient Conversion of Solar to Chemical Energy. *Nature Materials* **10**, 911-921 (2011).

131 Manjavacas, A., Liu, J. G., Kulkarni, V. & Nordlander, P. Plasmon-Induced Hot Carriers in Metallic Nanoparticles. *ACS Nano* **8**, 7630-7638 (2014).

132 Zheng, B. Y., Zhao, H., Manjavacas, A., McClain, M., Nordlander, P. & Halas, N. J. Distinguishing between Plasmon-induced and Photoexcited Carriers in a Device Geometry. *Nature Communications* **6**, 7797 (2015).

133 Hammer, B. & Nørskov, J. K. in *Advances in Catalysis* Vol. 45 71-129 (2000).

134 Behl, M. & Jain, P. K. Catalytic Activation of a Solid Oxide in Electronic Contact With Gold Nanoparticles. *Angewandte Chemie International Edition* **54**, 992-997 (2015).

135 Conner, W. C. & Falconer, J. L. Spillover in Heterogeneous Catalysis. *Chemical Reviews* **95**, 759-788 (1995).

136 Keblinski, P., Cahill, D. G., Bodapati, A., Sullivan, C. R. & Taton, T. A. Limits of Localized Heating by Electromagnetically Excited Nanoparticles. *Journal of Applied Physics* **100**, 054305 (2006).

137 Zhdanov, V. P., Zorić, I. & Kasemo, B. Plasmonics: Heat transfer between metal nanoparticles and supporting nanolayers. *Physica E: Low-dimensional Systems and Nanostructures* **46**, 113-118 (2012).

138 Graham, T. On the Absorption and Dialytic Separation of Gases by Colloid Septa. *Philosophical Transactions of the Royal Society of London* **156**, 399-439 (1866).

139 Felderhoff, M. & Bogdanovic, B. High Temperature Metal Hydrides as Heat Storage Materials for Solar and Related Applications. *International Journal of Molecular Sciences* **10**, 325-344 (2009).

140 Oumellal, Y., Rougier, A., Nazri, G. A., Tarascon, J. M. & Aymard, L. Metal Hydrides for Lithium-ion Batteries. *Nature Materials* **7**, 916-921 (2008).

141 Yoshimura, K., Langhammer, C. & Dam, B. Metal Hydrides for Smart Window and Sensor Applications. *MRS Bulletin* **38**, 495-503 (2013).

142 Huiberts, J. N., Griessen, R., Rector, J. H., Wijngaarden, R. J., Dekker, J. P., de Groot, D. G. & Koeman, N. J. Yttrium and Lanthanum Hydride Films with Switchable Optical Properties. *Nature* **380**, 231-234 (1996).

143 Fukai, Y. *The Metal-Hydrogen System: Basic Bulk Properties*. (Springer Berlin Heidelberg, 2006).

144 Wicke, E., Brodowsky, H. & Züchner, H. in *Hydrogen in Metals II: Application-Oriented Properties* (eds Georg Alefeld & Johann Völkl) 73-155 (Springer Berlin Heidelberg, 1978).

145 Schlapbach, L. in *Hydrogen in Intermetallic Compunds II: Surface and Dynamic Properties, Applications* (ed Louis Schlapbach) 15-95 (Springer Berlin Heidelberg, 1992).

146 Christmann, K. Interaction of Hydrogen with Solid Surfaces. *Surface Science Reports* **9**, 1-163 (1988).

147 Flanagan, T. B., Balasubramaniarn, R. & Kirchheim, R. Exploring Lattice Defects in Palladium and its Alloys Using Dissolved Hydrogen. Part I: Hydrogen Solubility and its Segregation to Dislocations and Vacancies. *Platinum Metals Review* **45**, 114-121 (2001).

148 Flanagan, T. B., Balasubramaniam, R. & Kirchheim, R. Exploring Lattice Defects in Palladium and its Alloys Using Dissolved Hydrogen: Part II: Hydrogen Segregation to Internal Interfaces and to Inhomogeneous Regions. *Platinum Metals Review* **45**, 166-174 (2001).

149 Behm, R. J., Penka, V., Cattania, M. G., Christmann, K. & Ertl, G. Evidence for Subsurface Hydrogen on Pd(110) - an Intermediate between Chemisorbed and Dissolved Species. *Journal of Chemical Physics* **78**, 7486-7490 (1983).

150 Peisl, H. in *Hydrogen in Metals I: Basic Properties* (eds Georg Alefeld & Johann Völkl) 53-74 (Springer Berlin Heidelberg, 1978).

151 Baranowski, B., Majchrzak, S. & Flanagan, T. B. The Volume Increase of fcc Metals and Alloys due to Interstitial Hydrogen over a Wide Range of Hydrogen Contents. *Journal of Physics F: Metal Physics* **1**, 258 (1971).

152 Wagner, C. The Interpretation of the Hysteresis Phenomena in the Palladium-hydrogen System such as with Rotation Conversions. *Zeitschrift Fur Physikalische Chemie-Leipzig* **193**, 386-406 (1944).

153 Krug, R. R., Hunter, W. G. & Grieger, R. A. Statistical Interpretation of Enthalpy-entropy Compensation. *Nature* **261**, 566-567 (1976).

154 Griessen, R., Strohfeldt, N. & Giessen, H. Thermodynamics of the Hybrid Interaction of Hydrogen with Palladium Nanoparticles. *Nature Materials* **15**, 311-317 (2016).

155 Ubbelohde, A. R. Some Properties of the Metallic State I - Metallic Hydrogen and its Alloys. *Proceedings of the Royal Society of London A: Mathematical, Physical and Engineering Sciences* **159**, 0295-0306 (1937).

156 Abraham, B. M. & Flotow, H. E. The Heats of Formation of Uranium Hydride, Uranium Deuteride and Uranium Tritide at 25-degrees. *Journal of the American Chemical Society* **77**, 1446-1448 (1955).

157 Everett, D. H. & Nordon, P. Hysteresis in the Palladium-hydrogen System. *Proceedings of the Royal Society of London A: Mathematical, Physical and Engineering Sciences* **259**, 341-360 (1960).

158 Scholtus, N. A. & Hall, W. K. Hysteresis in Palladium-hydrogen System. *The Journal of Chemical Physics* **39**, 868-870 (1963).

159 Lundin, C. E. & Lynch, F. E. in *Hydrides for Energy Storage* (ed A. J. Maeland) 395-405 (Pergamon, 1978).

160 Flanagan, T. B., Bowerman, B. S. & Biehl, G. E. Hysteresis in Metal-hydrogen Systems. *Scripta Metallurgica* **14**, 443-447 (1980).

161 Flanagan, T. B. & Clewley, J. D. Hysteresis in Metal-hydrides. *Journal of the Less-Common Metals* **83**, 127-141 (1982).

162 Birnbaum, H. K., Grossbeck, M. L. & Amano, M. Hydride Precipitation in Nb and Some Properties of NbH. *Journal of the Less-Common Metals* **49**, 357-370 (1976).

163 Schwarz, R. B. & Khachaturyan, A. G. Thermodynamics of Open Two-phase Systems with Coherent Interfaces: Application to Metal–hydrogen Systems. *Acta Materialia* **54**, 313-323 (2006).

164 Hughes, R. C., Schubert, W. K., Zipperian, T. E., Rodriguez, J. L. & Plut, T. A. Thin-film Palladium and Silver Alloys and Layers for Metal-insulator-semiconductor Sensors. *Journal of Applied Physics* **62**, 1074-1083 (1987).

165 Hughes, R. C. & Schubert, W. K. Thin-films of Pd/Ni Alloys for Detection of High Hydrogen Concentrations. *Journal of Applied Physics* **71**, 542-544 (1992).

166 Westerwaal, R. J., Rooijmans, J. S. A., Leclercq, L., Gheorghe, D. G., Radeva, T., Mooij, L., Mak, T., Polak, L., Slaman, M., Dam, B. & Rasing, T.Nanostructured Pd-Au Based Fiber Optic Sensors for Probing Hydrogen Concentrations in Gas Mixtures. *International Journal of Hydrogen Energy* **38**, 4201-4212 (2013).

167 Wagner, H. in *Hydrogen in Metals I: Basic Properties* (eds Georg Alefeld & Johann Völkl) 5-51 (Springer Berlin Heidelberg, 1978).

168 Myers, S. M., Baskes, M. I., Birnbaum, H. K., Corbett, J. W., Deleo, G. G., Estreicher, S. K., Haller, E. E., Jena, P., Johnson, N. M., Kirchheim, R., Pearton, S. J. & Stavola, M. J. Hydrogen Interactions with Defects in Crystalline Solids. *Reviews of Modern Physics* **64**, 559-617 (1992).

169 Kirchheim, R. Interaction of Hydrogen with Dislocations in Palladium—I. Activity and Diffusivity and their Phenomenological Interpretation. *Acta Metallurgica* **29**, 835-843 (1981).

170 Mütschele, T. & Kirchheim, R. Segregation and Diffusion of Hydrogen in Grain Boundaries of Palladium. *Scripta Metallurgica* **21**, 135-140 (1987).

171 Kuji, T., Flanagan, T. B., Sakamoto, Y. & Hasaka, M. Hydrogen Chemical Potentials and Dislocation Structures Following Quenching of Palladium-hydrogen Alloys into the Two-phase Envelope. *Scripta Metallurgica* **19**, 1369-1373 (1985).

172 Campbell, F. C. *Elements of Metallurgy and Engineering Alloys*. (ASM International, 2008).

173 Lejček, P. in *Grain Boundary Segregation in Metals* 5-24 (Springer Berlin Heidelberg, 2010).

174 Mütschele, T. & Kirchheim, R. Hydrogen as a Probe for the Average Thickness of a Grain Boundary. *Scripta Metallurgica* **21**, 1101-1104 (1987).

175 Eastman, J. A., Thompson, L. J. & Kestel, B. J. Narrowing Of The Palladium-Hydrogen Miscibility Gap In Nanocrystalline Palladium. *Physical Review B* **48**, 84-92 (1993).

176 Weissmuller, J. & Lemier, C. Lattice Constants of Solid Solution Microstructures: The Case of Nanocrystalline Pd-H. *Physical Review Letters* **82**, 213-216 (1999).

177 Niu, W. X., Zhang, L. & Xu, G. B. Shape-Controlled Synthesis of Single-Crystalline Palladium Nanocrystals. *ACS Nano* **4**, 1987-1996 (2010).

178 Suleiman, M., Faupel, J., Borchers, C., Krebs, H. U., Kirchheim, R. & Pundt, A. Hydrogen Absorption Behaviour in Nanometer Sized Palladium Samples Stabilised in Soft and Hard Matrix. *Journal of Alloys and Compounds* **404–406**, 523-528 (2005).

179 Larche, F. C. in *Advances in Phase Transitions* 193-203 (Pergamon, 1988).

180 Wadell, C., Pingel, T., Olsson, E., Zorić, I., Zhdanov, V. P. & Langhammer, C. Thermodynamics of Hydride Formation and Decomposition in Supported Sub-10 nm Pd Nanoparticles of Different Sizes. *Chemical Physics Letters* **603**, 75-81 (2014).

181 Sachs, C., Pundt, A., Kirchheim, R., Winter, M., Reetz, M. T. & Fritsch, D. Solubility of Hydrogen in Single-Sized Palladium Clusters. *Physical Review B* **64** (2001).

182 Narehood, D. G., Kishore, S., Goto, H., Adair, J. H., Nelson, J. A., Gutiérrez, H. R. & Eklund, P. C. X-ray Diffraction and H-storage in Ultra-small Palladium Particles. *International Journal of Hydrogen Energy* **34**, 952-960 (2009).

183 Yamauchi, M., Ikeda, R., Kitagawa, H. & Takata, M. Nanosize Effects on Hydrogen Storage in Palladium. *The Journal of Physical Chemistry C* **112**, 3294-3299 (2008).

184 Pundt, A., Sachs, C., Winter, M., Reetz, M. T., Fritsch, D. & Kirchheim, R. Hydrogen Sorption in Elastically Soft Stabilized Pd-clusters. *Journal of Alloys and Compounds* **293–295**, 480-483 (1999).

185 Pundt, A., Suleiman, M., Bähtz, C., Reetz, M. T., Kirchheim, R. & Jisrawi, N. M. Hydrogen and Pd-clusters. *Materials Science and Engineering: B* **108**, 19-23 (2004).

186 Langhammer, C., Zhdanov, V. P., Zorić, I. & Kasemo, B. Size-dependent Hysteresis in the Formation and Decomposition of Hydride in Metal Nanoparticles. *Chemical Physics Letters* **488**, 62-66 (2010).

187 Züttel, A., Nützenadel, Ch., Schmid, G., Emmenegger, Ch., Sudan, P. & Schlapbach, L. Thermodynamic Aspects of the Interaction of Hydrogen with Pd Clusters. *Applied Surface Science* **162–163**, 571-575 (2000).

188 Langhammer, C., Zhdanov, V. P., Zorić, I. & Kasemo, B. Size-Dependent Kinetics of Hydriding and Dehydriding of Pd Nanoparticles. *Physical Review Letters* **104**, 135502 (2010).

189 Cui, Z. *Nanofabrication: Principles, Capabilities and Limits*. (Springer, 2008).

190 Zhirnov, V. V. & Herr, D. J. C. New Frontiers: Self-Assembly and Nanoelectronics. *Computer* **34**, 34-43 (2001).

191 Heiz, U. & Landman, U. *Nanocatalysis*. (Springer, 2007).

192 Chi, L. *Nanotechnology: Volume 8: Nanostructured Surfaces*. (John Wiley & Sons, 2010).

193 Fredriksson, H., Alaverdyan, Y., Dmitriev, A., Langhammer, C., Sutherland, D. S., Zaech, M. & Kasemo, B. Hole-Mask Colloidal Lithography. *Advanced Materials* **19**, 4297-4302 (2007).

194 Fredriksson, H. *Nanostructures of Graphite and Amorphous Carbon - Fabrication and Properties* Thesis for the degree of doctor of philosophy, Chalmers University of Technology, (2009).

195 Kreibig, U., Bönnemann, H. & Hormes, J. in *Handbook of Surfaces and Interfaces of Materials* (ed Hari Singh Nalwa) 1-85 (Academic Press, 2001).

196 Siani, A. & Carolina, U. o. S. *Synthesis of Supported Nanoparticles for Catalytic Applications*. (University of South Carolina, 2007).

197 Wu, H.-L., Kuo, C.-H. & Huang, M. H. Seed-Mediated Synthesis of Gold Nanocrystals with Systematic Shape Evolution from Cubic to Trisoctahedral and Rhombic Dodecahedral Structures. *Langmuir* **26**, 12307-12313 (2010).

198 Niu, W., Li, Z-Y., Shi, L., Liu, X., Li, H., Han, S., Chen, J. & Xu, G. Seed-Mediated Growth of Nearly Monodisperse Palladium Nanocubes with Controllable Sizes. *Crystal Growth & Design* **8**, 4440-4444 (2008).

199 Franssila, S. *Introduction to Microfabrication*. (J. Wiley, 2004).

200 Dupas, C., Houdy, P. & Lahmani, M. *Nanoscience: Nanotechnologies and Nanophysics*. (Springer, 2007).

201 Rossnagel, S. M., Cuomo, J. J. & Westwood, W. D. *Handbook of Plasma Processing Technology: Fundamentals, Etching, Deposition, and Surface Interactions*. (Noyes Publications, 1990).

202 Mattox, D. M. *Handbook of Physical Vapor Deposition (PVD) Processing*. (Elsevier, 2007).

203 SreeHarsha, K. S. *Principles of physical vapor deposition of thin films*. (Elsevier, 2006).

204 Kääriäinen, T., Cameron, D., Kääriäinen, M. L. & Sherman, A. *Atomic Layer Deposition: Principles, Characteristics, and Nanotechnology Applications*. (Wiley, 2013).

205 Goldstein, J. *Scanning Electron Microscopy and X-Ray Microanalysis*. (Kluwer Academic/Plenum Publishers, 2003).

206 Maitland, T. & Sitzman, S. in *Scanning Microscopy for Nanotechnology: Techniques and Applications* (eds Weilie Zhou & Zhong Lin Wang) 41-75 (Springer New York, 2007).

207 Keller, R. R. & Geiss, R. H. Transmission EBSD from 10 nm Domains in a Scanning Electron Microscope. *Journal of Microscopy* **245**, 245-251 (2012).

208 Fundenberger, J. J., Bouzy, E., Goran, D., Guyon, J., Yuan, H. & Morawiec, A. Orientation Mapping by Transmission-SEM with an on-axis Detector. *Ultramicroscopy* **161**, 17-22 (2016).

209 Williams, D. B. & Carter, C. B. *Transmission Electron Microscopy: A Textbook for Materials Science*. (Springer, 2009).

210 Piller, H. *Microscope Photometry*. (Springer London, Limited, 2011).

211 Nusz, G. & Chilkoti, A. in *Nanoplasmonic Sensors* (ed Alexandre Dmitriev) 105-126 (Springer New York, 2012).

212 Catchpole, K. R. & Polman, A. Design Principles for Particle Plasmon Enhanced Solar Cells. *Applied Physics Letters* **93**, 191113 (2008).

213 Bacsa, W. S., Pavlenko, E. & Tishkova, V. Optical Interference Substrates for Nanoparticles and Two-Dimensional Materials. *Nanomaterials and Nanotechnology* **3** (2013).

214 Shoute, L. C. T. Multilayer Substrate-Mediated Tuning Resonance of Plasmon and SERS EF of Nanostructured Silver. *Chemphyschem* **11**, 2539-2545 (2010).

215 Blake, P., Hill, E. W., Castro Neto, A. H., Novoselov, K. S., Jiang, D., Yang, R., Booth, T. J. & Geim, A. K. Making Graphene Visible. *Applied Physics Letters* **91**, - (2007).

216 Grant, A. W., Hu, Q. H. & Kasemo, B. Transmission Electron Microscopy 'Windows' For Nanofabricated Structures. *Nanotechnology* **15**, 1175 (2004).

217 Langhammer, C., Kasemo, B. & Zoric, I. Absorption and Scattering of Light by Pt, Pd, Ag, and Au Nanodisks: Absolute Cross Sections and Branching Ratios. *Journal of Chemical Physics* **126**, 194702 (2007).

218 Gross, J. H. & Roepstorff, P. *Mass Spectrometry: A Textbook*. (Springer Berlin Heidelberg, 2011).

219 Li, K., Stockman, M. I. & Bergman, D. J. Self-Similar Chain of Metal Nanospheres as an Efficient Nanolens. *Physical Review Letters* **91**, 227402 (2003).

220 Thomas, R. & Swathi, R. S. Organization of Metal Nanoparticles for Surface-Enhanced Spectroscopy: A Difference in Size Matters. *The Journal of Physical Chemistry C* **116**, 21982-21991 (2012).

221 Chen, Y., Milenkovic, S. & Hassel, A. W. Thermal Stability of {110} Facet Terminated Gold Nanobelts. *Applied Surface Science* **258**, 6224-6231 (2012).

222 Liz-Marzán, L. M., Giersig, M. & Mulvaney, P. Synthesis of Nanosized Gold−Silica Core−Shell Particles. *Langmuir* **12**, 4329-4335 (1996).

223 Wadell, C., Nugroho, F. A. A., Lidström, E., Iandolo, B., Wagner, J. B. & Langhammer, C. Hysteresis-Free Nanoplasmonic Pd–Au Alloy Hydrogen Sensors. *Nano Letters* **15**, 3563-3570 (2015).

224 Sterl, F., Strohfeldt, N., Walter, R., Griessen, R., Tittl, A. & Giessen, H. Magnesium as Novel Material for Active Plasmonics in the Visible Wavelength Range. *Nano Letters* **15**, 7949-7955 (2015).

225 Strohfeldt, N., Tittl, A., Schäferling, M., Neubrech, F., Kreibig, U., Griessen, R. & Giessen, H. Yttrium Hydride Nanoantennas for Active Plasmonics. *Nano Letters* **14**, 1140-1147 (2014).

226 Zhdanov, V. P. Oxidation of Metal Nanoparticles with the Grain Growth in the Oxide. *Chemical Physics Letters* **674**, 136-140 (2017).

227 Li, K., Hogan, N. J., Kale, M. J., Halas, N. J., Nordlander, P. & Christopher, P. Balancing Near-Field Enhancement, Absorption, and Scattering for Effective Antenna–Reactor Plasmonic Photocatalysis. *Nano Letters* **17**, 3710-3717 (2017).